Numerical finite element modelling of the high speed resistance welding process.

Burrows, Richard

Numerical Finite Element Modelling of the High Speed Resistance Welding Process

A thesis by

Richard Burrows

Submitted to Swansea University in fulfilment of the requirements for the degree of Engineering Doctorate in Steel Technology

Swansea University

ProQuest LLC.
789 East Eisenhower Parkway
P.O. Box 1346
Ann Arbor, MI 48106 – 1346

SUMMARY

High Speed Resistance Welding (HSRW) is a high volume welding technique for three-piece can body production using tin-plated steel. Corus, the sponsor of this research, sell approximately 2 million tonnes of steel for this process per annum. At present can manufacturers predominantly use weld settings for their equipment that have an historic rather than scientific basis. They frequently return on-spec batches of steel as unweldable. The purpose of this body of work was to provide a better definition of weldability so that Corus can offer superior technical advice to their customers. In particular, the model described here may be used to aid introduction of new grades of tinplate to customers in a successful and timely manner. Due to the nature of the process, complete understanding of weld evolution is hampered by the impossibility of measuring the exact physical phenomena taking place. This thesis describes an attempt to mathematically model HSRW using a Finite Element model that couples a transient electro-thermal model (Joule heating, conduction and melting/solidification) to the elasto-plastic deformation taking place during the process arising from both applied loads and induced thermal stresses. Heat generation is an integral part of the HSRW process as high heating rates are necessary to achieve temperatures whereby solid state bonding of the steel can take place; erratic heat generation causes defect formation, poorer weld quality and thus reduces production efficiency. Validation of the model is attempted by matching the experimentally measured re-melted tin zone (a fairly robust measurement used in industry which indicates the position that the 232°C isotherm reached on the post-weld surface of the can body) to simulations results. Conclusions are formed on defect origination and evolution, as well as a weldability theory linking process parameters to acceptable weld formation.

DECLARATION

This work has not previously been accepted in substance for any degree and is not being concurrently submitted in candidature for any degree.

Signed ..... (candidate)

Date .....

STATEMENT 1

This thesis is the result of my own investigations, except where otherwise stated. Where correction services have been used, the extent and nature of the correction is clearly marked in a footnote(s).

Other sources are acknowledged by footnotes giving explicit references. A bibliography is appended.

Signed ..... (candidate)

Date .....

STATEMENT 2

I hereby give consent for my thesis, if accepted, to be available for photocopying and for inter-library loan, and for the title and summary to be made available to outside organisations.

Signed ..... (candidate)

Date .....

CONTENTS LIST

1.0 INTRODUCTION

High Speed Resistance Welding is a highly automated joining process that is used in the production of three piece can bodies at a rate of up to 750 cans per minute. Three piece cans are the type of metal packaging that as the name suggests comprises of three pieces, a cylindrical body, a bottom and a top, frequently with an easy open end. The body is formed from a single tinplated steel blank that is rolled over upon itself before the seam is welded. The applications are aerosol cans, pet food tins, paint tins and cans for vegetables and soups to name a few examples.

HSRW is part of the family of seam welds, but remains unique due to the fact that no evidence of melting and solidification is observed in the post weld microstructures. The bond is formed in the solid state so this allows higher speeds to be reached. The literature available on HSRW is thin to say the least with very few articles published in the past few years and on modelling of the process there is even less, an obvious niche ripe for development.

The precise method of bond formation is not fully understood and neither is the origin of defects. The decision was taken to numerically model the process to bring to light more information on the conditions prevalent during welding and a previous study involved the development of a model by [Suthar, 2005] and by [Brown, 2004]. One of the conclusions of this work was that a three dimensional stress code would greatly expand the predictability of the model and it is this that has been developed in this body of work.

The construction of a Finite Element model that sequentially couples a transient electro-thermal model (Joule heating, conduction and melting/solidification) to the elasto-plastic deformation taking place during the process arising from both applied loads and induced thermal stresses is described. The model allows the conditions of a weld during formation to be simulated fully in three dimensions so

further insight can be gained on defect formation and tinplate weldability, something not possible by experiments alone. The model is validated against experimental data and the results attained from the validated model are analysed in detail and conclusions formed on defect formation and weldability.

1.1 Application of Study to Industry

The model provides a powerful research tool that simulates High Speed Resistance Welding, a manufacturing process that cannot be successfully modelled on commercial Finite Element software packages. Of direct benefits to Corus will be the ability to elaborate upon current understanding of the process by offering access to data that is impossible or at least inconvenient to gather from traditional experiments, viz three dimensional stress/temperature/current density maps. Detailed logs produced by the model allow in depth study of heat generation patterns; this can be related to any defect formations or other discrepancies for example. Along with the ability to elaborate upon the physical phenomenon taking place the model can be used as a tool to help when working with customer queries, specifically when steel batches are returned as unweldable, when a few simple setting changes are all that is required. Introduction of future steel grades to customers can be implemented faster and with less downtime when a greater variety of tools are at the disposal for Corus, enhancing their relationship with the customer and promoting greater confidence in Corus Packaging Plus. It is value added services such as these that allow companies such as Corus to maintain or even boost margins whilst retaining customer orders or increasing market share.

2.0 LITERATURE SURVEY

The following is a review of literature available on High Speed Resistance Welding. Despite prevalence of HSRW, there is a profound scarcity of literature owed to the fact that experimental results and data are usually very commercially sensitive. The literature presented does however provide the reader with insight into the process and some closely related processes are reviewed where the author sees as appropriate.

2.1 PRINCIPLES OF RESISTANCE SEAM WELDING

Before an introduction is given on High Speed Resistance Welding a treatment is given to similar processes. HSRW can be considered part of a family of processes known as Seam Welding. [Schuler, 1977] gives a brief overview of the different variations of the basic process such as:

- Lap Seam Welding
- Flange Welding
- Mash Seam Welding
- Metal Finish Seam Welding
- Foil Butt Seam Welding
- Butt Seam Welding
- High Frequency Butt Seam Welding
- Bar Butt Seam Welding
- Controlled Path Resistance Welding

The above list is by no means exhaustive but gives an insight. The processes are grouped together because of a physical similarity between the respective processes' machinery; a whole new welding type is often born when a different

application requiring a slight change to the geometry of the equipment or lay-up of the work pieces is needed for a different application. E.g. work on Semi-Mash Seam Welding [Mitchell, 1973] developed from Mash Seam Welding gives a slightly better surface finish. *"Resistance Seam Welding – A continuous weld made between or upon over-lapping members, wherein coalescence may start and occur on the fraying surfaces or may have proceeded from the surface of one member. The continuous weld may consist of a single weld bead or a series of overlapping spot welds"*. This definition by [Schuler, 1977] intimates melting and solidification by his comparison to spot welding and frequently talks about it, as do other authors, so it is probably not strictly true to say that HSRW is part of this family as melting does not take place. HSRW does however share many of the same characteristics as other Resistance Seam Welding processes, most notably Mash Seam Welding. A basic introduction to MSW is given by [Bellotte, 1964].

The early work on MSW by [Begeman, 1955] and by [Funk, 1956] on uncoated autobody steel is concerned with similar process variables such as electrode force, welding speed, contact resistance and initial overlap. But from a modelling perspective the process is quite different; not only is the bonding between the sheets caused by the solidification of a weld bead, but because of the lack of a coating, the heat generation at the surface necessitates the weld to be flooded with water.

On first observation greater similarities could be drawn between HSRW and MSW of galvanized sheet steel [Allen, 1958][Westgate, 1984]. Crucial differences are the partial boiling away of the zinc coating, no use of an intermediate electrode and the slow speed of operation. So, process optimisation involves, for example, missing every tenth cycle in the AC current to stop excessive heat build up ahead of the weld gap whereas in HSRW this doesn't occur because the welding speed is so much faster than the rate of heat diffusion. Melting that takes place during MSW places a limit on the maximum weld speed as pressure needs

to be applied to the liquid weld nugget as it solidifies to prevent casting defects such as shrinkage cavities and shrinkage cracks [Schuler, 1977]. Melting does not take place in HSRW for a sound weld. Zinc alloying with the copper electrodes and zinc build up on the surface results in fouling of the electrodes and is described as a major problem by [Allen,1958], remedies such as the introduction of an intermediate electrode are given in work by [Ganowski, 1972] and [Oldroyd, 1980].

2.2 High Speed Resistance Welding

High Speed Resistance Welding, also known as the Soudronic Wire Welding Technique, offers a high speed manufacturing route for the creation of continuous seam welds. Developed during the 1960's by Soudronic AG of Switzerland for the production of three piece can bodies, the technique sought to overcome the problem associated with welding tinplate, namely that of weld roll contamination with the coating metal [Williams, 1977, part I]. Impetus for the method's genesis also came from the need to reduce the lead content of food and therefore to replace the previous method of can body production namely soldering. The HSRW process began to replace significantly the soldering production method in the early 1970's [Renard, 1992]. Since the conception of the technique productivity has risen from 15 m min^{-1} to 115 m min^{-1}, the driving force for these improvements being competition from other packaging mediums.

Three piece cans comprise three pieces; a body, a top and a base. The base and the top are both formed by pressing sheet steel blanks. The vast majority of the machines for the production of three piece can bodies are fully automated. In essence, the process takes flat sheet steel blanks, loads them into the machine where progressively one at a time they are folded over to form a cylinder before welding a leak tight continuous seam along the slightly overlapped edges.

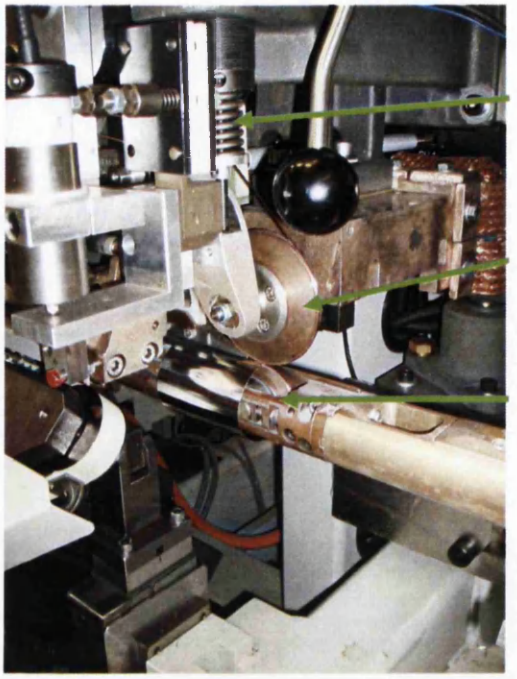

Figure 2.1: photograph of a Soudronic high speed seam welder modelled in this body of work showing the two electrodes, the upper one being spring loaded. A can body is placed between the two electrodes to demonstrate the movement of a can body. The can body would be fed through the electrodes causing it to move from left to right.

A HSRW machine is shown in Figure 2.1. After the blank has been overlapped to create a cylinder it is held by tooling to keep the overlap constant before being passed between the electrode wheels, this is done automatically. Before a weld is made the electrode wheels are in contact and are short circuiting. As the blank enters between the welding electrodes it forces them apart, there is contact between the electrode wheels and overlapped sheet so that an electrical current is caused to flow through the steel. The current causes Joule Heating sufficient enough to turn the steel into a plastic state. During this plastic state the material is forged together creating a solid state weld [Phillips, 1960]. No filler material is needed.

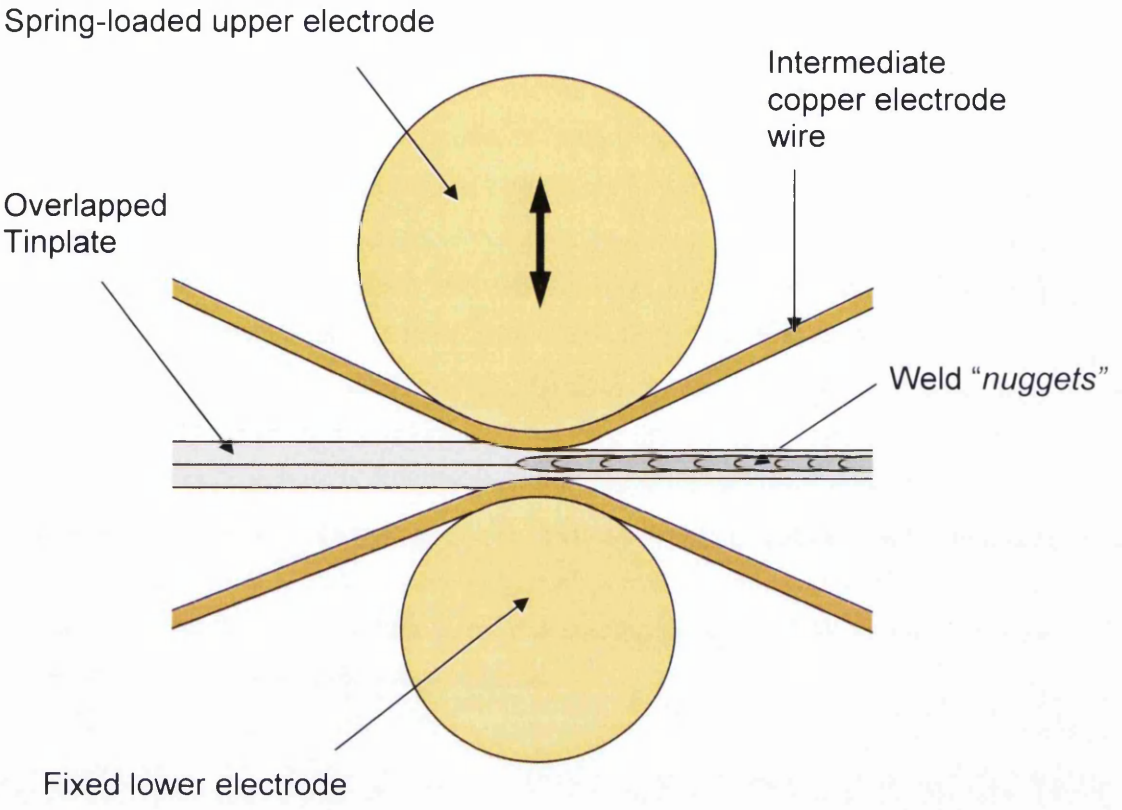

Figure 2.2: schematic diagram of the components that are the main consideration in this model. The basic fundamentals are shown as the tinplate moves through the electrodes from left to right.

As depicted schematically in Figure 2.2 the copper alloy electrode wheels do not directly come into contact with the material to be welded due to the presence of a continuous feed of intermediate copper wire. This feature of the machine is to prevent the electrodeposited protective tin coating on the steel contaminating the electrodes by continuously replacing the contact surface [Westgate, 1980]. The consumption of this copper wire typically represents around 30 – 60% of welding cost [Schaerer, 1984] thus placing pressure on the method to be substituted by Laser Seam Welding for example [Church, 1986]. High copper prices of late only increase this pressure, though some solace is brought by the fact that the copper is resold as scrap for approximately 80% [Westgate, 1980] of the value that it is bought for.

As the material passes between the electrodes the current alternates. As Joule Heating is proportional to the square of current density, the peak of the welding current creates the highest degree of heating and roughly the centre of a weld "nugget". Each so-called nugget is not analogous to a single Spot Weld, because it is not thought that melting and solidification takes place, rather a forging together of austenitic steel in the plastic state to create a metallurgical bond. This is the same principle used in Roll Welding when cladding mild steel with aluminium [Manesh, 2005] or Hot Roll Bonding [Brick, 1970]. The basic principle of the process is to form a continuous band of overlapped weld nuggets. There is a limit to the speed of welding because to create a water-tight seal with adequate strength the nuggets need to overlap. There is also a limit to the AC frequency that each machine can operate at, so the welding speed is limited by this as well as other process variables described later.

2.3 Welding Latitude

The welding latitude, or lobe, is the welding current range over which a weld is determined to be sound. The welding lobe is often referred to in resistance welding; the greater the welding lobe the better the weldability. Welding latitudes are often represented on a graph with, say, electrode force or weld speed along the x-axis and welding current along the y-axis.

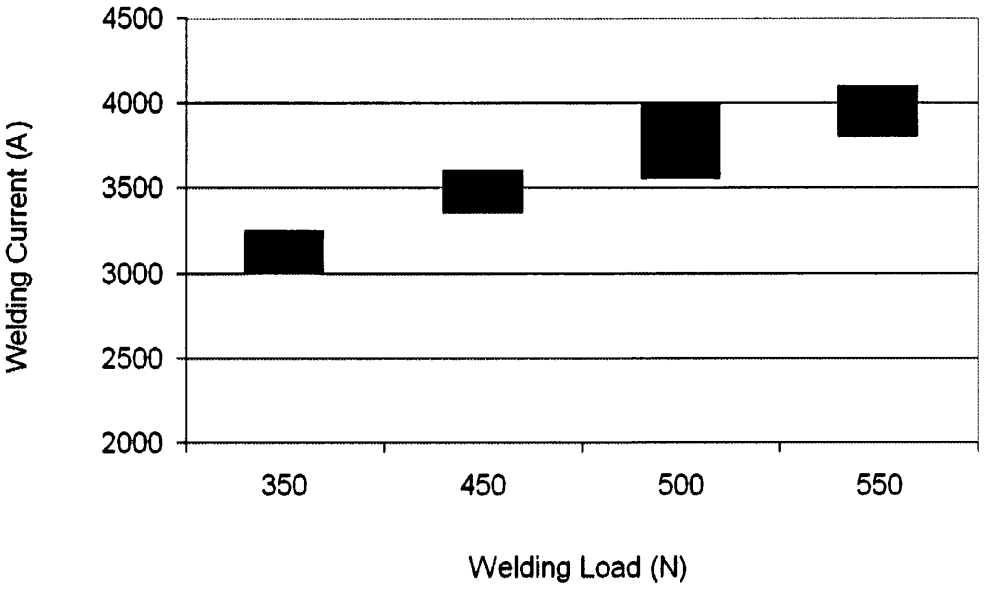

Figure 2.3: typical welding latitude showing the non linear variation in welding currents over which sound welds form.

As an example Figure 2.3 shows the welding latitude derived from experimental data. The lower limit below which a *cold weld* is formed is determined by the weld failing a rip test. A rip test is a test that tries to pull out a weld from the formed can body using special pliers, indicating that the weld is stronger than the base material. See Figure 2.4 below.

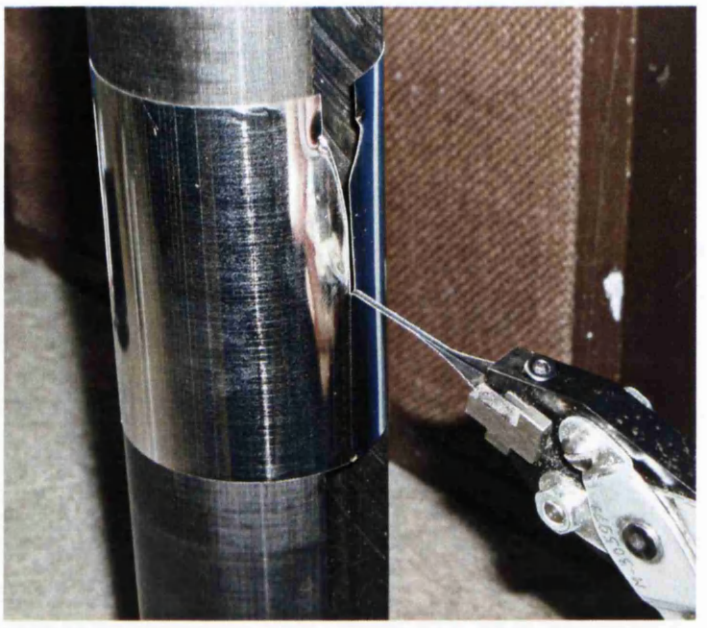

Figure 2.4: picture of a rip test where the weld is pulled out from the can body to indicate strength using specially adapted pillars.

The upper limit is represented by the current above which splash occurs. Splash defects are typically molten material expelled from the weld gap due to undesirable melting and is described later. When producing these plots all other settings are held constant and only the current is changed.

2.4 Process Factors Affecting Weld Quality

2.4.1 Contact Resistance

Joule Heating is caused by the passage of electric current through a resistive medium, the moving electrons colliding with atoms of the material through which they pass transfer energy to them in the form of heat. Due to the imperfect contact at surfaces the surface resistivity is often significantly higher than the bulk resistivity of components in contact. This is because the surface of the components in contact will not be atomically smooth so there is a reduced area

of contact through which electrons must pass. Also it can be the case that the surface is not perfectly clean, i.e. there is an oxide layer present or other material deposited upon the surface such as grease. [Simon, 1992] details the importance of surface roughness when determining contact resistance. Tinplated steel is used for HSRW as tin has a low melting temperature and thus reduces the contact resistance by wetting the surface as well as being electrochemically more noble than iron, preventing surface oxidation.

It transpires that this causes the heating to be more pronounced at the interfaces of the electrode/material and the sheet/sheet interfaces. The classic theories on contact between two surfaces have been proposed by [Holm, 1967] and [Greenwood, 1966, I and II]. The value of the contact resistance itself does not remain constant; it is dependent upon such factors as the coating material, the coating weight, welding load and the temperature of the components in contact. It is also worth noting that as the temperature quickly rises to a level sufficient to melt the coating metal, as this takes place the surface/contact resistance will change abruptly and this has important consequences for how it is dealt with numerically. This is also the case when the bonding of the two sheets takes place; they behave more as one body rather than two bodies in contact so the local resistance will abruptly reduce to the value of bulk resistivity.

[Ichikawa, 1988] discusses the importance of contact resistance to mash seam welding. The paper goes as far as stating that high electrical contact resistance results in poor weldability. A relationship is displayed in Figure 2.5 that proposes a relationship between weldability and the contact resistance of the coated strip. Tinplate, ECCS and Ni coated steel are all evaluated and the paper concludes by stating the best welding latitudes are possessed by tinplate with the smallest contact resistance.

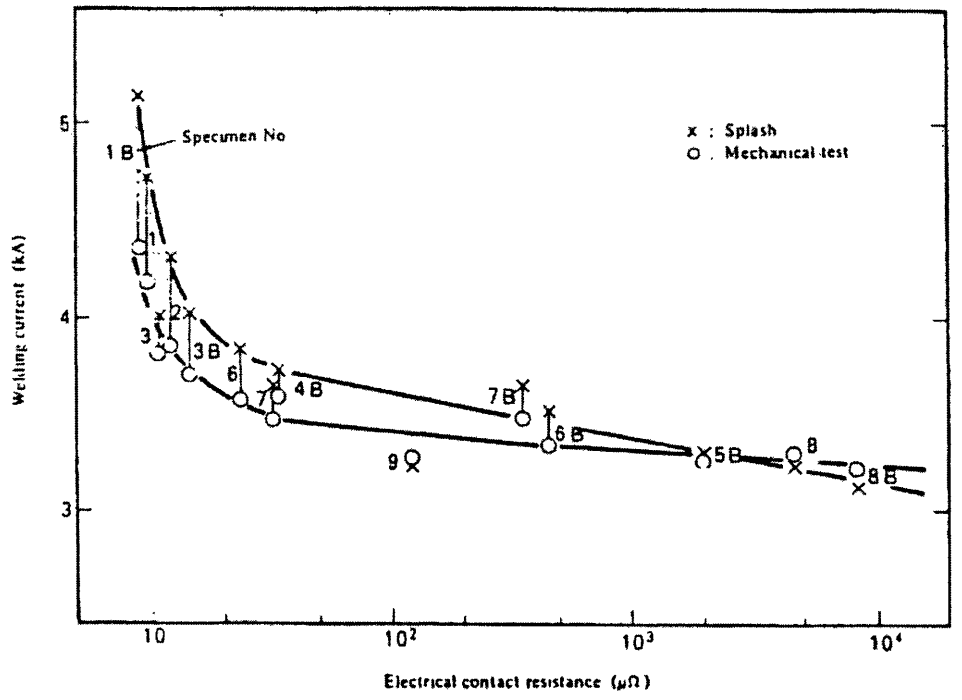

Figure 2.5: welding current vs. electrical contact resistance [Ichikawa, 1988].

[Sodeik, 1988] goes into detail by describing the general effect of coating weight on the weldability of tinplate. Figure 2.6 is taken from the aforementioned paper and summarises the author's findings; a reduction in coating weight is accompanied by a reduced welding lobe. [Waddell, 2001] outlines the same concerns. This is particularly interesting due to the fact that a coating metal is not only required to impute corrosion resistance, but also weldability. The increase in weldability is down to the fine coat of tin reducing the contact resistance [Ichikawa, 1988]. [Haigh, 1982] describes how the use of tin to plate the welding wire can be beneficial to the weldability by lowering the sheet/electrode contact resistance.

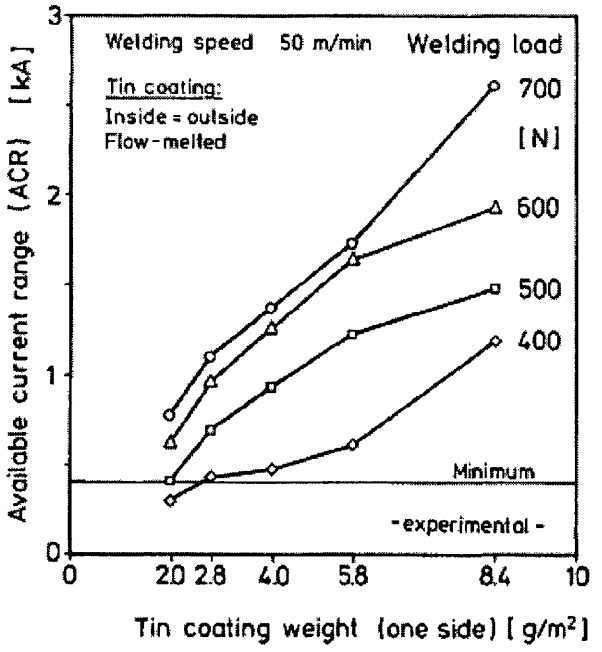

Figure 2.6: tin coating weight vs. available current range [Sodeik, 1988].

The general consensus is that black plate, i.e. uncoated steel strip, is unweldable [Haigh, 1982][Asano, 1985] because of the oxides occurring at the surface. [Asano, 1985] expounds that by removing these oxides by grinding and polishing or similar a marked increase in weldability is witnessed. Too high a coating weight can be detrimental to the weld quality because intergranular cracking can take place. Intergranular cracking takes place in the heat affected zone and is attributed to the penetration of tin along the ferrite grain boundaries [Williams 1977, part II, and Williams, 1973]. But this effect is only witnessed above the weldability lobe, so should not be seen as so much of a problem. Shunting [Bellotte, 1964] of the welding current can occur for higher coating weights [Williams, 1973] causing current to flow at the interface significantly in front of the weld gap, reducing current density. The type of thermal treatment given to the coating can also be of interest [Waddell, 2001]. This influences the contact resistance of the strip steel by altering the ratio of tin to iron-tin intermetallic in the coating.

Of particular interest is the work of [Shimizu, 1998] who records that the total contact resistance, that is the sum of the surface resistance as a proportion of total dynamic resistance, is correlated with the weldability lobe. A larger contribution from the contact resistance to the total resistance results in a smaller weldability lobe. Intuitively this notion seems sensible because contact resistance is a source of local heating at the interface when current is passed and in turn raises the energy state of atoms at the interface. This increases the propensity for the thermally assisted bonding to take place, but too intense heating can cause the steel to melt at this interface resulting in the early onset of splash. The heating is so intense when blackplate is welded that there is effectively no welding latitude because the splash condition is reached before sound welds can be produced.

2.4.2 WELDING LOAD

The use of lower tin weights reduces the weldability lobe [Sodeik, 1988][Waddell, 1986], but these authors similarly state that an increase in the weldability can be caused by increasing the welding load i.e. the load applied by the spring mounted upper welding electrode. This affects the contact resistance by causing it to decrease, see Figure 2.7. Consideration of Figures 2.6 and 2.8 reveals the beneficial effect that this has on the weldability of light tin steels. [Sodeik, 1988] does draw attention to the dangers of 'over mashing' the seam by the use of a high welding load and recommends the use of tooling to govern the maximum mashing of the weld seam.

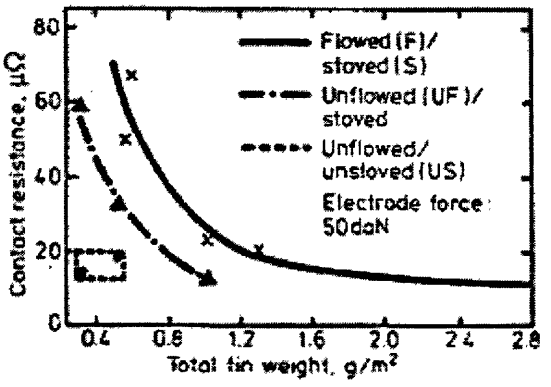

Figure 2.7: contact resistance vs. total tin weight [Waddell, 1986].

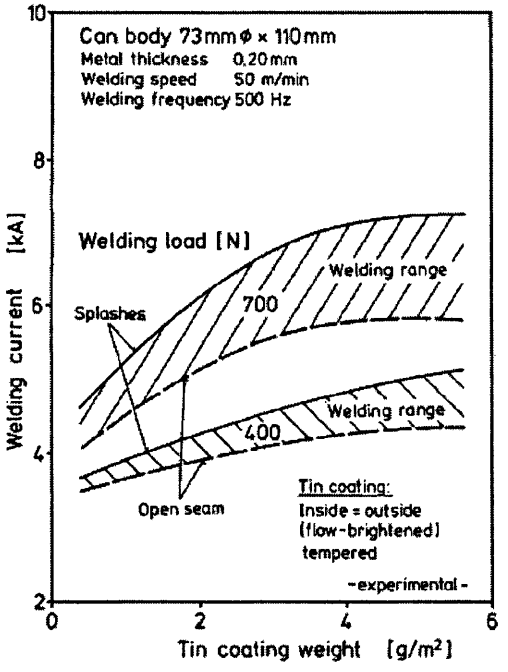

Figure 2.8: welding current vs. tin coating weight [Sodeik, 1988].

2.4.3 WELDING SPEED

Westgate discusses, in part, the typical current schedules used during HSRW. The heat distribution during welding is a direct result of the varying flow of

electrical current with time. The heat affects the plasticity of the material and so also the extent of deformation and forging together of the two sheets. The AC current waveform is of primary importance; this is especially true when the exact waveforms applied by welding machinery can be different from those expected, viz the current *spikes* associated with solid state frequency converters often differ from an expected theoretical smooth sine wave form.

A high welding speed is crucial to the commercial success of mash seam welding; increasing the welding speed increases the number of cans produced per min thus reducing the production cost of each can body. At each half cycle in the AC current waveform a weld "nugget" is formed, so at 50 Hz a maximum of 6000 weld nuggets can be produced every minute. This imposes a maximum welding speed because as the speed is increased the spacing between the nuggets is increased also. So there becomes a point where the nuggets do not overlap sufficiently to create a sound weld. [Williams, 1977, part II], explores this. It becomes apparent that as the welding speed is increased, the frequency of the AC current needs to do so too. On old machines that use a 'rotary frequency converter' the frequency is fixed so there is less flexibility to adjust nugget pitch.

However, as the weld speed increases, the time available for each weld to form diminishes. This has the effect that the amount of energy transferred to the material as heat and therefore the maximum temperature attained are reduced. This has obvious consequences for the formation of the solid state weld nuggets; there becomes a point where the weld is not fully formed. To compensate for this the weld current needs to be increased so sufficient heating of the material takes place allowing for adequate plasticity of the steel and, as the solid state weld needs to form in less time even more heat input is required to reach the higher temperatures necessary. As the welding current increases however, the likelihood of Splash increases and it is even possible for the current carrying capacity of the sheet to be exceeded resulting in the burning of the sheet [Williams, 1977, part II].

An early investigation by [Lavery, February 1970][Lavery, March 1970] concludes that higher welding speeds (100 Hz compared to 50 Hz) increase the hardness of the weld and can cause problems with further forming operations such as flanging because of possible embrittlement. Further investigation of this at 150 Hz by [Chatterjee, 1971] showed that the increase in hardness was less pronounced when compared to welds at 100 Hz and that in all cases the increase in hardness did not impart brittleness to the weld; all welds were indeed stronger than the strip but remained sufficiently tough that when burst testing cans to destruction failure never occurred at the seam.

[Elzinga, 2002] states that there is a non linear variation in the welding latitude with welding speed; notably that at 80 m min^{-1} there is a drop in weldability when compared to speeds below and above this value. This result highlights the inconsistent and complex behaviour of the machine for some settings. [Gregory, 1985] stipulates the need for tighter control on tinplate thickness as speed is increased as the geometry of the weld stack up is of prime importance to heat generation patterns.

2.4.4 Overlap

The overlap of the weld stack up is an important process parameter and much effort by the manufacturers of canwelders has been made to control this process variable and keep it consistent. A typical production value for pre-weld overlaps is 0.5 mm on modern machines. Published works [Schuler, 1977][Funk, 1956] state the need to control overlap width because of heat generation sensitivity, and excessive or deficient heat generation will knock out other process variables because of their interdependency.

2.4.5 MATERIAL GRADE

The material grade used has a very profound effect on the weldability of tinplate and welding latitude. Can producers are keen to reduce the gauge of tinplate used, and changing this changes the weld geometry. The thesis of [Suthar, 2005] showed how dramatic the effect was when the weld gap was changed and postulated that the weld geometry change affected the current density which in turn changes heat generation and mechanical properties etc.

Carbon content has been shown [Williams, June 1975] to deleteriously affect the weldability lobe of tinplate of constant thickness. The increased carbon content also increases the resistivity of the steel, thus higher welding current is needed to maintain weld nugget size. Martensite forms in the weld and heat affected zone whereby the hardness of the weld is increased; a higher carbon content of the tinplate causes the martensite that forms to be harder making the effect more pronounced.

During the production of tinplate, after electrolytic plating of metallic tin, the *flow melting* of tin takes place to improve surface finish and bonding of the tin layer to the steel substrate. The extent to which this occurs will affect the microstructure of the coating, and therefore the contact resistance, see Figure 2.7. Tin needs to be removed before a sound weld can be formed [Blom, 2006] and the higher proportion of Fe/Sn intermetallics present after flow melting will hinder this as the intermetallics have a much higher melting temperature, see Figure 2.9. Intermetallic volume fractions also increase after the necessary *lacquer baking* step in can body manufacturing [Asano, 1985].

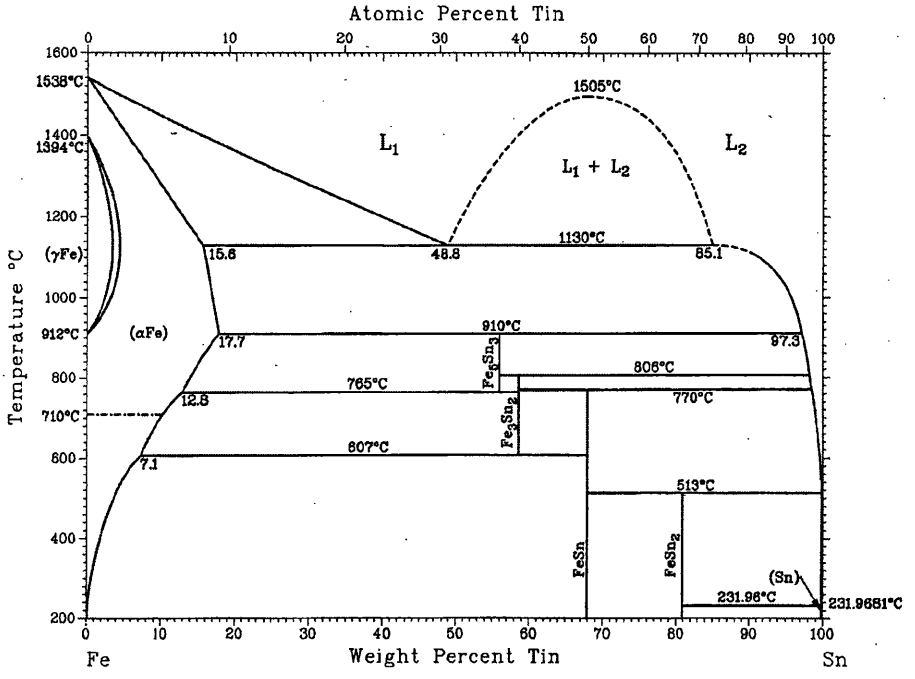

Figure 2.9: iron-tin binary equilibrium phase diagram [Okamoto, 2000]

[Hiroki, 2004] states that the Tin Free Steel for packaging applications available on the market, namely Electro Chromium Coated Steel (ECCS), is unweldable. The thin chromium hydroxide layer on top of the metallic chromium layer has a very high electrical resistivity and as such causes strong localised heating at both the strip/electrode interface and the strip/strip interface making stable welding impossible without first removing this chromium hydroxide layer. [Nakakoji, 1987] reflects the same difficulties with ECCS but some slight improvements in weldability were noted if the electrolysis process is reversed slightly causing formation of a surface low in chromium oxide/hydroxide.

2.5 Successful High Speed Resistance Weld

Manifold factors, properties and settings affect the quality of a High Speed Resistance Weld. The main parameters pertinent to a model of the process have

been discussed and now the following section describes the ideal weld that is sought by canmakers. A successful weld has to possess certain attributes:

- sufficient strength to pass a rip test
- surface free from splash or severe roughness that could impair corrosion performance
- sufficient ductility for subsequent forming operations such as flanging, double seaming and beading
- freedom from internal defects such as commas or porosity (described below)

Figure 2.10 shows a successful mash seam weld. This photomicrograph shows how the two sheets have combined resulting in a continuous microstructure. This seam would be sufficient for application. This contrasts with Figure 2.11 where the two sheets still remain separate. This weld may not be gas tight under pressure, would not pass a *rip test* and would be more susceptible to corrosion so is clearly unacceptable.

A HSRW machine has to be set up to create a weld of sufficient quality, a deviation from the welding parameters or *drift* can result in an unacceptable weld being produced. A weld is typically 1.4 times the original sheet thickness and is said to be *overmashed* when this figure drops below 1.3 or so.

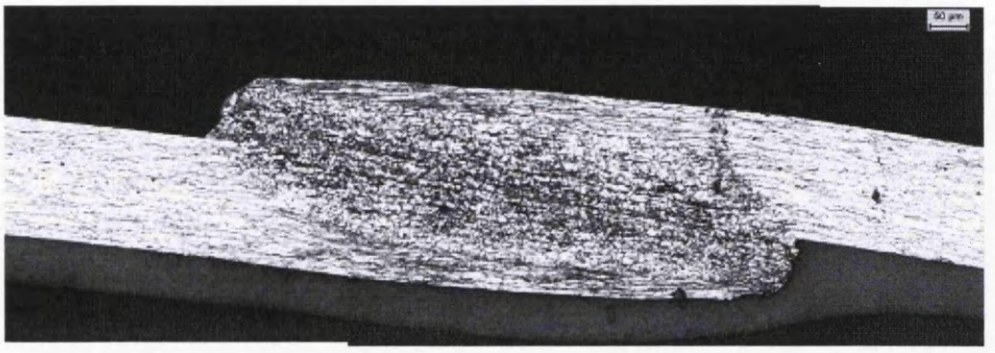

Figure 2.10: photomicrograph of a sound High Speed Resistance Weld showing the heat affected zone [Elzinga, 2005].

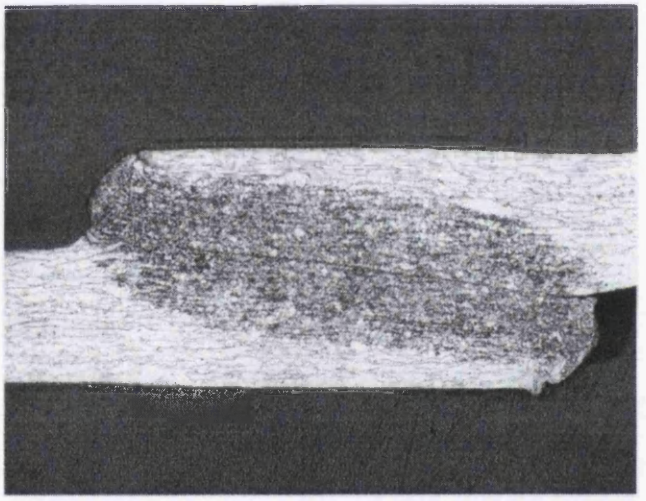

Figure 2.11: photomicrograph of an incomplete High Speed Resistance Weld [Elzinga, 2005].

[Blom, 2006] postulates that for a successful seam weld the tin layer must be at least partially broken up and removed during the formation of the weld, if not completely. The tin is driven to the edges of the weld seam by the pressure exerted by the welding load leaving behind two clean surfaces in intimate contact that can be mashed together to create the seam. The tin is given more time to displace when the welding load is reduced and the current is increased and also when the speed is reduced. Small amounts of tin remain after welding with any

machine settings as Fe/Sn intermetallics have high melting temperatures and adhere to the substrate, and very limited diffusion of tin is witnessed.

[Allen, 1968] also suggests that metallic coatings, in this case zinc, are pushed away by electrode pressure. The difference between tin and zinc coatings is the low boiling point of zinc when compared to tin, 907°C and 2269°C, respectively. In spot welding of galvanised steel the zinc can be caused to boil, whereas the likelihood of this happening with tin is much less. [Allen, 1986] agrees with this mechanism and states that for zinc coated steel the electrode pressure forces the molten zinc away from the weld area during the first stages of the heating paving the way for a solid state bond to take place.

With regard to the underlying steel substrate the bonding is a solid state process; Solid State Welding is defined by the American Welding Society as *"a group of welding processes which produce coalescence by the application of pressure at a temperature below the melting temperature of the bases metal and filler metal"* [Linnert, 1994]. [Linnert, 1994] also gives a brief description of the method and states that two obstacles must be overcome before a bond takes place. Typically, smooth metallic surfaces still have surface asperities hundreds of atoms deep and are covered in an oxide layer and other contaminants. It is these obstacles that need to be removed to allow sufficiently intimate contact between the mating surfaces and subsequent coalescence to take place.

The asperities are an important feature in the HSRW process for they cause the surface to have a series of microcontacts responsible for the contact resistance: this will be given further treatment in the model formulation section. The influence of surface films is dealt with by [Tylecote, 1958]. The authors suggest that not only are oxides present but occasionally sulphides, hydrated oxides or even carbonate films as a result of process conditions. The necessity of pressure and deformation was cited as important because the deformation breaks up the

surface films and thus allows bare metal to be exposed and participate in metallic bonding.

An interesting theory is proposed by [Mohamed, 1975] involving the thermodynamics of solid state welding. An energy barrier is suggested as being present due to one or a combination of several factors because even when two clean surfaces are brought into contact a weld does not spontaneously form; energy in the form of pressure and heat are required. The energy barrier is suggested to be due to recrystallisation, diffusion or crystallographic miss-matching.

Solid state bonding mechanisms are investigated by [Eizadjou, 2008] and by [Wright, 1978], both works specifically relating to cold/warm pressure welding by rolling bonding. [Eizadjou, 2008] conducted peel tests of samples subjected to different process parameters and found an increase in the strength of the bond when there was an increase in any of the following; a) the amount of thickness reduction, b) the temperature of welding, c) the pressure of the weld or d) the time taken to weld. [Wright, 1978] proposes similar ideas but also mentions a theoretical maximum strength related to the remaining contaminated areas in the formed weld. The strength of the weld is a function of the amount of virgin metal exposed by the creation of new surface area as thickness reduction takes place because it is only this virgin metal that participates in solid state bond formation. Work similar to this was conducted by [Gould, 2003] on Mash Seam Welding. [Gould, 2003] states that creation of new surfaces plays a significant, but reduced, part in bonding. Cold pressure welding of aluminium requires approximately 400-500% strain whereas in Gould's calculations MSW is suggested to produce straining of the order of 110%. Cold pressure welding of aluminium would require more virgin metal to be exposed because of the Alumina on the surface whereas the steel substrate has very little oxide on the surface in comparison. Processes such as diffusion, oxide dissolution, and recrystallisation purportedly contributed much more to bond strength. [Gould,

2003] found that a critical time was required above a critical temperature and thus concluded that the thermally activated processes were dominant as a formation mechanism.

[Blom, 2005] also proposes a mechanism of solid state bonding in HSRW; a necklace of grains nucleates at the two surfaces to be joined and subsequently grow into both sheets. Partially formed welds just below the lower welding limit have a string of freshly nucleated grains at the surface; these then have greater opportunity to grow further when higher welding currents are used, creating a sound solid state bond. This recrystallisation is stated as happening by [Davies, 1993] in combination with atomic diffusion during the formation of pressure welds.

2.6 Defects

After discussing a successful High Speed Resistance Weld it seems appropriate to discuss when machine set up is less than adequate, or rather less than adequate for the particular machine because the same settings applied to different machines frequently do not produce replicable welds. HSRWs have two main defect types, the comma and splash.

2.6.1 Splash

Splash is caused by the ejection of molten metal from the seam weld, and there are two possible explanations for its formation. The first relies on the fact that the weld nugget is molten metal surrounded by solid and it is suggested that a combination of factors causes the weld nugget to grow to such an extent that the solid containing it can no longer do so. Alternatively the liquid is formed only

when splash occurs by the application of too much current for the set up of the machine. The ejected material is seen as a roughening of the inner side of the can body and gets progressively worse until clear spats are seen, Figure 2.12. [Asano, 1985] states that splash is caused by abnormal heat generation at the surfaces due to the contact resistance present at the interface.

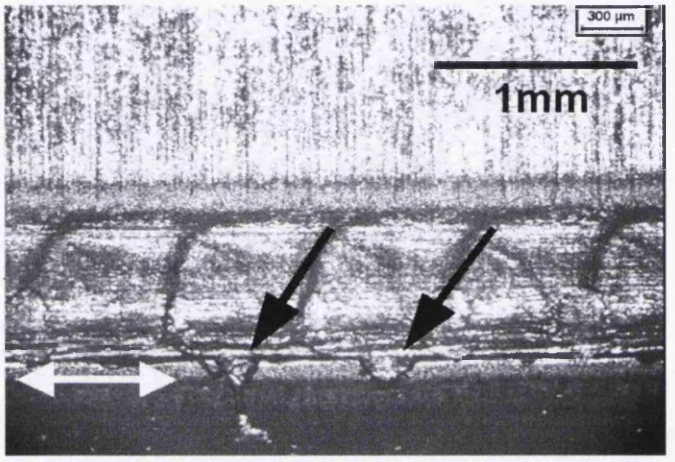

Figure 2.12: photograph of the splash defect. The white arrow is the nugget length and the black arrows are the splash [Elzinga, 2005].

[Williams, 1977, part I], discussed the causes of splash and suggested that poor mating of the surfaces to be welded as a result of low welding loads was one cause. Also poor surface finishes can encourage splash formation. Much the same conclusions were reached by [Jacques, 1968] in that poor mating of the surfaces to be joined, low weld load, excessive welding speeds and currents causes splash.

2.6.2 Commas

Comma formation is an area of debate. Figure 2.13 shows a comma defect in a transverse micrograph of a seam weld. Commas are porous features of

characteristic shape caused when the welding current is high or the rolling force is low [Waddell, 2001].

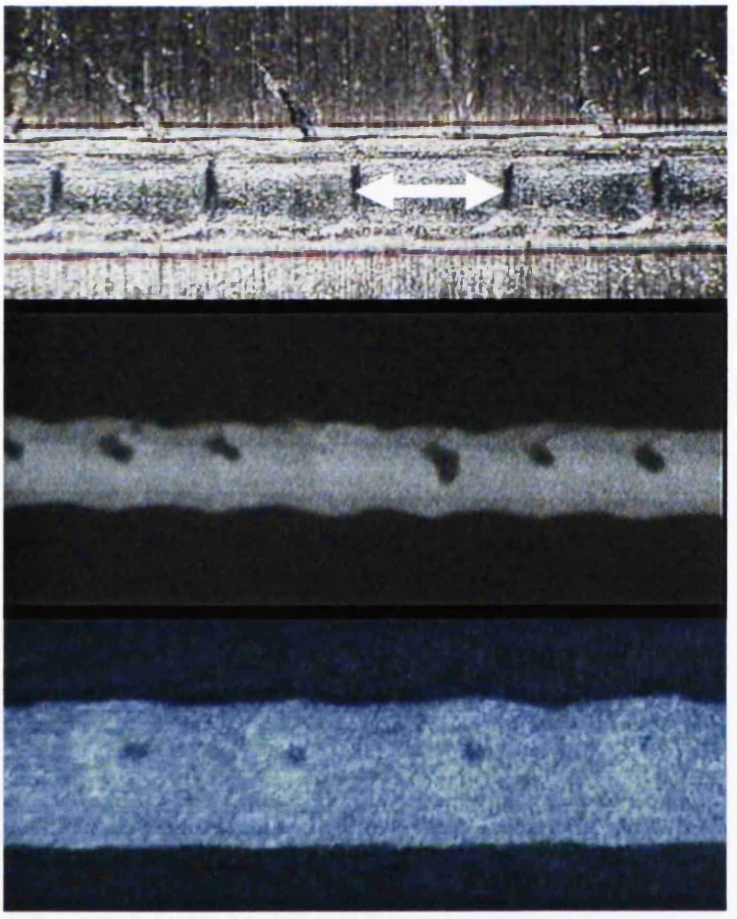

Figure 2.13: the comma defect photograph and x-ray images. The white arrow is the nugget length [Elzinga, 2005].

Commas characteristically form when the heat generation becomes uneven, and they form as curved areas of high heat input toward the smaller lower electrode. Severe commas form after what is assumed to be molten metal expulsion.

[Elzinga, 2002] notes the greater susceptibility to comma defects of welds produced on a machine with a solid state *Unisoud* frequency converter in comparison to a *Rotary* frequency converter. [Elzinga, 2002] also states that commas are much more prevalent at higher welding speeds. [Boyd, April 1981]

observes that the comma is situated within the zone of most rapid cooling, just below the weld crest, and that their inner surface appears glazed as though the molten state was attained.

2.6.3 Shrinkage Cavities

Shrinkage upon solidification of the tinplate results in shrinkage cavities. [Williams, 1977, part I], observed that very few welds were free of porosity, but these welds are produced at lower speeds in combination with higher current where melting often takes place. Modern welding practices do not use such settings; higher speeds where welds show no sign of melting and solidification are free from this porosity and so this defect seldom occurs with modern machines. Figure 2.14 shows a shrinkage cavity.

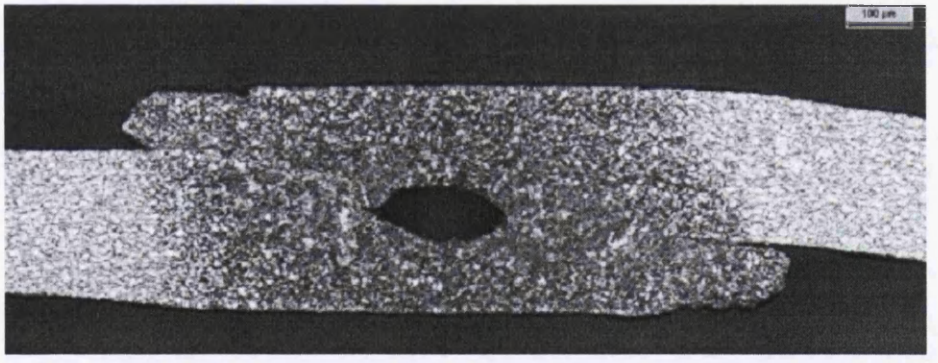

Figure 2.14: photomicrograph of a shrinkage cavity [Elzinga, 2005].

Shrinkage cavities are not typically found in HSRW due to the fact that there is no melting taking place for acceptable welds; they are much more of an issue for Mash Seam Welding. Shrinkage cavities occur without the constraint of welding load and can be avoided by allowing the weld to cool slightly whilst under pressure from the welding load, ergo forging back together the internal pore surfaces.

2.6.4 Cold Weld

Cold welds result where there has not been enough heat input into the weld and no solid state metallic bonding or grain growth across the interface results. As tin melts at 232 °C the low heat input can melt this surface tin and cause it to re-solidify and solder the can body. This defect is identified by the *rip test* as the joint is weak and comes cleanly apart.

2.7 Numerical Modelling

2.7.1 Electro-Thermal Effects

An important aspect of the HSRW process, like many other welding methods, is the electro-thermal effects. The numerical modelling of the transient thermal field is important because an increase in temperature is accompanied by a decrease in mechanical properties, and it is this that gives the final HSRW seam its characteristic undulating surface shape. Not only this, but it is the elevated temperatures that supply the energy to allow the solid state bond to form. The different stages in calculating the electro-thermal fields in the model are now described from electrical potential field up to the Joule heating source term.

2.7.2 Electrical Potential Field

The electrical potential field is described using the Laplace equation. In any given time step the electrical potential is modelled as instantaneously reaching equilibrium. In three dimensions,

$$\frac{\partial}{\partial x}\left(k_{ex}\frac{\partial V}{\partial x}\right)+\frac{\partial}{\partial y}\left(k_{ey}\frac{\partial V}{\partial y}\right)+\frac{\partial}{\partial z}\left(k_{ez}\frac{\partial V}{\partial z}\right)=0 \qquad (2.1)$$

Where V is voltage (V) and k_e ($\Omega^{-1}m^{-1}$) is temperature dependent electrical conductivity in each of the three Cartesian directions. If $k_{ex}=k_{ey}=k_{ez}$ they may be eliminated to leave,

$$\nabla^2 V=0 \qquad (2.2)$$

2.7.3 Current Density

The current density vector, i (Am^{-2}), is important in determining the extent of Joule Heating. Current density is the subject of some research [Elzinga, 1996-1997] because of its importance with respect to heat generation within the weld; the smaller lower electrode has a smaller contact area and therefore a higher current density and regions closer to it are subject to more heat generation. Current density is the differential of the potential field and has both magnitude and direction, which is negative to the voltage gradient,

$$i_x=-\frac{1}{\beta}.\frac{\partial V}{\partial x} \qquad (2.3)$$

Where β is temperature dependent electrical resistivity (Ωm) and V is voltage. This term is used to provide a *source term* added to the transient heat transfer equations described next.

2.7.4 TRANSIENT HEAT TRANSFER

Steady state heat transfer can also be modelled using the Laplace equation, but in this problem the evolution of the heat field over time is of interest so the Fourier equation is used,

$$\frac{\partial T}{\partial t} = \nabla\left(\frac{k_e}{\rho c}\nabla T\right) \tag{2.4}$$

This is the three dimensional Fourier equation, where T is temperature (°C), t is time (s), ρ is temperature dependent density (kg m^{-3}), k_t is temperature dependent thermal conductivity ($Wm^{-1}K^{-1}$), c is temperature dependent specific heat capacity ($Jkg^{-1}K^{-1}$) and x, y and z (m) are the three Cartesian directions. Here the thermal conductivity is assumed to be isotropic. To make the Fourier equation describe fully the thermal situation under application of a voltage the equation needs to be modified by taking into account current density and latent heat evolution that takes place during solidification and melting,

$$\frac{\partial T}{\partial t} = \nabla\left(\frac{k_e}{\rho c}\nabla T\right) + i^2\frac{\beta}{\rho c} + \frac{H}{c}\frac{\partial f_s}{\partial t} \tag{2.5}$$

Where i is current density H is latent heat of fusion (Jkg^{-1}) and f_s is the volume fraction of solid (dimensionless), which ranges from 0 to 1. The equation can be applied in finite difference as well as finite element and this particular version of the equation is commonly used in spot welding and vacuum arc re-melting models.

2.7.5 MATERIAL PLASTICITY

The theory of Plasticity is used to describe a material's behaviour when it no longer obeys Hooke's Law. Plastic deformation is non-reversible on unloading. The first mathematical treatment of plastic strain was by Lévy and Saint-Venant in 1870 and has subsequently progressed into a detailed science. Further early work is described by [Hill, 1950]. Plastic redistribution of the steel takes place in HSRW as the two separate strips of tinplate are *mashed* together at elevated temperature to create the seam weld.

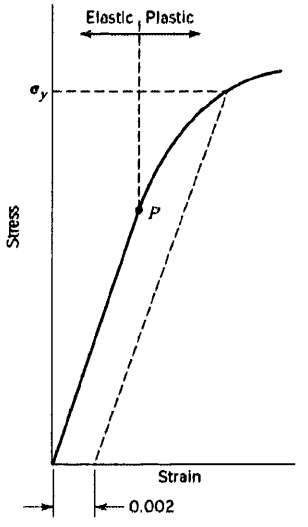

Figure 2.15: stress-strain curve outlining the plastic deformation numerically modelled in this model [Calister, 2001].

Figure 2.15 shows typical tensile behaviour of a metal whereby it behaves elastically and has a gradual transition to plastic behaviour at point P. At this point the material is said to yield and the stress at which yield takes place is called the yield strength. At higher temperatures yielding is easier and consequently takes place at a lower stress. This concept is important in HSRW because the Joule Heating Effect takes place due to the passing of an AC current through the can body blank when it is welded. The characteristic shape of the weld is due to this sensitivity of the yield strength to temperature. The

constant shape change of the overlapped strip subsequently has ramifications for the current density; geometrical features such as sharp corners cause current densities to become high and it is the current density that provides the heating.

2.7.6 Dislocations

From a microscopic perspective a metal is a polycrystalline aggregate; each crystal being of differing shape, size and orientation having formed from individual nuclei when the metal was originally cast. Recrystallised polycrystalline material, where no previous deformation has been applied to it, will behave in an isotropic manner. Deformation, for example by rolling, orientates the crystals causing the material to be anisotropic. On the atomic scale, deformation within these microscopic crystals is the breaking and remaking of interatomic bonds of many atoms as they move relative to one another.

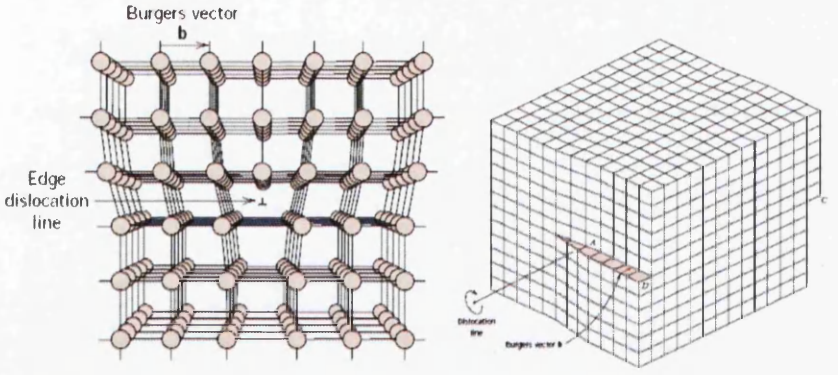

Figure 2.16: metal deformation in single crystals by slip, Edge dislocation (left) and Screw dislocation (right) [Calister, 2001].

For crystalline materials such as metals this process is called slip and involves the movement of dislocations, shown above in Figure 2.16. In the simulation of HSRW the movement of individual dislocations is not simulated neither is the

behaviour of individual grains, the material is assumed isotropic and homogeneous.

2.7.7 Yield Criteria

Mathematical criteria have been developed to approximate the stress at which yielding will occur. The von Mises criterion is often an acceptable choice for metals that obey the associated flow rule [Chakrabarty, 1987], and it is used regularly for metal forming processes such as forging and hot rolling. Before continuing with a derivation of yield criterion some basic notation needs to be clarified. The Cauchy stress tensor in Figure 2.17 can also be described as three principal stresses, Equation 2.6.

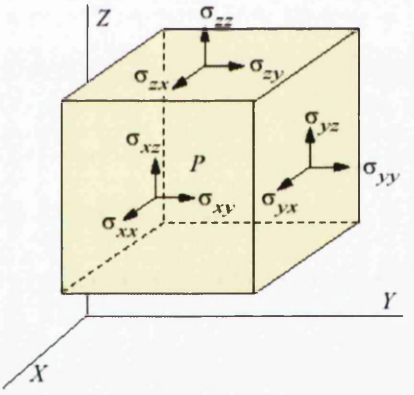

Figure 2.17: description of stress state at an infinitesimal point in a material.

$$\begin{bmatrix} \sigma_{xx} & \sigma_{xy} & \sigma_{xz} \\ \sigma_{yx} & \sigma_{yy} & \sigma_{yz} \\ \sigma_{zx} & \sigma_{zy} & \sigma_{zz} \end{bmatrix} \equiv \begin{Bmatrix} \sigma_1 \\ \sigma_2 \\ \sigma_3 \end{Bmatrix} \tag{2.6}$$

Richard Edler von Mises proposed his empirical law in 1913; that yielding would occur when a critical value, k^2, was exceeded by the second invariant of the stress deviator, J_2.

$$J_2 = k^2 \tag{2.7}$$

Where,

$$J_2 = \frac{1}{6}\left((\sigma_1 - \sigma_2)^2 + (\sigma_2 - \sigma_3)^2 + (\sigma_3 - \sigma_1)^2\right) \tag{2.8}$$

To relate this to a uniaxial tension test, where at yielding, $\sigma_1 = \sigma_0$ and $\sigma_2 = \sigma_3 = 0$ so,

$$\sigma_0^2 + \sigma_0^2 = 6k^2 \tag{2.9}$$

Rearranging,

$$\sigma_0 = \sqrt{3}k \tag{2.10}$$

Substituting Equation 2.7 into Equation 2.10 results in,

$$\sigma_0 = \frac{1}{\sqrt{2}}\left[(\sigma_1 - \sigma_2)^2 + (\sigma_2 - \sigma_3)^2 + (\sigma_3 - \sigma_1)^2\right]^{\frac{1}{2}} \tag{2.11}$$

This is the usual representation of the von Mises' equation [Dieter, 1988]. This failure criterion has remained widely accepted in this form as an invariant of the stress deviator. Because an isotropic material is described, the choice of axis must be independent from the yield criterion so an invariant function must be used. Moreover, experiments show that the yield strength of metals is independent of hydrostatic stress; pressure induced plasticity for example. It is for this reason that a stress deviator is used. It is also worth noting that the function is not dependent on the sign of individual stress invariants as square terms are in the criterion. When used in the FE code described in this thesis, the

failure criterion is referred to as a simple function, the Yield Function Y. The yield function is a function of the von Mises stress, σ_{vm} (Pa), and the yield strength, σ_{ys} (Pa). The yield function is greater than 0 at yielding and less than 0 when the material is purely elastic,

$$Y = \sigma_{vm} - \sigma_{ys} \tag{2.12}$$

2.7.8 Modelling of Physical Problems

A model of a physical problem is a simplification of reality to which established physical laws are applied. This simplification of reality allows reality to be simulated. In materials problems common methods of applying continuum physical laws are the Finite Element, Finite Difference and Finite Volume methods. Each method has its own advantages and disadvantages. A clear division of problems is often made by separating them in terms of both length and time scales. Because models are necessarily simplifications of reality detail at certain time/length scales is often missed. For example the simulation of a shaped casting process does not take into account the evolution of each and every single dendrite, but there are simulations that do exist for single dendrites. Likewise, the simulation of hot rolling on a 5 stand hot mill does not take into account the deformation of each and every crystal in the billet, but deformation of single crystals is most certainly an area of active research. Einstein once said "A model should be as simple as possible, but not simpler". This highlights the main objective when creating a model; only particular areas of interest and the relevant controlling physics will be contained in a model, needless detail will only increase the solution time. Finite Element Analysis was chosen to look at the deformation during HSRW along with the electrical and the thermal effects based on its ability to deal with arbitrary 3D geometries and its widely accepted superiority in numerical stress analysis problems.

2.8 Finite Element Method

The Finite Element (FE) method is one of many methods used to numerically model scientific and engineering problems and is particularly good at recreating component/workpiece geometry. It has been chosen to be used in this research for its ability to model electric potential, deformation and heat transfer, the main physics taking place during HSRW. FE has been applied to all manner of engineering problems and it is usually the method of choice for macro scale modelling of welding, rolling processes and forging to name a few examples. The following derivation, representation and notation follows that of [Desai, 1972].

2.8.1 Elements

For all manner of problems it is often easier to break the problem into simpler constitutive parts and evaluate these rather than the entire problem. This piecewise approximation is the basic philosophy of the FE method. The sub division of the object of interest into a finite number of elements i.e. Discretisation, is a process requiring engineering judgement. There is an array of element types to choose from, usually of simple geometry, for examples but by no means an exhaustive list of typical elements see Figure 2.18. The body of interest is divided into these elements by imaginary planes, the planes crossing at nodal points common to more than one element. It is these nodal points at which the equations are applied in the Displacement Model.

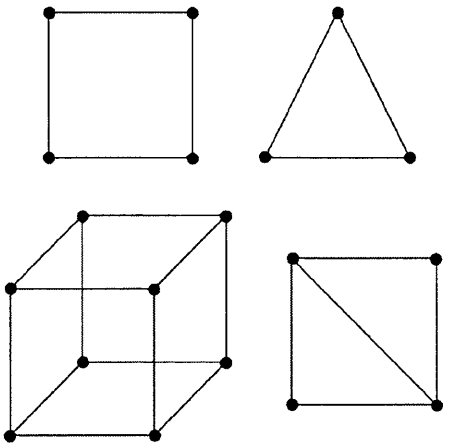

Figure 2.18: a selection of element types used with the Finite Element Method.

2.8.2 Isoparametric Elements

Isoparametric elements [Zienkiewicz, 1969] greatly simplify and generalise both the formulation of element stiffness and displacement models. Before the concept is made clear, two new concepts must be introduced; the Local Coordinate System and the Displacement Model.

2.8.3 Local Coordinate System

A local coordinate system defines the nodal positions within a single element. The positions within the whole body are defined by the Global Coordinate System. The type of local system most useful in FE is the Natural Coordinate System, as any point within an element can be described by a dimensionless number that is unity at only one primary node and zero at all others. This 'trick' allows for the method to be simplified and crucially allows for easy integration within the area/volume of the element. Figure 2.19 shows a linear quadrilateral, and how the linear quadrilateral is represented by natural coordinates.

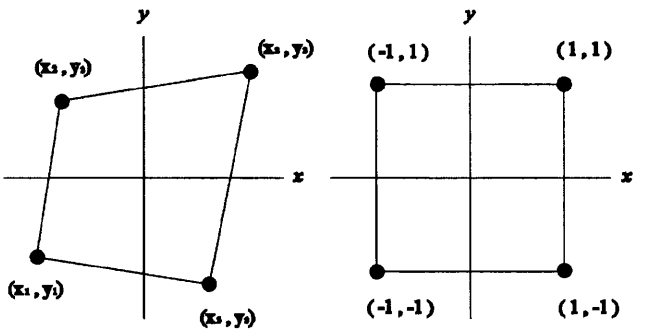

Figure 2.19: global (left) and local (right) coordinates.

To convert between the two coordinate systems one may use the formulae below,

$$\begin{Bmatrix} x \\ y \end{Bmatrix} = \begin{bmatrix} N_i & 0 \\ 0 & N_i \end{bmatrix} \begin{Bmatrix} x_n \\ y_n \end{Bmatrix} \tag{2.13}$$

Where,

$$N_i = \tfrac{1}{4}(1+ss_i)(1+tt_i)_{i=1\to4} \quad (2.14) \qquad x_n = \begin{Bmatrix} x_1 \\ x_2 \\ x_3 \\ x_4 \end{Bmatrix} \quad (2.15) \qquad y_n = \begin{Bmatrix} y_1 \\ y_2 \\ y_3 \\ y_4 \end{Bmatrix} \quad (2.16)$$

With x and y being the Cartesian coordinates (m), s and t being the natural coordinates, s_i and t_i being the natural coordinates (dimensionless) of nodes 1 to 4. Equation 2.14 is the *shape function* for a linear quadrilateral, Equation 2.15 is the x coordinates of the 4 nodes and Equation 2.16 is the y coordinates of the 4 nodes.

2.8.4 DISPLACEMENT MODEL

Discretisation of a continuum allows simple functions to be applied to the individual elements to govern their behaviour. When considering the behaviour of all the elements in the discretised body one gains an approximate solution to the expected behaviour of the assemblage of elements i.e. the problem in hand. Analysis of stress is the primary variable of concern in this project, thus it is displacement that is of interest and that will be assumed by a simplified function, the displacement model.

The nodal displacements necessary to describe fully the deformation of the element are known as the degrees of freedom of the element. For example a 4 node 2D linear quadrilateral will have 8 degrees of freedom. Shown below is a displacement model for a linear quadrilateral,

$$\begin{Bmatrix} u \\ v \end{Bmatrix} = \begin{bmatrix} N_1 & 0 & N_2 & 0 & N_3 & 0 & N_4 & 0 \\ 0 & N_1 & 0 & N_2 & 0 & N_3 & 0 & N_4 \end{bmatrix} \begin{Bmatrix} u_1 \\ v_1 \\ u_2 \\ v_2 \\ u_3 \\ v_3 \\ u_4 \\ v_4 \end{Bmatrix} \tag{2.17}$$

Here N_i is the shape function (dimensionless) shown in Equation 2.14 and u and v on the left hand side are the displacements at any point within the element of concern with the nodal displacements on the right hand side. Shape functions are usually described using the natural coordinate system, and when this is true the elements are particularly attractive because they are said to be Isoparametric.

2.8.5 Isoparametric Element Concept

Comparing Equation 2.13 and 2.17 one observes that they are of the same configuration,

$$\{x\} = [N]\{x_n\} \quad (2.13) \qquad\qquad \{q\} = [N]\{q_n\} \quad (2.17)$$

Isoparametric elements such as these are not only described using the same parameters but also they are of the same order, giving them the ability to describe both the geometry and the displacements of the element. This is attractive because such elements (of any order) satisfy both the requirements for completeness and compatibility. Isoparametric elements have the ability to become curvilinear by the use of a higher order polynomial shape function, allowing for the mapping between curved elements in the global domain and straight edged elements in the local domain. Using this quality of isoparametric elements it allows analyses of more complicated structures and/or loading with fewer elements, thus reducing storage and processing requirements.

2.8.6 Stress and Strain in Finite Element

It can be said that one of the most important aspects common to all forms of engineering is the analysis of stresses and strains for particular deformations, henceforth below is a method by which it is possible to relate the displacements of the nodes to the stresses and strains within an individual element. This is also necessary for the use of variational methods to be able to substitute such quantities into the Potential Energy Functional, explained later. The stress/strain constitutive equation for each node of a quadrilateral is,

$$\begin{Bmatrix} \sigma_x \\ \sigma_y \\ \tau_{xy} \end{Bmatrix} = [D] \begin{Bmatrix} \varepsilon_x \\ \varepsilon_y \\ \gamma_{xy} \end{Bmatrix} \tag{2.18}$$

Where for plane stress,

$$[D] = \frac{E}{1-\nu^2} \begin{bmatrix} 1 & \nu & 0 \\ \nu & 1 & 0 \\ 0 & 0 & \frac{1-\nu}{2} \end{bmatrix} \tag{2.19}$$

And for plane strain,

$$[D] = \frac{E}{(1+\nu)(1-2\nu)} \begin{bmatrix} 1-\nu & \nu & 0 \\ \nu & 1-\nu & 0 \\ 0 & 0 & \frac{1-2\nu}{2} \end{bmatrix} \tag{2.20}$$

The relationship between strain and the nodal displacements is,

$$\{\varepsilon\} = \begin{bmatrix} \frac{\partial u}{\partial x} \\ \frac{\partial v}{\partial y} \\ \frac{\partial u}{\partial y} + \frac{\partial v}{\partial x} \end{bmatrix} = [[B_1] \ [B_2] \ [B_3] \ [B_4]]\{q\} \tag{2.21}$$

Where the sub matrices $[B_i]$ are,

$$[B_i] = \begin{bmatrix} \frac{\partial N_i}{\partial x} & 0 \\ 0 & \frac{\partial N_i}{\partial y} \\ \frac{\partial N_i}{\partial y} & \frac{\partial N_i}{\partial x} \end{bmatrix} \tag{2.22}$$

Where E is Young's Modulus, ν is Poisson's Ratio (dimensionless), σ is stress (Pa), ε is strain (dimensionless) and q is the nodal displacement vector (m). But because the displacement model is in terms of the local coordinates, s and t, the derivatives need to be with respect to the local coordinates thus,

$$[B_i] = \begin{bmatrix} 1 & 0 & 0 & 0 \\ 0 & 0 & 0 & 1 \\ 0 & 1 & 1 & 0 \end{bmatrix} \begin{bmatrix} [J]^{-1} & [0] \\ [0] & [J]^{-1} \end{bmatrix} \begin{bmatrix} \{N_i'\} & \{0\} \\ \{0\} & \{N_i'\} \end{bmatrix} \tag{2.23}$$

Where $[J]$ is the 2x2 Jacobian Matrix and,

$$\{N_i'\}^T = \begin{bmatrix} \frac{\partial N_i}{\partial s} & \frac{\partial N_i}{\partial t} \end{bmatrix} = \frac{1}{4}[s_i(1+tt_i)\ t_i(1+ss_i)] \tag{2.24}$$

Summarising the equations above for relating stress, strain and displacement there exist three key formulae,

$$\{\sigma\} = [D]\{\varepsilon\} \quad (2.25) \qquad\qquad \{\varepsilon\} = [B]\{q\} \quad (2.26)$$

And from 2.25 and 2.26,

$$\{\sigma\} = [B][D]\{q\} \tag{2.27}$$

2.8.7 Variational Formulation of Element Stiffness and Loads

The FE method relates the nodal loads Q (N) to the nodal displacements q (m) via the following equation,

$$[Q] = [k]\{q\} \tag{2.28}$$

In the analysis of stress it is this relationship that is used when solving for the equilibrium situation, i.e. the minimum energy state of all the elements, the body of interest. Because the displacement models are separate for each element, the principle of minimum potential energy needs also to be applied separately to each element. The integral of the summation is equivalent to the summation of the separate integrals, so this poses no problem,

$$2U = \iint_A \{\varepsilon\}^T \{\sigma\} dA = \iint_A \sum_{e=1}^{N} \{\varepsilon_e\}^T \{\sigma_e\} dA = \sum_{e=1}^{N} \iint_{A_e} \{\varepsilon_e\}^T \{\sigma_e\} dA \tag{2.29}$$

At the end of the derivation the expressions for the element stiffness matrix and the element loads are reached,

$$[k] = h\int_{-1}^{1}\int_{-1}^{1} [D]^T [C][B] \det([J]) ds.dt \tag{2.30}$$

$$\{Q\} = h\int_{-1}^{1}\int_{-1}^{1} [N]^T \{\overline{X}\} \det([J]) ds.dt \tag{2.31}$$

The integrations seen in the above equations can be carried out numerically by Gaussian Integration because they are between -1 and +1. k and Q will be used in the next section during the assembly process.

2.8.8 ASSEMBLY

Prior to the current section consideration has only been given to a single element, now the consideration is extended to the entire problem by creating the assembly of individual elements. The process of assembly is illustrated with the most ease for a collection of one dimensional elements as seen in Figure 2.20.

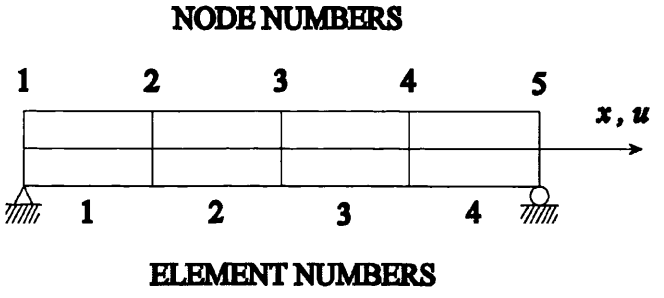

Figure 2.20: 1D element and nodal numbering convention.

The stiffness matrices are given as follows,

$$[k_1]=\begin{bmatrix} a_{11} & a_{21} \\ a_{12} & a_{22} \end{bmatrix} \qquad [k_2]=\begin{bmatrix} b_{11} & b_{21} \\ b_{12} & b_{22} \end{bmatrix}$$
$$[k_3]=\begin{bmatrix} c_{11} & c_{21} \\ c_{12} & c_{22} \end{bmatrix} \qquad [k_4]=\begin{bmatrix} d_{11} & d_{21} \\ d_{12} & d_{22} \end{bmatrix} \tag{2.32}$$

With the load vectors,

$$\{Q_1\}=\begin{Bmatrix} A_1 \\ A_2 \end{Bmatrix} \quad \{Q_2\}=\begin{Bmatrix} B_1 \\ B_2 \end{Bmatrix} \quad \{Q_3\}=\begin{Bmatrix} C_1 \\ C_2 \end{Bmatrix} \quad \{Q_4\}=\begin{Bmatrix} D_1 \\ D_2 \end{Bmatrix} \tag{2.33}$$

And the vectors of unknown nodal displacements,

$$\{q_1\}=\begin{Bmatrix}u_1\\u_2\end{Bmatrix} \quad \{q_2\}=\begin{Bmatrix}u_2\\u_3\end{Bmatrix} \quad \{q_3\}=\begin{Bmatrix}u_3\\u_4\end{Bmatrix} \quad \{q_4\}=\begin{Bmatrix}u_4\\u_5\end{Bmatrix} \tag{2.34}$$

The assembly of these four elements into a global matrix looks like this,

$$\begin{bmatrix} a_{11} & a_{12} & 0 & 0 & 0 \\ a_{21} & a_{22}+b_{11} & b_{12} & 0 & 0 \\ 0 & b_{21} & b_{22}+c_{11} & c_{12} & 0 \\ 0 & 0 & c21 & c_{22}+d_{11} & d_{12} \\ 0 & 0 & 0 & d_{21} & d_{22} \end{bmatrix} \begin{Bmatrix} u_1 \\ u_2 \\ u_3 \\ u_4 \\ u_5 \end{Bmatrix} = \begin{Bmatrix} A_1 \\ A_2+B_1 \\ C_1+B_2 \\ C_2+D_1 \\ D_2 \end{Bmatrix} \tag{2.35}$$

Or,

$$[K_m]\{U\}=\{F\} \tag{2.36}$$

This global matrix is solved to give the unknown nodal displacements. These displacements can then be used to give local stresses if needed. This concludes the explanation of the basics of the FE method for linear problems.

2.8.9 Conjugate Gradient Method

Traditionally the simultaneous equations held in matrices and vectors after assembly are then solved, for example by Gaussian back substitution. Such a method of finding the solution, or rather an approximation of the solution, is computationally intensive both on memory and processor time. To get around this problem an *element by element* approach to finding a solution where no assembly of the stiffness matrix takes place is much more favourable, Conjugate Gradient Method is such an approach. As a first step to finding the solution Equation 2.36 is manipulated,

$$\{F\}-[K_m]\{U\}_0=\{R\}_0 \tag{2.37}$$

Where R is a residual load vector in the following process that takes k steps to iteratively find the solution,

$$\{Q\}_k=[K_m]\{P\}_k \tag{2.38}$$

$$\alpha_k=\frac{\{R\}_k^T\{R\}_k}{\{P\}_k^T\{Q\}_k} \tag{2.39}$$

$$\{U\}_{k+1}=\{U\}_k+\alpha_k\{P\}_k \tag{2.40}$$

$$\{R\}_{k+1}=\{R\}_k-\alpha_k\{U\}_k \tag{2.41}$$

$$\beta_k=\frac{\{R\}_{k+1}^T\{R\}_{k+1}}{\{R\}_k^T\{R\}_k} \tag{2.42}$$

$$\{P\}_k=\{R\}_{k+1}+\beta_k\{R\}_k \tag{2.43}$$

For the very first iteration,

$$\{P\}_0=\{R\}_0 \tag{2.44}$$

The loop is terminated upon convergence i.e. the difference between $\{U\}_{k+1}$ and $\{U\}_k$ becomes the order of say 0.01%. The solution can be found after significantly less iterations by using a good first guess for the initial loads whereby $\{P\}_0=\{R\}_0$ is set to the leading diagonal term of the inverted stiffness matrix. This method is known as diagonal preconditioning [Shewchuk, 1994].

2.8.10 Material Non-linearity in Finite Element

The incorporation of plastic deformation involved in HSRW necessitates non-linear stress analysis. A non-linear analysis in the FE method requires a

considerable amount of extra equations to be solved entailing longer solution times. In many of the possible methods for plasticity analysis the load or displacements are applied iteratively, contrasting with linear stress analysis where the load or displacement is done in one loading and solution process.

The above derivation of the FE method is for elastic stress analysis, however the deformation that takes place during mash seam welding is not purely elastic. Elastic deformation takes place only during the first stage of deformation of a material, the deformation that takes place in the seam is of the order of 30% or more so a different approach is required. Material non-linearity refers to the behaviour of a material when Hooke's Law is no longer valid, the deformation is plastic and the relationship between stress and strain is more complex than a straight forward linear relationship.

2.8.11 Initial Stress Method

The Initial Stress Method or ISM [Zienkiewicz, 1969] is used in this work as it offers three superior qualities; fast solution times, the ability to apply a load or displacement effectively in large increments and a proven ability only to diverge if a breakdown in the structure occurs [Argyris, 1969]. As fewer solutions are required for the algorithm this allows the model to run on a conventional desktop PC. The method iteratively reduces the stress at each integration point and redistributes it as the corresponding nodal loads elastically, causing the material to *flow*.

The following derivation follows [Smith and Griffiths, 2004]. As was mentioned above, the loading or displacements are iteratively applied to the system in increments so for increment i,

$$[K_m]\{U\}^i = \{F\}^i \tag{2.45}$$

Where $[K_m]$ is the global stiffness matrix, $\{U\}^i$ is the global displacement increments and $\{F\}^i$ is the global external and internal body loads. The elemental displacements $\{u\}^i$ are extracted from $\{U\}^i$, and when multiplied by the B matrix reveal the elemental strain increments,

$$\{\Delta\varepsilon\}^i = [B]\{u\}^i \tag{2.46}$$

Both elastic $\{\Delta\varepsilon^{\mathrm{e}}\}^i$ and plastic $\{\Delta\varepsilon^{\mathrm{p}}\}^i$ strains will be taking place in the elements that are assumed to be yielding,

$$\{\Delta\varepsilon\}^i = \{\Delta\varepsilon^e\}^i + \{\Delta\varepsilon^p\}^i \tag{2.47}$$

Assuming perfect plasticity where only the elastic components are generating stresses results in,

$$\{\Delta\sigma\}^i = [D^e]\{\Delta\varepsilon^e\}^i \tag{2.48}$$

Where D^e is the elastic 'dee' matrix and σ is stress.

For each plastic iteration the stresses calculated from Equation 2.48 are added to the matrix of stresses from the previous plastic iteration and will be used to determine if the yield criterion is violated. During each plastic iteration where yield is violated, $\{F\}^i$ in Equation 2.45 needs to be divided into two types of load,

$$\{F\}^i = \{F_a\} + \{F_b\}^i \tag{2.49}$$

Where $\{F_a\}$ is the actual applied external load increment and $\{F_b\}^i$ is the body loads that are adjusted downwards for each plastic iteration. There are numerous other methods for calculating these body loads such as Viscoplasticity [Zienkiewicz ,1974], also known as the Initial Strain Method.

This initial stress method contains a greater relationship between increments of stress and strain than the initial strain method so,

$$\{\Delta\sigma\} = [D^{pl}]\{\Delta\varepsilon^e\} \tag{2.50}$$

Where,

$$[D^{pl}] = [D^e] - [D^p] \tag{2.51}$$

Where $[D^p]$ is the plastic property matrix. So called perfect plasticity is assumed so there is no strain hardening. It transpires that this assumption means once a stress state is reached whereby it is on the yield surface, any further change in stress state will be able to shift position *on* the failure surface, but never *outside* the failure surface thus,

$$\left\{\frac{\partial Y}{\partial\sigma}\right\}^T \{\Delta\sigma\} = 0 \tag{2.52}$$

Because plastic flow is associated, plastic strain increments occur normal to the yield surface, thus,

$$\{\Delta\varepsilon^p\} = \lambda\left\{\frac{\partial Y}{\partial\sigma}\right\} \tag{2.53}$$

Assuming the change in stress is generated only by elastic strain components gives,

$$\{\Delta\sigma\} = [D^e]\left(\{\Delta\varepsilon\} - \lambda\left\{\frac{\partial Y}{\partial\sigma}\right\}\right) \tag{2.54}$$

The final stage of the derivation requires that 2.54 is substituted into 2.52, and results in,

$$[D^p] = \frac{[D^e]\left\{\frac{\partial Y}{\partial\sigma}\right\}\left\{\frac{\partial Y}{\partial\sigma}\right\}^T[D^e]}{\left\{\frac{\partial Y}{\partial\sigma}\right\}^T[D^e]\left\{\frac{\partial Y}{\partial\sigma}\right\}} \tag{2.55}$$

For the ISM the body loads are reformed as opposed to summed for each plastic iteration until convergence takes place,

$$\{F_b\}^i = \sum_{elements}^{all}\iiint[B]^T[D^p]\{\Delta\varepsilon\}^i .dx.dy.dz \tag{2.56}$$

Computationally the ISM follows logical steps:-

1. fix displacements or loads applied to the system
2. solve global equilibrium equations using elastic properties
3. use Equation 2.55 above to give the stresses that need to be redistributed i.e. the plastic stresses
4. perform Gaussian integration using Equation 2.56 to generate to corresponding plastic bodyloads
5. go back to step 2 unless convergence has occurred when the redistributed plastic bodyloads are below a preset tolerance

2.9 Previous Models of High Speed Resistance Welding

The scarcity of literature on numerical or mathematical modelling of HSRW is even more profound than that of general experimental work, what now follows is a review of this limited literature.

The first instance of a HSRW simulation is a two dimensional mathematical model attempted by [Boyd, January 1981]. The model was more concerned with weld cooling rather than "heat generation and then cooling" and observed the process parameters effect on oxide layer formation and subsequent lacquering. The model was basic and made many simplifications but provided results consistent with experiments. The model was later elaborated to incorporate the geometry of a weld by using a graphics model of the transverse section of the weld and was validated against a similar lay up of plasticine being compressed between two flat surfaces. Despite these simplifications the heat loss mechanism was understood to have greater radiation and convection loss to the atmosphere than conduction into the can body and the graphics model correctly reproduced the experimentally observed topography of a HSRW. One of the conclusions was that relative contact area sizes play an important role in successful weld formation and it was stated that from the model results one would obtain better weldability by using electrodes with similar diameters.

Finite element models have been developed on commercial code packages by a few authors one being the work by [Brifcani, 1994] on Direct Current welding of can bodies to look at the voltage field and transient temperature fields. The finite element model using the commercial package ANSYS was not without its limitations, as admitted by [Brifcani, 1994], but did provide some useful information on the process. The interesting conclusion of the work was that a contributing factor towards the cause of defects was the instabilities resulting from high temperatures in the weld; these in turn caused current to be shunted

ahead of the weld gap. This was noted however not to be of such prevalence in HSRW where an Alternating Current is used.

[Ferrasse, 1998] conducted research with the aid of SYSWELD on Mash Seam Welding of 0.7 mm uncoated steel at 6 m min^{-1} and 9 m min^{-1}. MSW as modelled in Ferrasse's paper has stark differences when compared to HSRW and was discussed earlier in this thesis. The author still feels that it is sensible to consider a model of such a process as very little exists on HSRW itself. Three current settings were used for each of these weld speeds so that both melting and non melting situations could be observed. A two dimensional transverse non evolving mesh was used; this simplification was justified because the heat conduction was slow compared to the welding speed. A non evolving mesh based on micrographs was chosen because all the shape change took place "before the instance of melting". The transient thermal field was analysed by itself in this model so heat generation was simplified greatly by simply applying a heat source term in a linear fashion to a box shaped area in the cross section, see Figure 2.21.

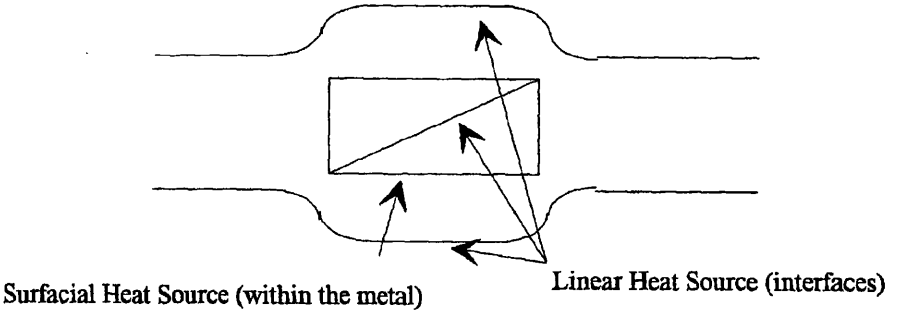

Figure 2.21: schematic showing the heat source used in the model by [Ferrasse, 1998].

The power input was measured as a function of time experimentally and applied to the model in timesteps to simulate the passage of the 2D section through the weld gap. Materials properties were considered a function of temperature and

validation was attempted by using infrared thermography and by polished and etched micrographs showing the heat affected zone and zone of re-solidification.

It was concluded that heat generation was sensible as some agreement was found between experimental and simulated results. One point made by [Ferrasse, 1998] was that the heat generation at the faying surfaces was of utmost importance thus implying that contact resistance is important. The model did however go through a change in behaviour when the current was increased to such a level that melting was expected and this was blamed for the model becoming unstable. Also increasing the welding speed changed the way heat was generated because of the shunting effect. Because of the model's reliance on experimental data to generate the power input, the model loses all predictive ability so such an approach is now dismissed for the remainder of this work.

[Murakawa, 2001] also followed the route of using a 2D longitudinal model to look at MSW, the welding of three uncoated steel plates 0.5 and 0.7 mm thick was considered in this model. Custom written software was used as opposed to the more widespread practice of using a commercial package. The speed of the process modelled was 1.4 to 1.6 m min^{-1}. Heat loss to the rolls, welding speed, welding current magnitude and current mode were all investigated with the aid of a thermo-electro-mechanical FE model.

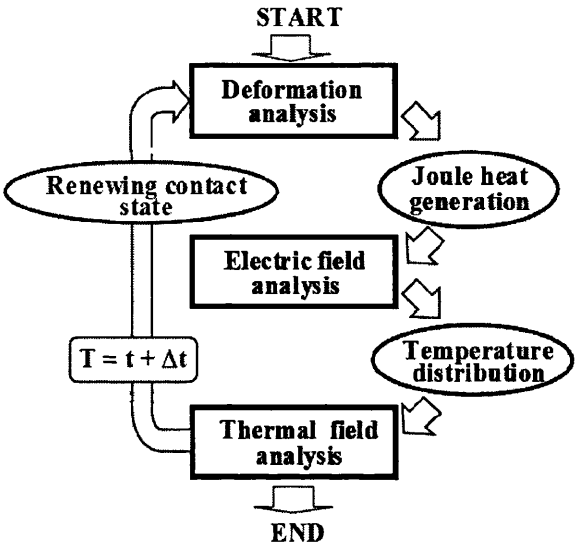

Figure 2.22: coupling of electro-thermo-mechanical analyses used in the model by [Murakawa, 2001].

The Figure 2.22 represents the procedure performed in the FE model. The approach is computationally more expensive than the approach of [Ferrasse, 1998] as more calculations need to be performed, but has greater fidelity to the physical process. [Murakawa, 2001] recognises that phenomena are taking place in three dimensions but states that a two dimensional model reported in this work is a first step. In the results of the model instabilities were witnessed, again with respect to the molten nugget growth. Investigation of this revealed a relationship between the contact length and the stability of the nugget; the one cycle on / one cycle off nature of the modified welding current allowed the high temperature of the nugget to be pumped out into the electrode and the contact length to increase before the next on cycle was applied. Some modification was needed to take further heat out of the weld; it was stated that heat would dissipate in the direction transverse to the welding direction in reality, but it would be *trapped* in a 2D simulation.

An instance of HSRW simulation being conducted within Corus is that of [Beaverstock, 2000], later followed up by [Wen, 2001]; this work details the use

of a commercially available FE package ABAQUS. Numerical solution to the heat distribution has been calculated in two dimensions, both transversely and longitudinally. The 2D results are shown in Figure 2.23 and 24 below.

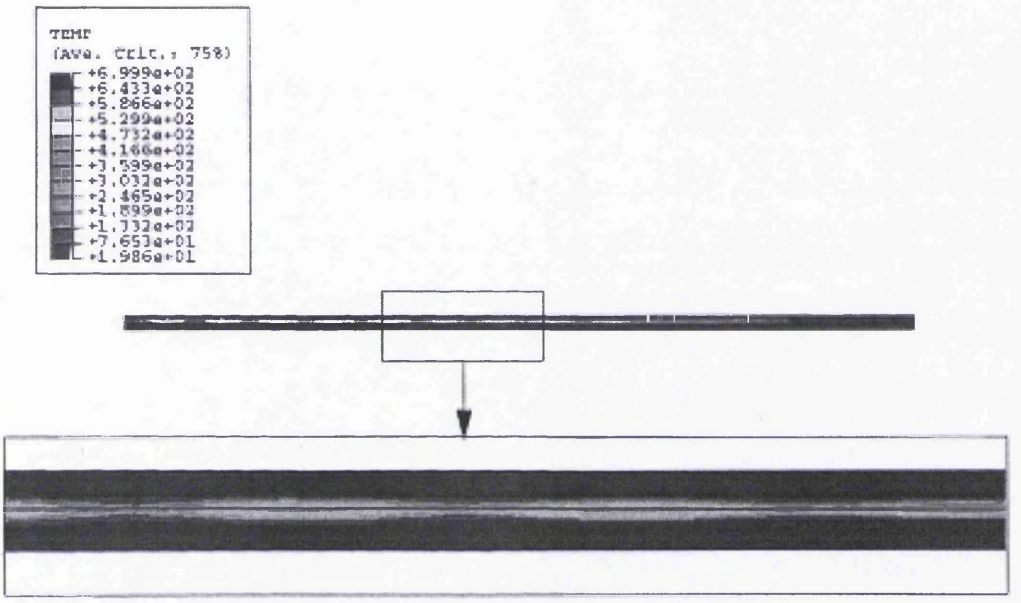

Figure 2.23: longitudinal simulation fringe plot of temperature [Beaverstock, 2000].

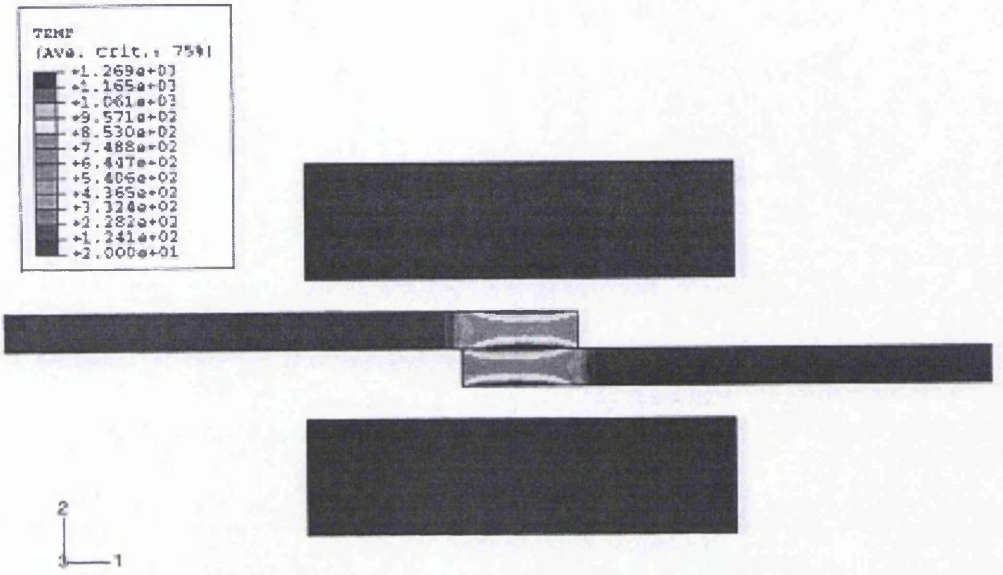

Figure 2.24: transverse simulation fringe plot of temperature [Beaverstock, 2000].

The main aim of this work is a preliminary investigation into the usefulness of the Finite Element technique by exploring the possibilities and appreciating the potential difficulties one can encounter when simulating can body welding. A variety of assumptions and simplifications are used in this work, one of which is the use of a fixed roll gap. This is an over simplification because potentially so much is decided by the movement of the upper electrode, viz current density because of its dramatic sensitivity to geometry. The two simulations are only in two dimensions; a gross oversimplification because the physical phenomena taking place are three dimensional, particularly heat conduction and electrical potential fields. Coupled electro-thermo-mechanical analysis is not performed in either of the simulations; the transverse section is just a thermo-mechanical analysis and the longitudinal simulation was just a thermal analysis to look at Joule heating. The longitudinal simulation however did not model the Joule effect, but simply used heat fluxes for the surfaces in contact and the bulk heat generation. For the thermal calculations of the model no heat loss to the electrodes or atmosphere was assumed, clearly far from reality considering the

work of [Boyd, January 1981] where this is the main method of heat loss! Also contact resistance was neglected, a known important phenomenon where bodies are in contact and electro-thermal effects are of interest. The body of work concluded that the ideal situation would be to develop a fully coupled electro-thermo-mechanical model, however there was some concern that this might be too computationally expensive to run and prone to convergence problems. It was this work that preceded the work of [Brown, 2004, 2005] and of [Suthar, 2005] and resulted in the genesis of their research.

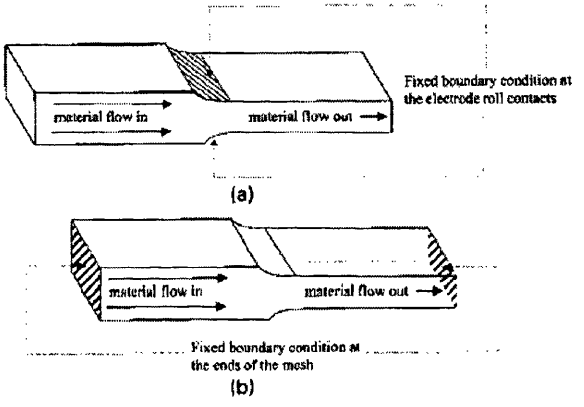

Figure 2.25: schematic model description [Brown, 2004].

[Brown, 2004] followed an Eulerian approach when modelling the HSRW process whereby a static mesh has material flowing through it, see Figure 2.25. The three dimensional mesh used in the model is pre-deformed but the electro-thermal effects are calculated. The model was used to numerically experiment with the process variables, something not possible in reality, so as to determine the most important process variables. Figure 2.26 shows how the model reaches equilibrium and from then on behaves in a cyclic fashion.

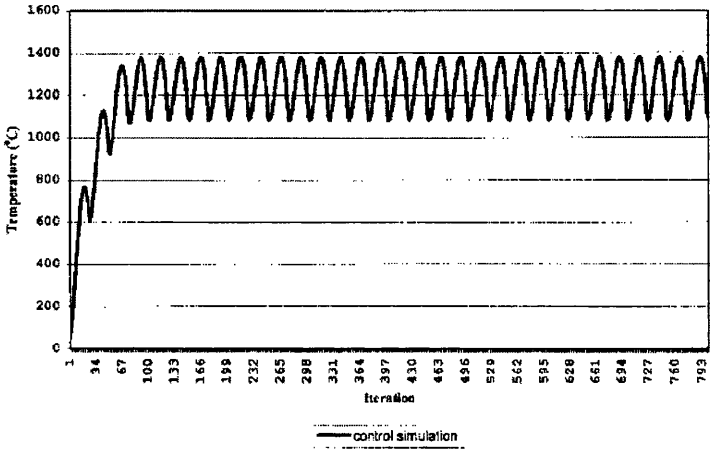

Figure 2.26: transient temperature graph [Brown, 2004].

When the welding velocity was changed and its effect monitored, the precise change in heat input was known and not only that but the position geometrically that is subjected to the variation in heating. The same procedure was performed when changing the thickness of the tinplate being welded amongst other process parameters in this work. The usefulness of simulation was expounded when the higher heating seen at sharp corners was attributed to high current density.

2.10 WELD MONITORS

The ability of a model to *look inside* the weld zone is unrivalled however other methods have been devised for looking at certain process variables. One such method is infrared monitoring. Infra red monitoring is an indirect method of weld temperature measurement relying on the fact that the temperature of the weld in general is linked to the temperature of the surface shortly after leaving the weld gap. [Snee, 1972] applies this fact to seam welding and attains interesting results. An analogue readout from the infra-red detector has the ability to have a higher amplitude for a satisfactory weld than a cold weld, and a higher readout for splash being formed than for a satisfactory weld so can be used as an early

warning system to let operators know that weld conditions have changed since initial set up. But this method does not have that same power as a FE model to look at heat generation patterns or defects.

Another method that offers more scientific insight to weld formation during resistance welding processes and can also, like infra-red monitoring, be used as an in-process evaluator is dynamic contact resistance monitoring. Dynamic contact resistance monitoring is applied by [Savage, 1978] and applies the principle to spot welding. Previous work by [Savage, 1977] on the static contact resistance, i.e. the initial value of contact resistance before a weld has been formed and the final value of contact resistance after a weld has been formed, showed no relationship to, or indicator of, weld quality. Work on dynamic contact resistance gave some indication of what was happening to the faying interfaces. Contact resistance was calculated by taking away the bulk resistance of the steel from the total resistance of the work piece. Depending on the magnitude of the welding current there was a variation in contact resistance that can be related to weld formation. As the current begins to flow through the sheets being spot welded, there is a drop in the contact resistance, related to the heating up of the zinc on the surface of the steel softening and then wetting the surfaces to get greater contact. Then as the current continues to flow the heat builds up and the contact resistance builds up again as one would expect with resistivity before reducing again as the heat causes the surfaces to join before disappearing when substrate melting takes place. If the welding current is increased the first drop in contact resistance doesn't take place because it happens so rapidly, it just increases with resistivity and then decreases when the weld has formed.

[Basarab-Horwath, 1986] applies a similar principle to calculation of dynamic contact resistance during can welding and concluded that there may be a possibility that this could be built into a seam weld monitor. [Basarab-Horwath, 1988] found out experimentally that voltage, current or resistance although showing some variation did not provide sensitive enough information for a weld

quality monitor and this is backed up by separate research from [Needham, 1983]. The measurement of these variables did however prove fruitful as the power put into a weld nugget was a good indicator of quality. Physically it makes sense too because it is the power dissipated that is causing the formation of the weld.

Another method of monitoring welding processes that could even potentially be used for validation is high speed photography. [Sun, 2001] used previous research by [Cunningham, 1965] for validation of an FE model of Projection welding, here high speed photography proved useful in monitoring the deformation stages during the welding process, allowing comparison to the model. High speed photography could potentially offer some information on the deformation sequence during HSRW but this depends on good positioning being available for the camera. There is little or no chance of positioning the camera within the lower electrode as this sits within the can body being welded, however for the upper electrode there would be a greater possibility. Even supposing the pictures could be attained there is still no chance to observe any internal heat generation patterns and how they develop over time. It could be argued that it is sufficient to know the final shape of the weld and the deformation sequence is less important, but it is still impossible to *see* the internal deformation.

2.11 Conclusion of Literature Review

Through this review of literature the reader has been made aware of pertinent research related to the title of this body of work. The review started with processes related to HSRW such as mash seam welding providing some insight into how this family of welds work and highlighting differences and similarities. Due to the scarcity of literature specifically on HSRW this expands the available opinions on various phenomena of interest, for instance weld formation mechanisms. Following this the basics of HSRW itself were introduced as well as

the process variables and how each of these affects the process. These important process variables are needed in the current model if it is to be valid. Furthermore these process variable descriptions allow the reader to envisage the process better so that when the model is drawn up the necessity of each model ingredient is better understood, and likewise when assumptions have to be made and details omitted. The bonding method was discussed as this is of prime importance with respect to the model, for the model is aimed at simulating the behaviour of the weld when it is producing sound welds in the steady state. Consequently, end effects are not a topic of study and are not simulated here.

This first half of the literature review described the physics of the process and after this the focus deviated toward more of the relevant modelling literature. The governing equations for the electro-thermal analysis were first highlighted as this is an important part of such a simulation. Then the FE method was introduced, in particular the stress analysis; the work of [Suthar, 2005] and of [Brown, 2004, 2005] gives a full treatment of the electro-thermal effects. The governing equations of the initial stress method and their derivation were discussed as well as a guide to implementation of the method being given. The reader, having been introduced to the fundamentals of the FE method, was then taken through previous models of the process and areas for expansion and elaboration were given some attention. The final topics of the literature survey were dedicated to the alternative and more traditional experimental techniques that have been used to study seam welding, and their benefits and disadvantages discussed with respect to a model of the process.

By this stage the author has hopefully provided sufficient foundation to now go on to describe the development of the current model. The reader has also been made aware of the importance of this novel approach to gaining insight into HSRW. The decision to construct a fully coupled electro-thermo-mechanical analysis in three dimensions is justified as novel due to the fact that it has remained unreported in the literature, as this extensive survey has shown. Given

that HSRW is a three dimensional process the information that can be gleaned from such a model should be superior to previous attempts.

3.0 Model Formulation

At this stage the reader should now be aware of the background to the problem. Before the results are presented the ensuing section aims to bring to light the methods by which the model was devised, and the assumptions made of the physics involved. A Finite Element model has been created to model the necessary phenomena in the process and briefly comprises three parts *coupled* together; the elasto-plastic stress analysis, the electrical field and the thermal field. Each step is inextricably linked and highly non-linear.

Coupled finite element models are prevalent in many different sectors of science and engineering and are used to bridge two or more separate, but dependent, physical phenomenon. In HSRW the bridging is between three physical phenomena on the same length scale, but the bridging can also be on different length scales where the modelling techniques do not exist that can cope with for instance stress analysis and lattice defects simultaneously [Raabe, 1998]. Sequential coupling is where adequate parameter transfer takes place among simulations that are used sequentially.

The coupling is obligatory since in each timestep the stress analysis will change the shape of the work piece as this will affect voltage distribution and therefore current density and in turn will influence the temperature field. Temperature-dependent properties calculated using this new temperature field are used for each subsequent timestep. Thermo-mechanical coupling is used in models of HSRW [Wen, 2001], Continuous Casting [C. Li, 2004], Superplastic Forming [Adam, 2003] and in Layered Manufacturing of metallic parts for rapid prototyping [Mughal, 2006]. Electro-thermo-mechanical coupling is exemplified frequently in models of Spot Welding [Hou, 2007], a process comparable to HSRW but not without stark differences. Electro-thermo-mechanical coupling is also used in research on Hall-Héroult cells [Richard, 2001] and Projection Welding [Sun, 2001].

Further details, the techniques and the assumptions of the model are now described so the reader can appreciate the extent of the detail of the model and equally what areas of physics that have been left out, and for what reason. In the development stage of any model assumptions and simplifications have to be made as not every physical phenomenon can be taken into account. For a component of interest to an engineer to be simulated in useful timescales requires many phenomena seen as insignificant to be omitted. Other FE models are referenced and where applicable other references are used to justify decisions made by the author in this body of work.

3.1 MESHING

Finite Element is a piecewise approximation method where differential equations describe behaviour over small simple sections of a complicated body. For a numerical model to be applied to the HSRW Process the problem has to be discretised in space, resulting in a mesh as shown below.

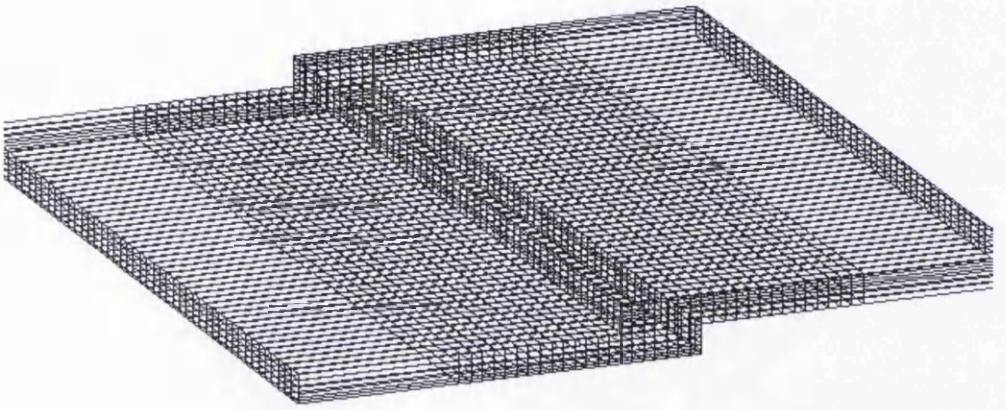

Figure 3.1: 3D Lagrangian mesh.

A three dimensional Lagrangian mesh is used in this model to represent the tinplate strip that will be welded. The two blanks of tinplate or rather the two ends of one blank are modelled as one mesh and the elements used are linear 8 node hexahedral bricks for both the stress and electro-thermal analyses. Shown in Figure 3.2 is a two dimensional *slice* of the mesh, the mesh is built of numerous identical slices.

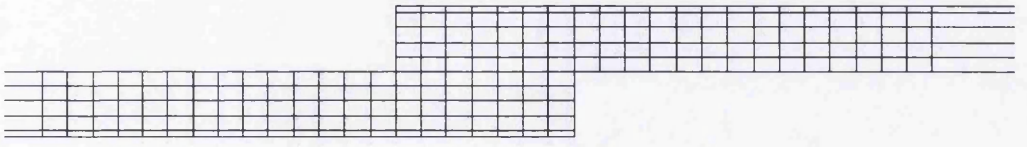

Figure 3.2: cross section of 3D Lagrangian mesh.

The electrode rolls are not represented as a mesh as they are not of interest in the same way as the tinplate and instead they are represented geometrically in the contact algorithm. HSRW is a dynamic process and hence the mesh needs to

move so the mesh needs to be long enough to allow ample distance for the model to reach steady state. Ideally one would require a very long mesh, but as a mesh gets longer the greater the number of equations is needed and the larger the storage requirement of the problem, eventually a point even could be reached where memory *paging* becomes necessary.

To avoid this problem and to use low floating point counts one can employ a technique such as automatic mesh regeneration as is done in this body of work. A straightforward computational procedure is followed in this numerical model; the mesh is moved through the weld gap between the electrodes as one would expect but a short mesh is used and is instead regenerated and is therefore effectively of infinite length. Simplistically this process is represented below in Figure 3.3 for an 8 node 2 dimensional mesh.

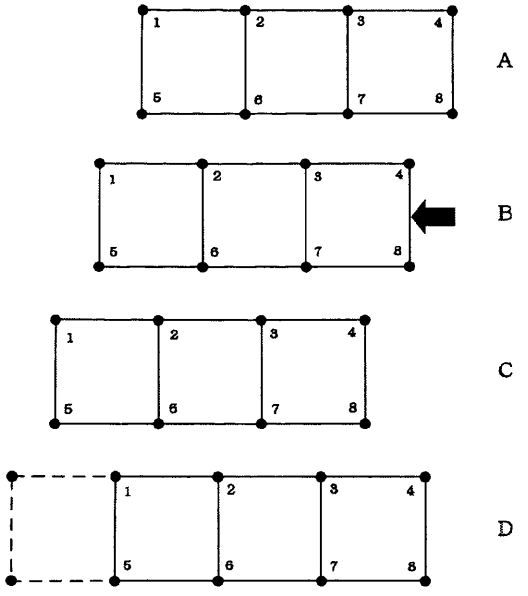

Figure 3.3: schematic representation of the automatic mesh regeneration algorithm.

The mesh is moved each timestep as is shown in step B, but when it moves past a critical distance as in D the mesh is regenerated so that it will never move more

than the critical distance even though long welds have been simulated. This prevents the mesh from drifting off too far and allows a mesh of minimum length to be used.

3.2 CONTACT ALGORITHM

HSRW like other mechanical processes involves contact between multiple objects, necessitating a contact algorithm to enforce interpenetrability of said multiple objects. Contact is numerically challenging and can be modelled by numerous methods, and is even the subject of theses [Kloosterman, 2002]. Kloosterman describes various methods of contact but the penalty/stiff spring method [Adam, 2003] has been implemented in this model of HSRW because of its simplicity and fast solution times when compared to an evolutionary shape optimisation method [W. Li, 2005] because multiple plastic solutions are avoided.

Contact is greatly simplified in this HSRW model because the electrodes are not modelled *per se*, only their presence. The electrodes are geometrically represented not by a mesh but as short cylinders that can be represented simply as Cartesian coordinates of a centre, height and radius. The cylinder is then a volume from which every node in the mesh is excluded. The penalty method is then used to fix the offending node's positions from the volume of the electrodes to the edge by using simple geometry. This *geometric* contact algorithm is highly efficient in terms of storage and solution times and is pictorially represented in Figure 3.4. The welding load is then a sum of all offending node's reactionary body loads.

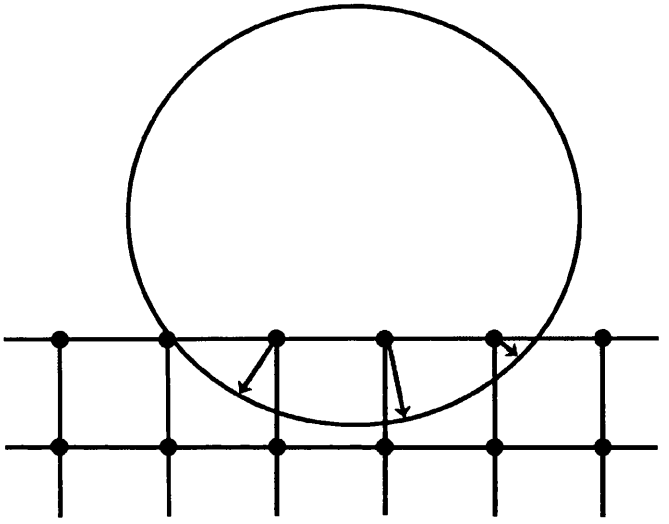

Figure 3.4: contact algorithm working on an undeformed mesh, offending nodes are identified and a displacement is prescribed to these offending nodes.

3.3 Stress Analysis

Finite Element analysis is a widely used method for performing stress analysis, spanning virtually every discipline of engineering and science. The vast majority of current research is carried out on commercial software packages such as SYSWELD, ANSYS and ABAQUS and frequently takes advantages of their multi-physics capabilities. A few selected papers from the literature where models were constructed in such a fashion include models of:

- Laser Butt Welding in SYSWELD [Tsirkas, 2003]
- Projection Welding in ABAQUS [Sun, 2001]
- Submerged Arc Welding in ABAQUS [Wen S.W., 2002]
- Spot Welding in ANSYS [Hou, 2007]
- Hall-Héroult Cell Anode in ANSYS [Richard, 2003]

As discussed earlier in the literature review previous attempts have been made to model HSRW, but in each case there were gross simplifications and significant detail was omitted. The papers listed above were all formulated on commercial packages. By their very nature these packages operate as *black boxes* to provide a solution and as such do not provide enough detail on precisely how the model was formulated. The papers are all useful though, as they provide an insight into the capability of FE as a method and highlight the possibilities in terms of outputs and the physics from which the resultant models are constituted. Boundary conditions are also discussed in publications.

It is frequently the case that the method of stress analysis is omitted in papers where the model was performed using commercial packages i.e. is the method Initial Strain or Initial Stress based? Other details are also omitted such as the equation solution algorithm used and tolerances. The model in this body of work has been developed by starting with open source FORTRAN95 implicit Finite Element code [Smith, 2004] and then making it significantly more elaborate, combining codes and refining the model and assumptions as part of a validation process. Using this route allowed precise control of the model and importantly an understanding of its inherent weaknesses.

The method of stress analysis for this research is based on the Initial Stress Method (Modified Newton-Raphson Method) and the elasto-plastic rate equations are integrated using a Consistent Return (Backward Eulerian) Algorithm [Smith, 2005]. The algorithm actually has the ability to deal with non-associated plastic flow of the body of interest, but in metallic polycrystalline aggregates the deformation is frequently reported as associated [Chakrabarty, 1987]. The von Mises yield criterion is employed within this algorithm to decide the stress condition at which yielding takes place, generally accepted as being suitable for a metal because yield strength is putatively independent of hydrostatic stress. There is some recent work in the literature by [Wilson, 2002] that puts forward evidence that this assumption is not true; after experimental

results are compared with numerical results generated by ABAQUS [Wilson, 2002] concludes that the Drucker-Prager yield function serves a better method of predicting yield in aluminium notched round tensile samples. Precise yield behaviour of metallic materials is not of concern here so the widely used von Mises criterion is utilised.

3.4 Load Guess

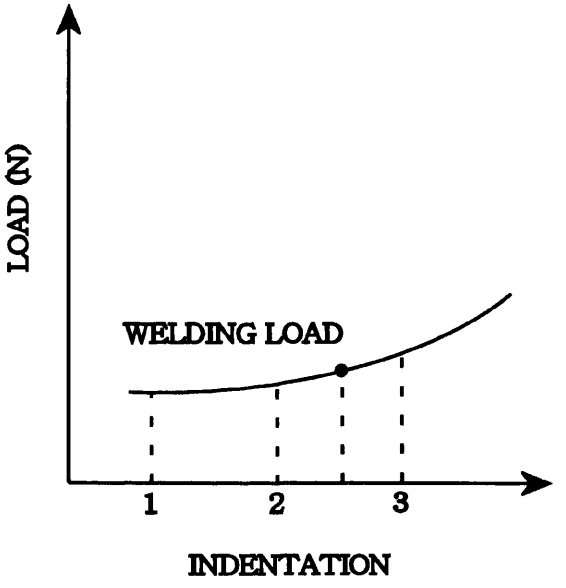

Figure 3.5: pictorial description of how the model applies the correct welding load from applied displacements.

In FE the interactions between the body of interest and workpieces, tools etc can be represented as either a fixed load or a fixed displacement to relevant nodes. The minimum potential energy of the system is then sought to find the solution. This causes some difficulty in a model of HSRW because a shape (the electrode) is displaced into the workpiece under a constant load. Obviously the correct circular indentation is required so the geometry is representative of the process but so is the correct level of indentation required so the reactionary force is equal

to the weld load. The way round this is to perform three load guess steps each of increasing severity by fixing displacements so the shape is always correct. A polynomial curve is fitted through the reaction loads obtained using the least squares technique, see Figure 3.5. The polynomial equation obtained will then allow accurate interpolation of the indentation level required to match the welding load on the fourth indentation. Inaccuracies using this method are typically less than ±5% of the welding load.

3.5 Mechanical Properties

As discussed in the literature review, deformation of metals and alloys occurs by the movement of dislocations along slip planes. A material's yield behaviour is therefore a function of dislocation mobility so if one can help or hinder this there will be a corresponding drop or increase in yield strength, respectively. Assuming comparison is between identical alloys that have been processed by identical processes an increase in temperature will increase dislocation mobility and therefore decrease yield strength. Increasing the temperature will also decrease the effect of dislocation pinning sites and will allow for dynamic recovery and recrystallisation further helping the softening of the metal/alloy. The thermally activated processes of recovery and recrystallisation are also dependent on time so this also takes place to a lesser or greater extent depending on the welding speed.

For FE simulations of production processes the mechanical properties and how they vary with process conditions are often critical to the success of the model. Flow behaviour and how this will be used in relation to a finite element model is discussed by many authors but some notable work has been performed by [Tafzi, 2000], [Krallics, 2000], [Chen, 2008], [Deng, 2008] and [Rusinek, 2007].

[Tafzi, 2000] and [Krallics, 2000] both performed compression tests at a variety of temperatures and strain rates to generate data for determination of material parameters used in the classical flow equation used for hot working and creep conditions:

$$\sigma_{ss} = \frac{1}{\eta}\sinh^{-1}\left(\frac{Z}{\theta}\right)^{m} \tag{3.1}$$

With

$$Z = \varepsilon.\exp\left(\frac{Q_a}{RT}\right) \tag{3.2}$$

Where η, θ, m are material parameters, Q_a is the activation energy for hot working, R is the universal gas constant and ε is strain. Z is the Zener-Hollomon parameter. Both papers conclude that these equations, when used to predict yield behaviour show good agreement with experiments. The disadvantage with this technique is that a dedicated test program is required to produce values for these material parameters before the equations are of any use at all. [Chen, 2008] similarly uses experimental data but this time expresses yield behaviour as a function of temperature, only under monotonic conditions, see Figure 3.6 a). The data is usefully plotted as a strength reduction factor and an equation is proposed to be used in the simulations. Good agreement is found between theoretical and experimental yield curves, Figure 3.6 b).

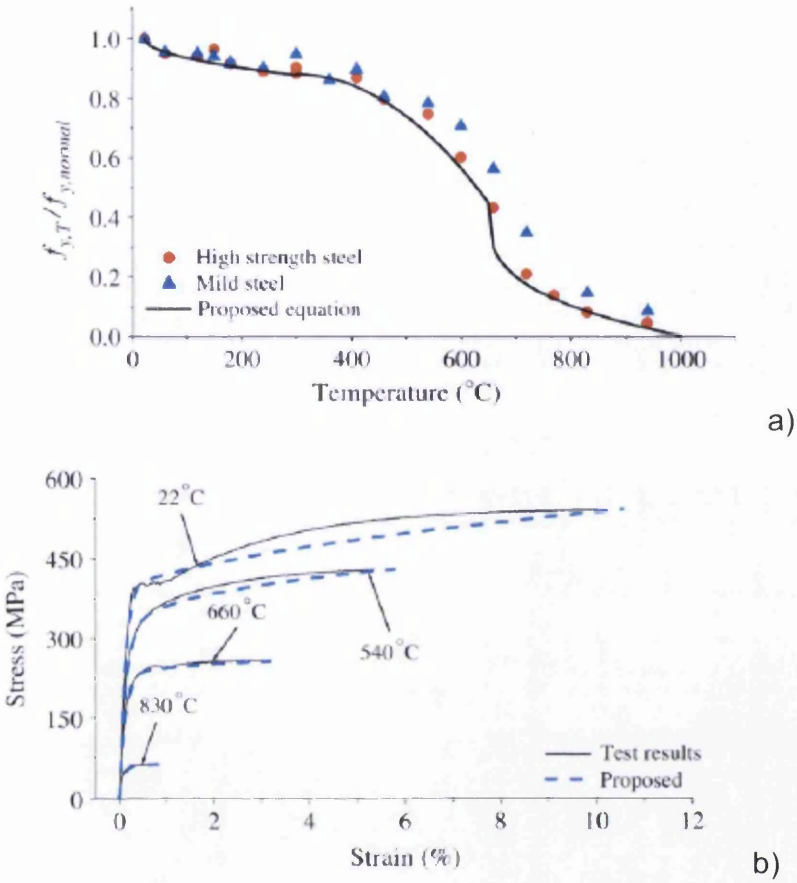

Figure 3.6: reduction factor, points in a) are of 0.2% yield strength, flow stress at temperature / nominal flow stress, b) is proposed yield function and test results [Chen, 2008].

[Deng, 2008] uses a similar approach to [Chen, 2008] but doesn't use experimental data to produce curves for the mechanical property reduction factor, the data is not referenced. Again [Deng, 2008] comes to the conclusion that the mechanical properties chosen were adequate when simulation results correlate well with experimental ones. See below Figure 3.7 for mechanical property variation with temperature.

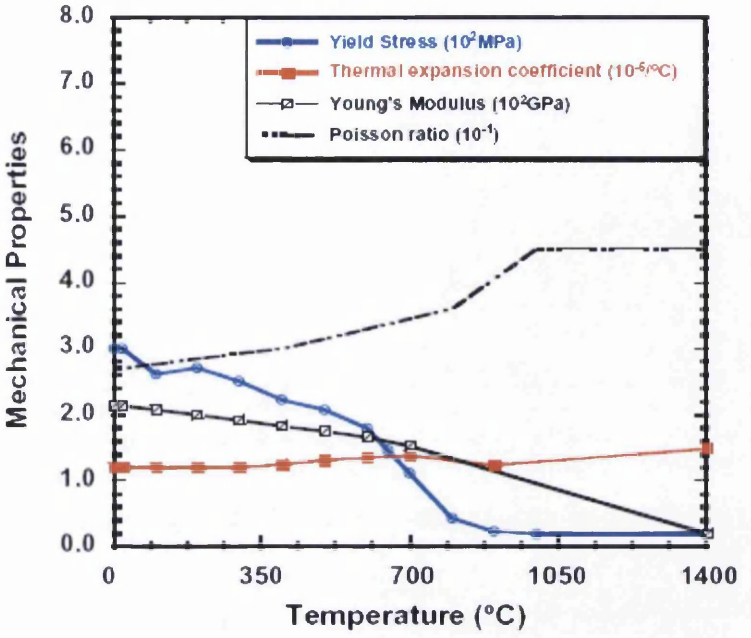

Figure 3.7: mechanical properties used by [Deng, 2008].

Both [Deng, 2008] and [Chen, 2008] use mechanical property reduction factors similar to those published in the British Standard (BS EN 1993-1-1:2005 Eurocode 3: Design of steel structures) for design of buildings to be fire resistant, Figure 3.8. The mechanical property reduction plots are also similarly designed for use in monotonic loading conditions, strain rates calculated in HSRW are the order of 10 s^{-1} to 100 s^{-1}.

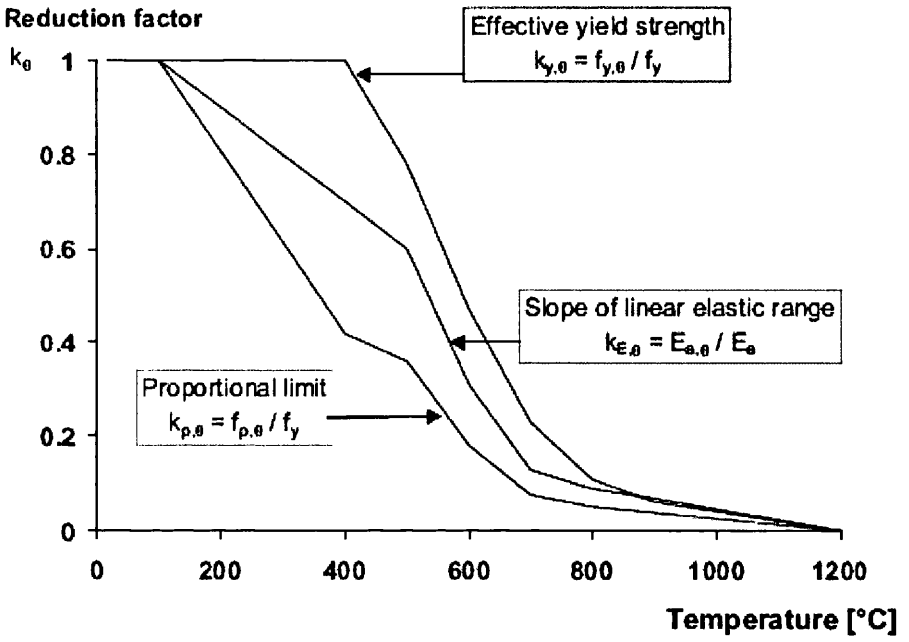

Figure 3.8: suggested mechanical property reduction factors set out in the British Standard used for fire resistant steel framed buildings [BS EN 1993-1-1:2005 Eurocode 3: Design of steel structures].

The work of [Rusinek, 2007] looks to calculate material parameters to predict yield behaviour over a "wide variation of temperatures and strain rates" for mild steel but the temperatures are not in the hot working range. The authors work on a new constitutive relationship, the RK relation. The relation appears to work well over the conditions used for validation but 8 material constants are needed so the only way to use this material model is once again a dedicated test program.

In light of all this previous work on developing material models needing costly test programs the decision has been taken to go for a reduction factor method like numerous other authors have done, but to opt for a simple linear relationship. The use of more complicated curves was considered, such as the more sinusoidal types identified in the literature to describe the reduction factor. However, tests using the model showed very little difference in the final results and non-linear relationships caused the model to be less stable. This decision is also justified because without a test program the material behaviour would be

hard to determine at the process conditions; viz high strain rates and very high heating rates. Without a continuous heating diagram the phases present are not precisely known, and the published curves discussed above are for monotonic conditions so softening due to recovery and recrystallisation can take place unlike the conditions prevalent during HSRW.

Finally, the last important topic when discussing mechanical material parameters is their sensitivity to strain rate. Under monotonic conditions and for times less than that where creep takes place the effect is negligible [Tafzi, 2000]. [Rusinek, 2007] takes mechanical test data from several authors and combines it with data in the authors own work, all on mild steel. In the strain rate ranges the curve is approximated by three linear curves, as depicted in Figure 3.9 below. Using the equation of the best fit line for the strain rate ranges seen in the validation tests for this body of work the strength is effectively increased by ~5%. Though not sounding significant on its own the effect is more dramatic in the simulations.

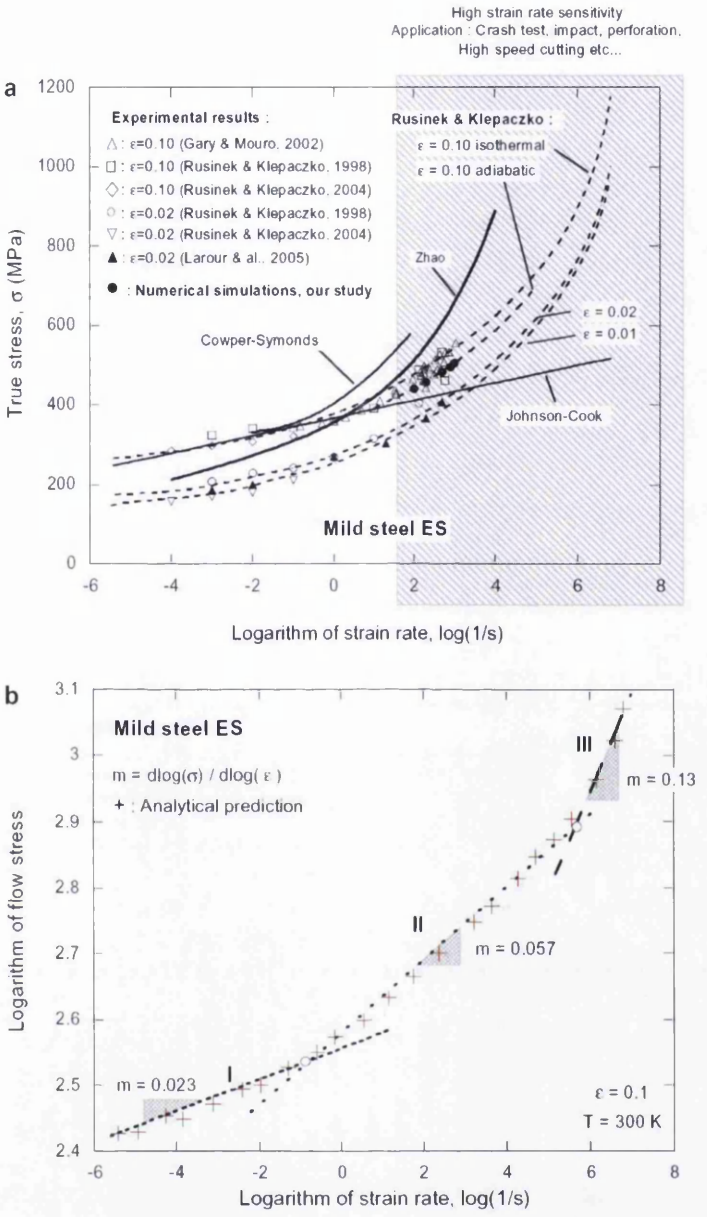

Figure 3.9: strain rate dependency of steel flow stress [Rusinek, 2007].

3.6 Electric and Thermal Fields

As one can see in Figure 3.10, there are several physical phenomena operating when one considers the electro-thermal effects present in the HSRW process.

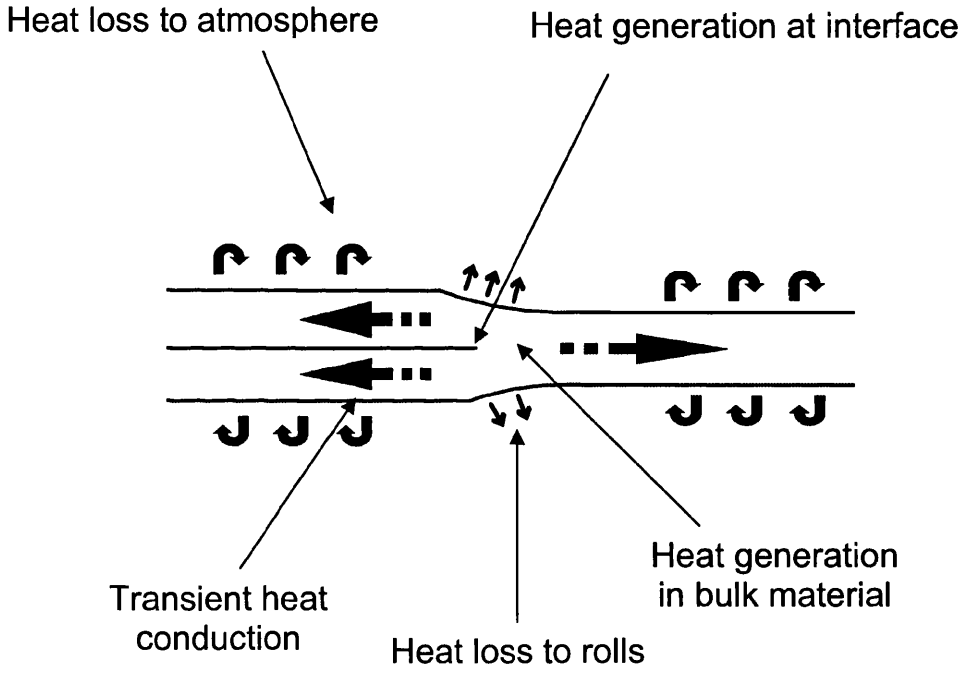

Figure 3.10: schematic of relevant physics in High Speed Resistance Welding simulated in the model, the rolls are omitted for clarity.

Electro-thermal effects are handled in code derived from that developed by [Brown, 2004, 2005] and by [Suthar, 2005], modified to fit in with the stress analysis mentioned previously. The code also uses the principle of Finite Element discretisation to find numerical solutions for the voltage and transient thermal fields. FE is used in several other similar applications [Sun, 2001][Hou, 2007][Richard, 2001] and has produced useful insight into the physics taking place. Transient heat conduction can be simulated by other methods reported in the literature; Finite Volume (FV) [Pavlik, 1995][Gutierez-Miravete, 1995][Taylor, 2000] is used extensively. FV is rarely used for stress analysis and as FE is used

in this body of work for stress analysis it does not seem sensible to both rewrite the electro-thermal part of the model and then face difficulty in integrating it to work in a coupled fashion with the deformation routine. FE also has great advantages in representing geometry very well, particularly smooth curves that are formed by the rolls. Heating by the Joule effect and transient heat distribution is modelled using FE in Submerged Arc Welding [Wen S.W, 2001] and similarly modelled by [Hou, 2007], where the heat field of a spot weld was outputted and visualised below.

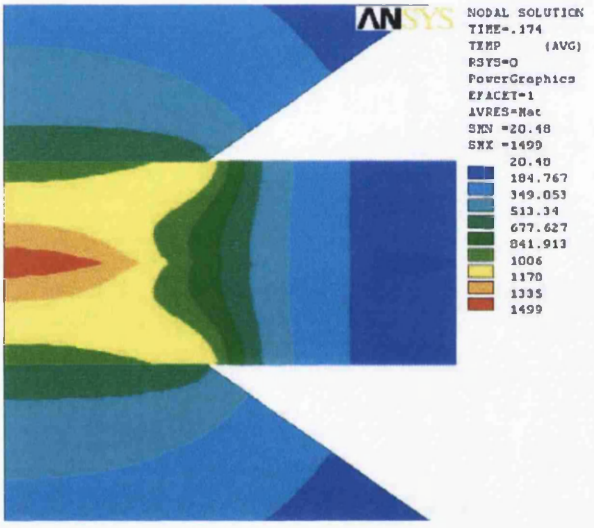

Figure 3.11: typical fringe plot of transient temperature field from resistance spot welding using ANSYS [Hou, 2007].

3.7 Contact Resistance

Electrical and thermal contact resistance are very important as far as heat generation and dissipation is concerned when two or more bodies are in contact and heat conduction and electric field are of interest. Hall-Héroult cells [Richard, 2003], Electric Arc Remelting and Electric Arc Steel Production are a few examples where, like HSRW, Joule Heating is of interest at two adjoining bodies. HSRW is different to these processes where heat conduction and therefore

thermal contact resistance between the two sheets is not as important as electrical contact resistance. Thermal contact resistance is viewed as unimportant because the magnitude of heat diffusion is so much less than welding speed i.e. the contact resistance will have disappeared for much of the time that heat diffusion is taking place because the weld will have formed. Thermal contact resistance is described as important by [Mughal, 2006] where it is included in the model of layered manufacturing of rapid prototypes; a value is taken away from the heat transfer coefficient thus effectively slowing the rate of heat loss to the base plate onto which material is deposited in the molten state in order to build up a three dimensional component in layers. The importance of the change in electrical and thermal contact resistance at the surface of the bodies to be joined is discussed by [Thieblemont, 1995].

Thermal contact resistance is relatively unimportant because of the symmetry of the weld stack up but the same cannot be said of electrical contact resistance. Electrical contact resistance is responsible for the greater intensity of heating at the overlapped tinplate, evidence of which can be seen in weld microstructures. Characterisation of such phenomena needs to take place before an accurate model can be drawn up. The work of [Richard, 2003] sought to investigate several interface resistance theories such as that proposed by [Cooper, 1969] originally devised for thermal contact resistance, to which essentially the same concepts apply. The theory is based on the assumption that a surface is not atomically smooth, as shown in Figure 3.12 below.

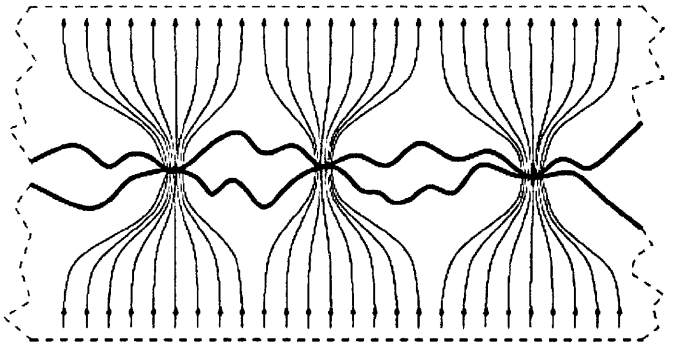

Figure 3.12: Asperities and the contact situation of two solid bodies [Richard, 2003].

The surface is represented by two waves, a carrier wave to represent the *waviness* and a higher frequency noise wave to represent the *asperities.* This original model has been modified and applied for both electrical and thermal contact resistance since its inception, for example by [Yovanovitch, 1996] to cover plastic behaviour of the surface. Mathematically this is shown in a simplified equation by [Singer, 1991]:

$$R_c = 0.8\beta_e \frac{\phi}{\psi}\left(\frac{P}{H_c}\right)^{-0.95} \tag{3.3}$$

Where ϕ is the root mean squared surface asperities height of the equivalent surface, ψ is the harmonic mean slope of this same surface, β_e is the harmonic mean electrical resistivity of the contacting materials, P is the contact pressure and H_c is the microhardness of the softest surface. As one can see there is a complicated relationship, and a lot of material parameters that are unknown. [Richard, 2003] tried to fit this contact model and another *fractal* model to the problem in hand, the Hall-Héroult Process. The complexity of both contact theories proved too difficult to implement and they were abandoned in favour of a reverse engineered empirical equation. This equation fitted the data with good agreement.

Electrical contact it seems, exhibits complex behaviour. To quantify this complex behaviour several value/parameter measurements are needed that could only be determined by a costly experimental campaign using, for example, the apparatus depicted in Figure 3.13. [Richard, 2003] made such an equation fit data but the experiment was on a larger scale and appreciably simpler.

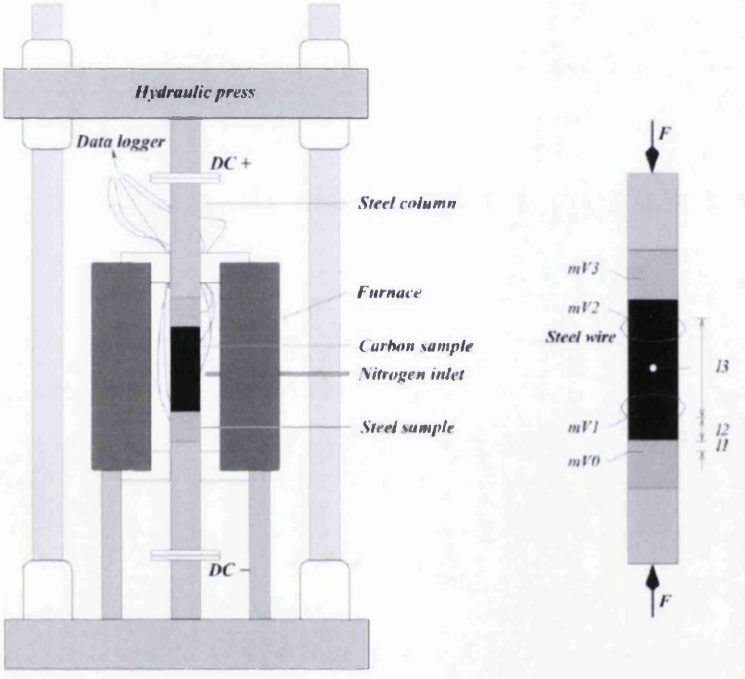

Figure 3.13: equipment used for contact resistance measurements [Richard, 2003].

The process conditions for HSRW on the other hand are not explicitly known so trying to use an empirical formula to relate contact resistance to the conditions will always pose a challenge, but most importantly there is the presence of tin on the surface and a weld is being formed. The tin on the surface will be present as metallic tin and iron/tin intermetallics, the metallic tin will melt and flow away due to the welding load and also the intermetallic tin may be removed. Not only this but the surfaces will be brought into such close contact that grains will nucleate on the surface and grow into both materials [Blom, 2006]. Contact resistance between the electrode wire and the sheet has been measured as small [Basarab Horwath, 1988] and is not taken into account in the present model.

A comprehensive treatment on electrical contacts is published by [Slade, 1999]. Contact resistance is stated by [Slade, 1999] to be independent of sample geometry and dependent only on plastic flow stress, H, load, F and resistivity, β.

$$R_c = \left(\beta^2 \chi \pi H / 4F\right)^{1/2} \tag{3.4}$$

χ is a dimensionless coefficient to take into account material cleanliness that takes a value of unity for perfectly clean interfaces, and assumed as 1.0 for the below calculations.

Table 3.1: electrical resistivity and flow stress at elevated temperatures used in calculation of Figure 3.14 for steel-steel contact resistance [Goldsmilth, 1961].

Temperature (°C)	Resistivity (Ωm)	Flow Stress (MPa)
25	5.81×10^{-8}	3.24×10^{8}
200	2.16×10^{-7}	2.87×10^{8}
800	1.10×10^{-6}	1.59×10^{8}
1000	1.16×10^{-6}	1.16×10^{8}

Employing this equation over those temperatures seen in the weld gap and using the data given in Table 3.1, data for a mild steel, results in the relationship displayed in Figure 3.14.

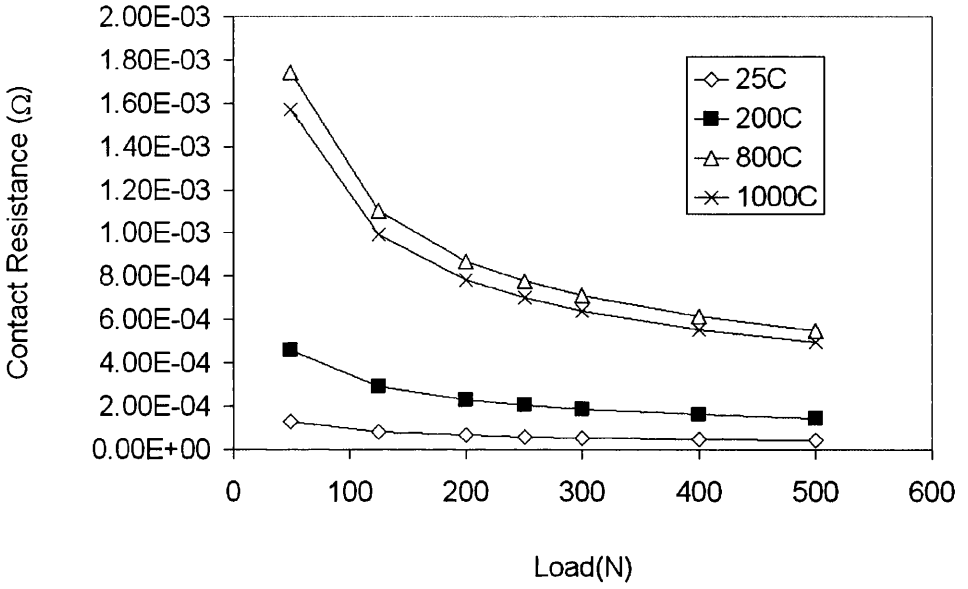

Figure 3.14: calculated contact resistance over several temperatures and loads for steel-steel contact.

The susceptibility of contact resistance to these parameters is clearly displayed in Figure 3.14. These predicted data correlate favourably with experimental data in Figure 3.15 in overall shape, but they do not predict the order. [Song, 2005] also noticed this, although more pronounced for aluminium and stainless steel, and put it down to the complicated interaction of the mechanical and electrical properties of the material and surface film.

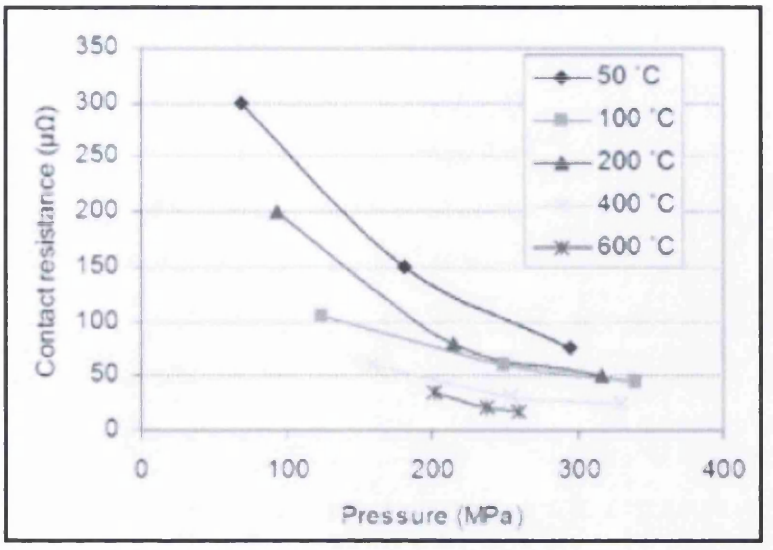

Figure 3.15: experimental measurements of contact resistance and how it varies through change in temperature and pressure [Song, 2005].

In HSRW the substrate could be approximated as "mild-steel-like" in the above demonstration of Equation 3.4, but the presence of tin on the surface would be neglected. There are equations, summarised by [Slade, 1999], to quantify contact resistance of a coated surface but each one is quite specific to a particular situation, for example where the size of contacting asperities are comparable to the thickness of the coating, none of which deals with the presence of liquid metal between the two components of interest. As an approximation of a contact situation where tin is on the surface of the objects being brought into contact one could use the data in the below Table 3.2 for tin to give the contact resistance.

Table 3.2: revised electrical resistivities and flow stresses at 4 temperatures for calculation of Figure 3.16, taking into account the tin on the surface of the tinplate, approximated as tin-tin contact [Goldsmilth, 1961].

Temperature (°C)	Resistivity (Ωm)	Flow Stress (MPa)
25	1.09×10^{-7}	4.00×10^{7}
200	4.05×10^{-7}	1.00×10^{5}
800	2.07×10^{-6}	0.0 (Liquid)
1000	2.18×10^{-6}	0.0 (Liquid)

The response, Figure 3.16, is now obviously modified by the presence of tin because tin has such a small melting point in comparison to carbon steel so there is effectively no resistance offered due to the constriction of current flow.

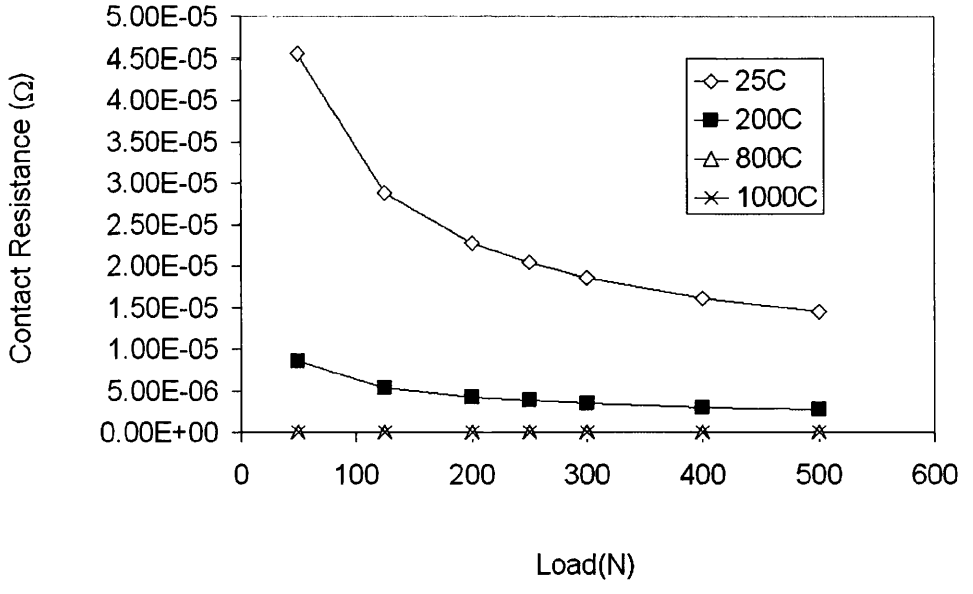

Figure 3.16: calculated electrical contact resistance for tin-tin at several load/temperature situations.

Because the tin is in the liquid state the contact is perfect between the two surfaces of steel; there are no gaps as would be expected when two solid faces are brought into contact so the problem is not due to contacting surfaces as is frequently assumed in the literature. The characterisation of the higher resistance

offered at the interface is actually a complicated problem that has not received a treatment in the literature.

Work on HSRW frequently refers to this phenomenon using the term "contact resistance", as opposed to "contact resistivity". Resistivity (Ωm) is different to resistance (Ω) but they often appear to be used interchangeably in the literature. Resistivity is a material parameter whereas a body's specific geometry and resistivity will give the resistance of that body. The resistivity of liquid tin has been the subject of research for a number of years [Roll, 1957][Scala, 1953][Takeuchi, 1962] and has been compiled together in Figure 3.17 below. FeSn resistivity is published by [Stenström, 1972] as a value of around 80 μΩm at room temperature.

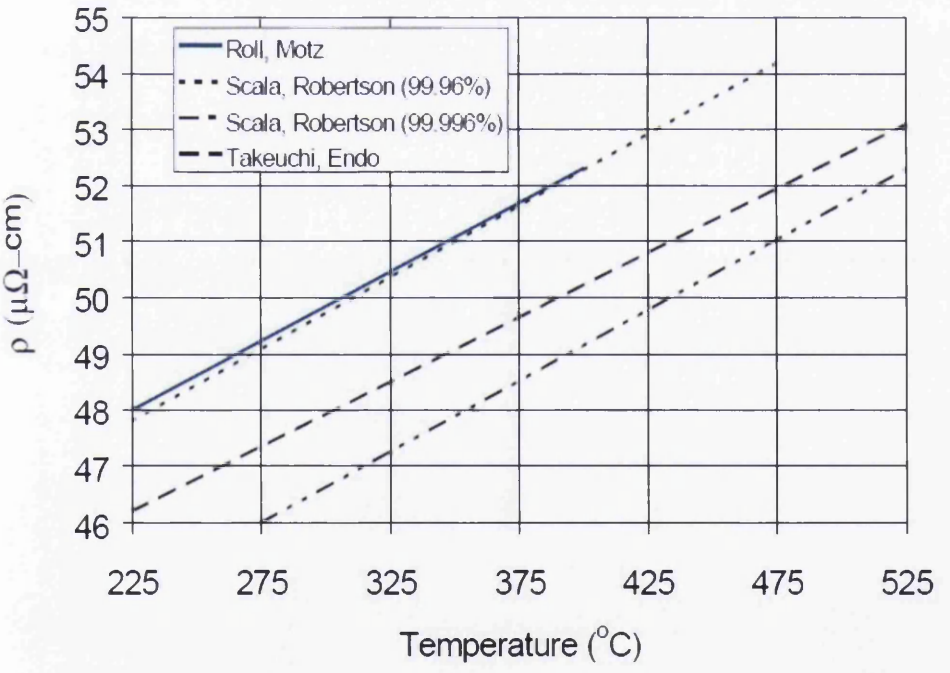

Figure 3.17: electrical resistivity of tin in the liquid state measured by experimentation [Roll, 1957][Scala, 1953][Takeuchi, 1962].

To model the film of liquid tin in between the two sheets of steel would ideally require a layer of elements designated as tin with appropriate thermo-physical

properties. Due to the difference in length scales, tin coating weights are typically about 2.8 g m^{-2} and this is an obvious problem when a macroscopic model of HSRW is the aim in this body of work. The assumption has had to be made that a higher resistivity is specified at nodes in the mesh designated as the interface. This assumption takes into account the effect of the tin layer, providing higher heat evolution, even though the tin is less than explicitly modelled. When this route is taken the value of the resistivity assigned should not be the temperature dependent value of resistivity for molten tin because the values at the interfacial nodes also have to reflect the resistivity of the steel substrate: the resistivity is a combination of both bulk steel and a film of tin. Further justification of this assumption can be given when considering exact, and immeasurable, quantities of components of the interface resistivity are discussed such as iron-tin intermetallics, tin oxides, iron oxides as well as contaminants such as oil.

If this situation was not complicated enough the variation of this value and its variation with respect to temperature is even harder to ascertain because of different melting temperatures of SnO (1080°C), SnO_2 (1630°C), FeSn (607°C), Fe_3Sn_2 (765°C) and Fe_2O_3 (1565°C). Figure 3.18 below shows the region, represented by the dotted line, where higher resistivities are applied to the interface nodes.

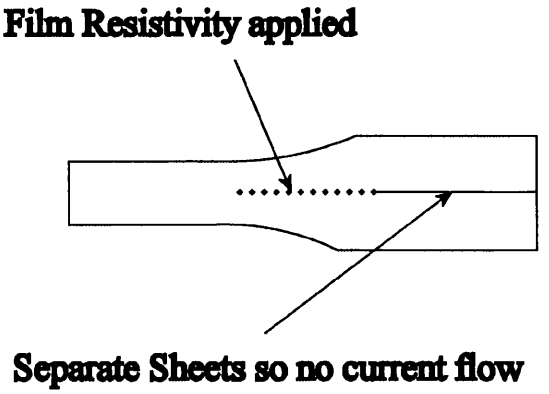

Figure 3.18: schematic representation of where electrical resistivity of the liquid tin between the sheets in the weld gap are modelled with a bulk multiplier. Material moves from right to left.

3.8 Boundary Conditions

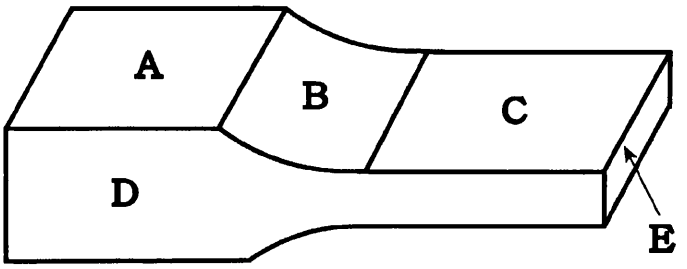

Figure 3.19: areas of the mesh where boundary conditions are applied.

Figure 3.19 is a schematic and simplified drawing of the mesh as it passes through the weld gap. The mesh moves from left to right and section 'B' is in contact with the roll. The model's behaviour is governed by differential equations that are applied to the discretised continua and are solved subject to boundary conditions; the calculation of the electrical field is a boundary value problem. The boundary conditions are an input of vital importance along with the material parameters. The dependent variables that form the solution to the problem are solved according to these boundary values and parameters as well as the independent variables.

3.9 Voltage Field

From a modelling perspective, in order to simulate the effect of voltage application to a conductive body of interest and to calculate the voltage field when the global equilibrium equations are solved the voltage needs to be fixed at relevant nodes in the mesh. The relevant nodes are decided upon in the contact algorithm and are the same nodes that have been fixed in the prevailing timestep for the stress analysis. The nodes that are also part of the upper surface are fixed to a positive value and the nodes that are also part of the lower surface are

fixed to a negative value. In Figure 3.19 above zone 'B', the area of nodes in contact with the rolls is fixed in terms of electrical potential as Dirichlet boundary conditions, the others are subject to the Insulation boundary condition (equation 3.7). Where C_V is the fixed voltage scalar, V is voltage and x is the direction normal to the surface in contact to the electrode roll,

$$V = C_V \tag{3.5}$$

At this time it also seems appropriate to mention the approximation of the sine wave signal of the Alternating Current. Modern HSRW machines' voltage, and therefore current application, and how it varies with time, is controlled by *solid state frequency converters* as opposed to *rotary frequency converters*. Rotary frequency converters rely on rotating electrics to control the frequency of the AC and thus provide a perfectly smooth sine wave. The solid state variety as the name suggests control the frequency by another method that by contrast only offers an approximate sinusoidal waveform that varies in magnitude above and below the sine wave with very high frequency and almost has a *spiky* nature to it. This means that the present model better serves as a model of an older machine with a rotary frequency converter, it is worth pointing out here to the reader that two machines with two different frequency converter types and all the other settings the same will not produce comparable welds.

A weld voltage is very rarely applied as a machine setting rather a weld current is applied so to model this one has to assume that Ohm's Law applies. Ohms Law is easily applied to a sample of simple geometry when one knows the resistivity of the sample and that resistivity is constant. In a more complicated set up such as HSRW the resistivity, though known as a function of temperature, is useless because the current path is so complicated. This entails the use of an arbitrary value for the voltage that is subsequently corrected after the numerical analysis of the voltage field. In the model use of this technique means that the voltage field is solved using the arbitrary voltage, it is then differentiated and the current

density calculated. The current density multiplied by the area through which it flows is of course the current so this is easily worked out on an element-by-element basis for the upper and lower electrode contact areas, resulting in the effective calculated welding current. Because linear elements are used the welding current is linearly related to the voltage applied so a simple correction factor is all that is needed to transform this first guess exactly to the desired weld current. Finally, discretisation in time is performed by setting the time increment to be 1/20th of the AC cycle.

3.10 Transient Thermal Field

With reference to Figure 3.19 the boundary conditions for the thermal part of the model are as follows. Heat loss to the rolls is governed by a Neumann boundary condition, and is applied to zone 'B' with a heat transfer coefficient, C_T, with a value of 8000 $Wm^{-2}K^{-1}$. Similarly zones 'A' and 'C' have Neumann boundary conditions to model heat loss to the atmosphere with a heat transfer coefficient of 25 $Wm^{-2}K^{-1}$. The Neumann boundary condition applies a heat flux, q (Wm^{-2}), normal to the surface to which it is applied,

$$q = -C_T(T_n - T_a) \tag{3.6}$$

Where T_n is the nodal temperature (K) and T_a is the ambient temperature (K), for example. Zones 'E' and 'D' have insulation boundary conditions as 'D' is the outer edge of the mesh and is therefore in contact with 'D' the other side due to the can body being a cylinder. Zone 'E' at the right is periodically deleted and zone 'E' at the left entering the weld gap is periodically created as part of the re-meshing. Both zone 'E's have the insulation boundary condition applied. This is a valid assumption because heat generation is more important than heat flow when welding speeds are higher than appreciable heat diffusion distances and on the

left zone 'E' no heat generation is calculated because it is sufficiently ahead of the weld gap. Where V would be voltage, or alternatively T where T Temperature,

$$\frac{\partial V}{\partial x} = \frac{\partial T}{\partial x} = 0 \tag{3.7}$$

3.11 Running the Model

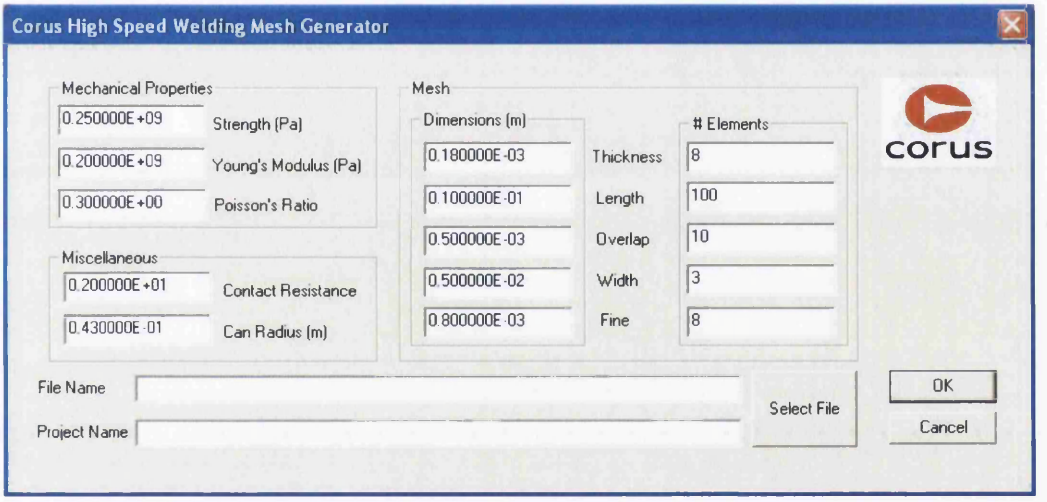

a)

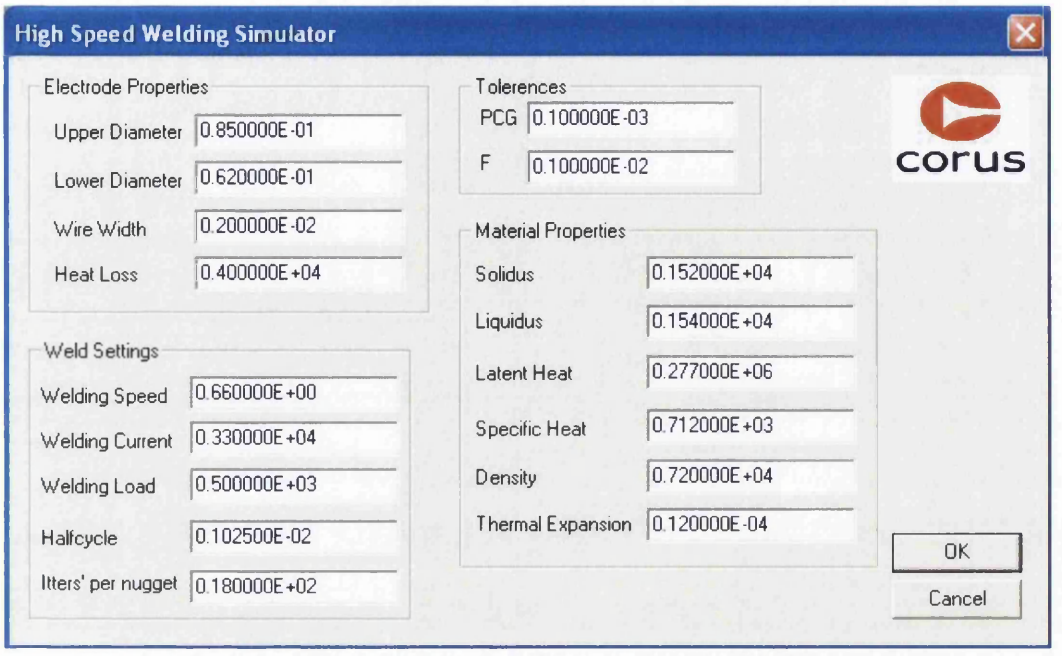

b)

Figure 3.20: Windows based Graphical User Interfaces for both mesh generation, a), and running the model, b).

A GUI has been written and is shown in Figure 3.20 a) and b) above to control the model so users unfamiliar with FORTRAN95 do not have to go into the code and change variables or parameters. There are two separate GUIs, one for the mesh generation and one for the High Speed Welding Simulator. Running the model to produce the results that are described in the following section requires only small inputs from the user for the following settings:

- Nugget pitch
- Weld speed
- Welding load
- Upper and lower electrode diameters

The geometric settings of the mesh are set in the mesh generation programme. Table 3.3 below gives the geometry and divisions of the mesh; there are two sections in the sheet with differing element densities, sheet width 1 is closest to

the overlap and sheet width 2 is closest to the edge and both combined give the total width of the mesh.

Table 3.3: mesh geometries and densities used in the model.

Specification	Value
Length	7 mm
Sheet Width 1	1 mm
Sheet Width 2	6 mm
Overlap	0.5 mm
Thickness	0.18 mm
No. of nodes in length	70
No. of nodes in width 1	14
No. of nodes in width 2	4
No. of nodes in overlap	7
No. of nodes in thickness	5

Material parameters are set in the programme code and the values for these parameters are detailed in Table 3.4. Where two values are quoted the value used in the calculation varies between them linearly with respect to temperature at 25 °C and the liquidus.

Table 3.4: physical material parameters used in the model.

Parameter	**Value(s)**	
Liquidus (°C)	1540	
Solidus (°C)	1520	
Latent Heat of Fusion ($kJkg^{-1}$)	277	
Density (kgm^{-3})	7850	7200
Thermal Conductivity ($Wm^{-1}K^{-1}$)	35	15
Coeff.Thermal Expansion (K^{-1})	12e-6	
Specific Heat Capacity ($Jkg^{-1}K^{-1}$)	450	900
Yield Strength (MPa)	550	5.5
Young's Modulus (GPa)	200	2
Poisson's Ratio (dimensionless)	0.3	

Electrical resistivity with respect to temperature follows a more detailed curve as it is this that determines the extent of the Joule heating. The curve used is shown in Figure 3.21.

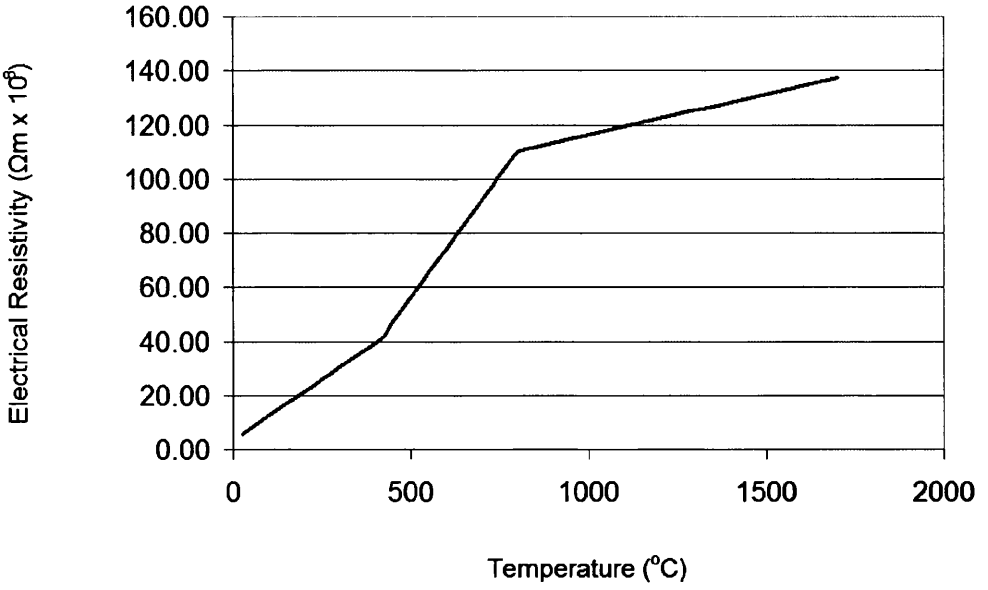

Figure 3.21: electrical resistivity used for the model with respect to temperature.

The desktop computer used to run the simulations has a CPU speed of 3.0 GHz, RAM of 2.0 Gb with a Front Side Bus of 1.3 MHz and Cache memory of 2.0 Mb. Run time is about 20 hours to simulate 10 nuggets where equilibrium is reached.

4.0 RESULTS

4.1 RESULTS SECTION I – VERIFICATION AND VALIDATION

The reader has now been made aware of how the model has been developed with all assumptions and omissions declared, now the following section will detail the use of this numerical model of the High Speed Resistance Welding process. This first section of results will explain the verification and validation of the model.

4.1.1 VERIFICATION

Verification of a model is crucial before any useful exploitation is possible. Verification, like validation is a crucial part of software development and is used to check that there are no bugs or errors and also to see that the results are relatively comparable to actual experiments. At first it seems sensible to run a single simulation to show that the model is stable and convergent to an equilibrium situation which models the assumed equilibrium of the actual process, ignoring end effects and so on. Figure 4.1 below shows both the upper and the lower areas of contact determined by the contact algorithm, these nodes in contact are then subjected to the boundary conditions discussed in the preceding 'model formulation' section.

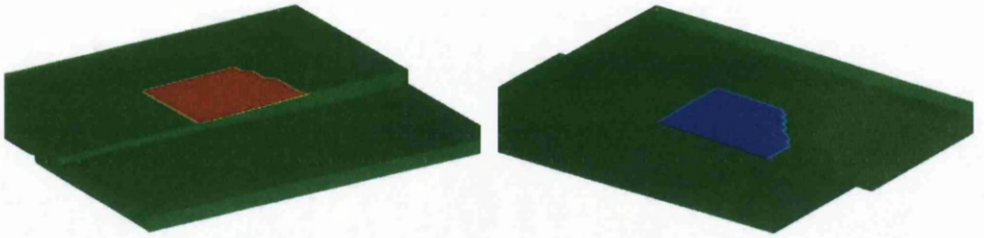

Figure 4.1: upper (left) and lower (right) contact areas identified by the contact algorithm and used in electrical, thermal and mechanical analyses.

Once the boundary conditions have been applied and a solution calculated for the stress analysis, the shape of the mesh is changed by the deformation caused by the two electrodes held under constant load, the welding load. The deformed mesh in Figure 4.2 is reached after several tens of timesteps and the model has reached equilibrium. The view is down the welding direction looking from the lower right toward the front face of the mesh. This front face will have been freshly introduced during the automatic mesh regeneration process and hence the weld stack up is completely undeformed. Further down the mesh as it is subjected to the effects of the electrodes the consequential deformation is clearly seen.

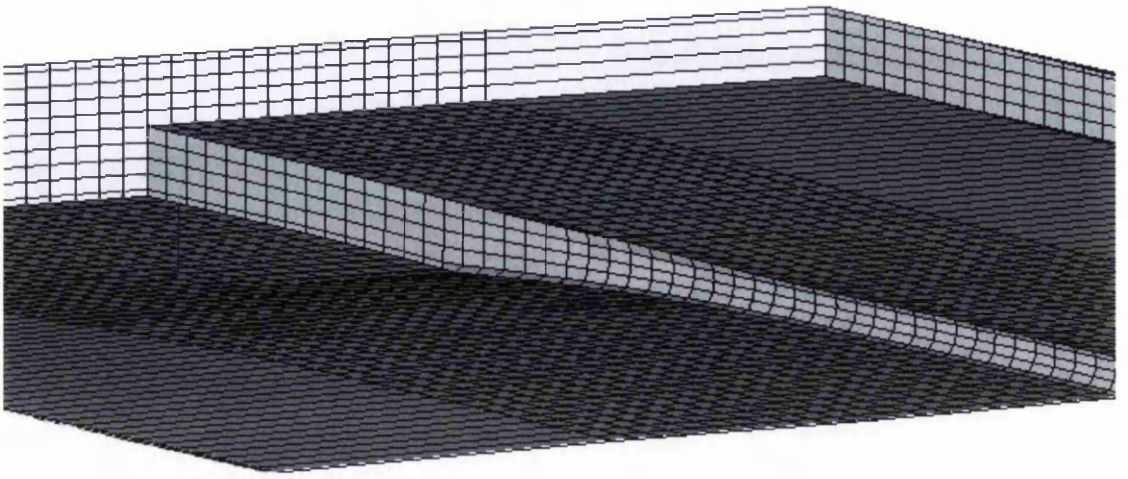

Figure 4.2: deformed mesh.

Figure 4.3 below displays a few examples of cross sectional and 3D post processed output files. The 4 fringe plots show the capabilities of a model and it appears that what one would intuitively expect to be happening within such a model is certainly happening.

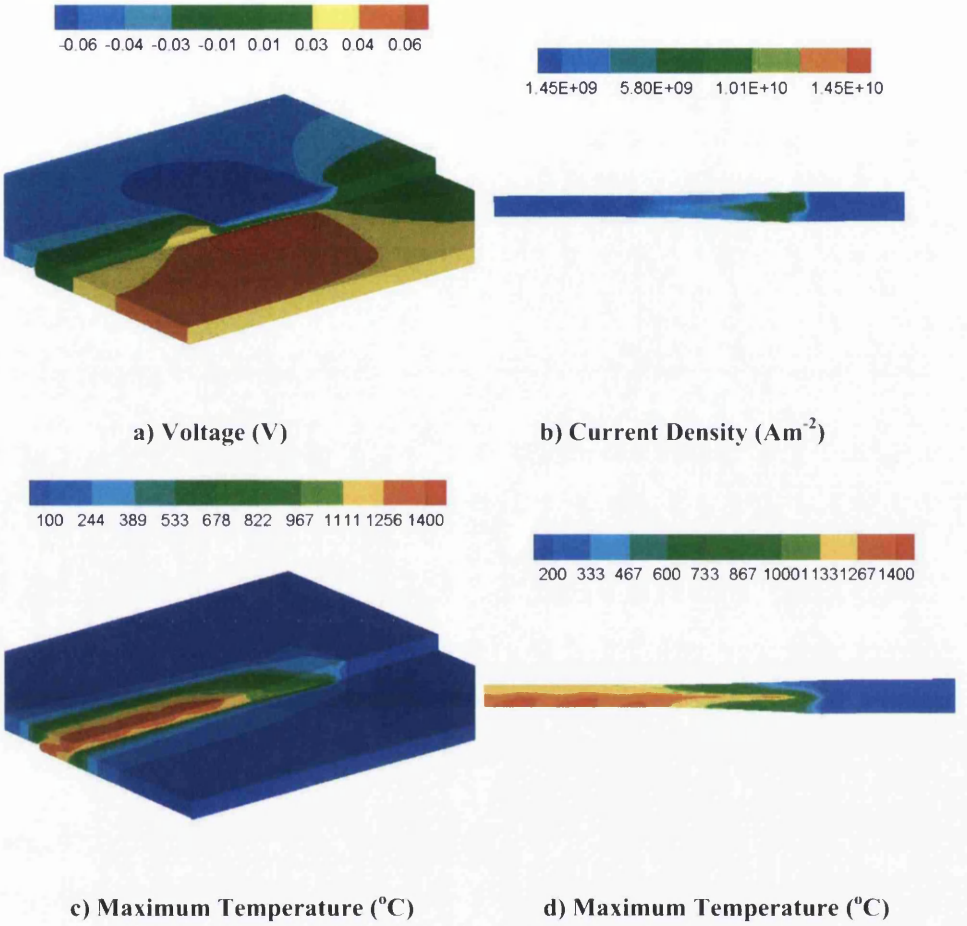

Figure 4.3: example fringe plots of the simulation at 30 m min^{-1} and with a current of 3400 A. The voltage, a), is differentiated to give the current density, b), this is used to give the Joule effect that supplies the heating, c) and d) offers a cut through to reveal the internal heat generation pattern.

Figure 4.3 a), in the top left, the 3D voltage distribution is displayed. This is outputted after the first part of the electro-thermal analysis and it is this voltage field that is differentiated to give the gradient that is used to calculate the current density. The current density distribution in Figure 4.3 b) consequently gives rise to Joule heating, the extent of which in each timestep affects the transient temperature distribution; Figure 4.3 c) and d). Figure 4.3 c) is a 3D plot, such a plot style is not always the most useful method of viewing results and greater insight is achieved when a 2D cross section is taken. This is analogous to taking a polished and etched micrograph of a weld as opposed to simply viewing the

external surfaces. Comparably, when one takes such a 2D section the internal independent variable distributions allow elaboration on any theory of weld formation, but the simulation offers the investigator the opportunity to view such distributions in real time, more useful in comparison to post weld microstructures.

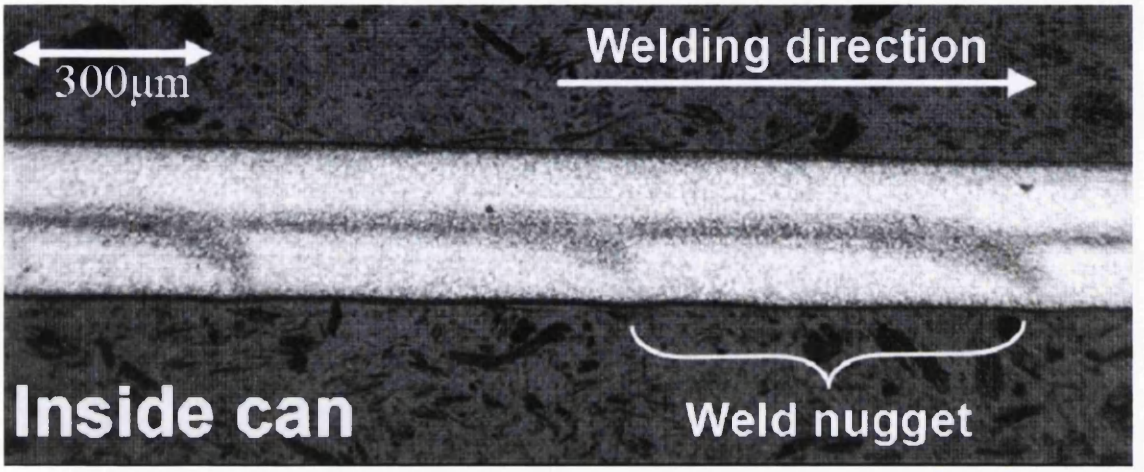

Figure 4.4: tangential polished and etched seam [Elzinga, 2005].

The above micrograph in Figure 4.4 is typical of a fully formed weld. When compared to the model output in Figure 4.3 d) the predicted heat generation pattern appears to be replicated i.e. the highest heat input is at the overlap but also curves down towards the smaller lower electrode where current density is higher. Thus visually the model is capturing the observed behaviour in real welds.

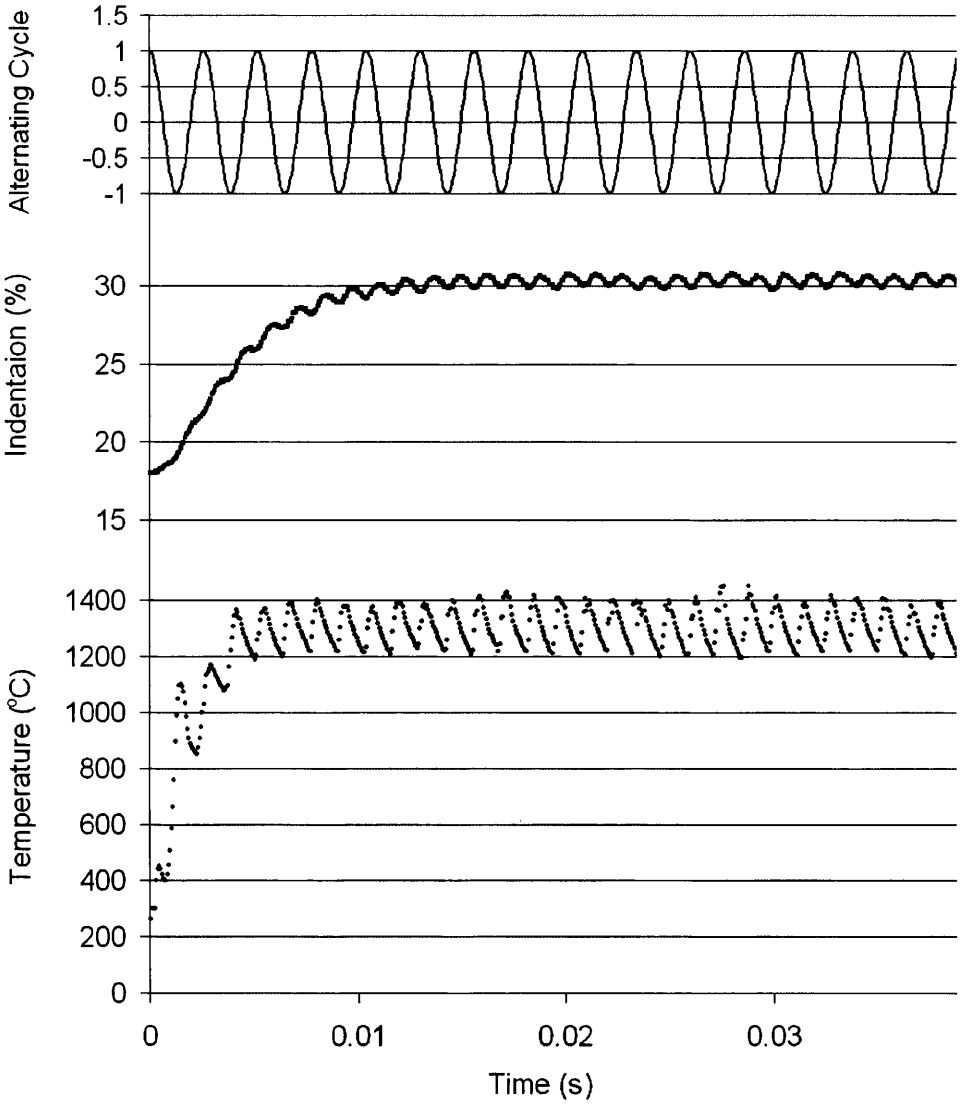

Figure 4.5: temperature and indentation variation with the AC cycle output from the model at 30 m min^{-1} and with a current of 3400 A

Graphically, the stability of the model can be demonstrated in the above graph, Figure 4.5. By 200 timesteps the model has reached a steady state that oscillates periodically with the AC and is numerically very stable. The results so far somewhat verify the model in that the model behaviour seems sensible, the quality of the results indicate that sufficient physics has been captured in the

model and there are no detectable bugs (and with some degree of certainty no obvious errors).

4.1.2 VALIDATION

Validation is the phase of model development where a model is determined to be fit for purpose, normally after comparison to a measurable quantity from experimental results. After validation the model is considered sufficiently correct to permit proper exploitation. The model can be used to investigate extrapolative/interpolative untested situations and determination of other quantities un-retrievable by physical experimentation.

4.1.3 RE-MELTED TIN ZONE

The re-melted Tin Zone (RTZ) is suggested in work by [Suthar, 2005] to be a measurement that can be used for validation of a HSRW model. The RTZ is effectively a 232°C isothermal line on the post weld surface of the tinplate and is caused by the heat generated during the welding conducting away from the weld overlap. The heat generated during welding is considerably higher than the melting point of tin (232°C) so this causes the fine coat of tin to melt and then re-solidify, thus the surface is visibly different due to the fact that the solidification conditions are different to those seen in the 'flow melting' stage of tinplating. Figure 4.6 below shows the clear visibility of the RTZ.

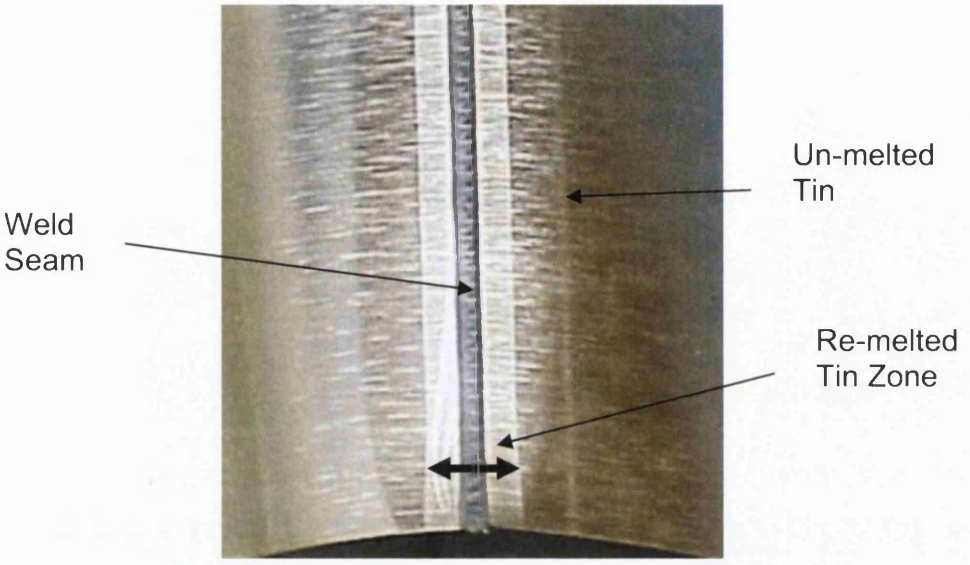

Figure 4.6: welded seam and the Re-melted Tin Zone.

The RTZ is easily measurable both experimentally and numerically; this is why it is seen as a robust measurement for validation. Experimentally it is a case of using a Vernier scale on a light microscope but numerically it requires that a weld is cooled down to less than the melting point of tin. To get a result for the RTZ from the model entails the simulated cool down of the simulated welds. Simulation of a weld cooling down to 231°C takes a considerably longer time than a simulation of weld formation because the time taken is much longer in reality for the former in comparison to the latter. If a measurement was to be taken from the FE calculation a very long mesh would be needed to allow cool down to happen on the same mesh as heat generation. A separate program has been developed to calculate the RTZ by using a few simplifications.

4.1.4 Finite Difference – RTZ Calculation

A Finite Difference program has been developed, also in FORTRAN95, to simulate the weld cool down stage. The RTZ calculation program makes the assumption that because the RTZ is a band, a 2D simulation will be adequate.

Simulation in 2D is less computationally intensive than 3D so the time taken is appreciably less.

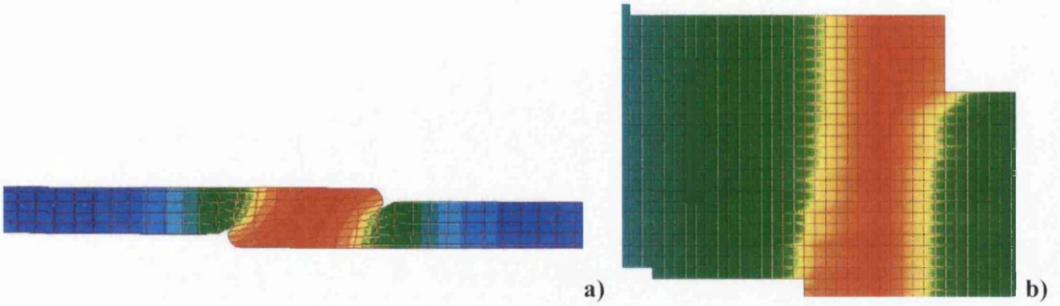

Figure 4.7: Finite Element mesh a) and Finite Difference mesh b)

Figure 4.7 above demonstrates how a nodal plane of the 3D Finite Element mesh, a), which is to be cooled down, is mapped onto a 2D FD mesh shown in b). The FD mesh is plotted as a series of cells that is much finer than the original FE mesh ensuring that a sufficient level of detail is captured. A timestep is decided by the Courant-Friedrich-Levy Stability criterion so solution is guaranteed for that mesh size.

Table 4.1: machine settings and mechanical material parameters used in the model.

Process Parameter	Value
Welding Load	500 N
Upper Electrode Diameter	85 mm
Lower Electrode Diameter	47 mm
Material Young's Modulus	200 MPa
Material Yield Strength	550 MPa
Material Poisson Ratio	0.3

Experimental data for RTZ measurements has been produced for validation of the model through an extensive test program on a Soudronic AFB1075 seam welder, displayed in the Figure 4.8. This experimental work was carried out by

[Elzinga, 2007] at Corus, IJmuiden in Holland. The above Table 4.1 has all the process settings used in both the experimental tests and numerical simulations.

Table 4.2: experimental data of those weld settings that resulted in good welds [Elzinga 2007].

Welding Speed ($m\ min^{-1}$)	Nugget Length (mm)	Lower Limit (A)	Upper Limit (A)
20	0.5	2850	3600
	0.6	2800	3450
	0.7	2750	3250
	0.8	2850	3150
30	0.5	3300	3850
	0.6	3250	3800
	0.7	3200	3600
	0.8	3150	3650
40	0.5	3650	4150
	0.6	3700	4100
	0.7	3700	3900
	0.8	3650	3850
50	0.5	4000	4450
	0.6	3900	4250
	0.7	3800	4250
	0.8	3800	4050

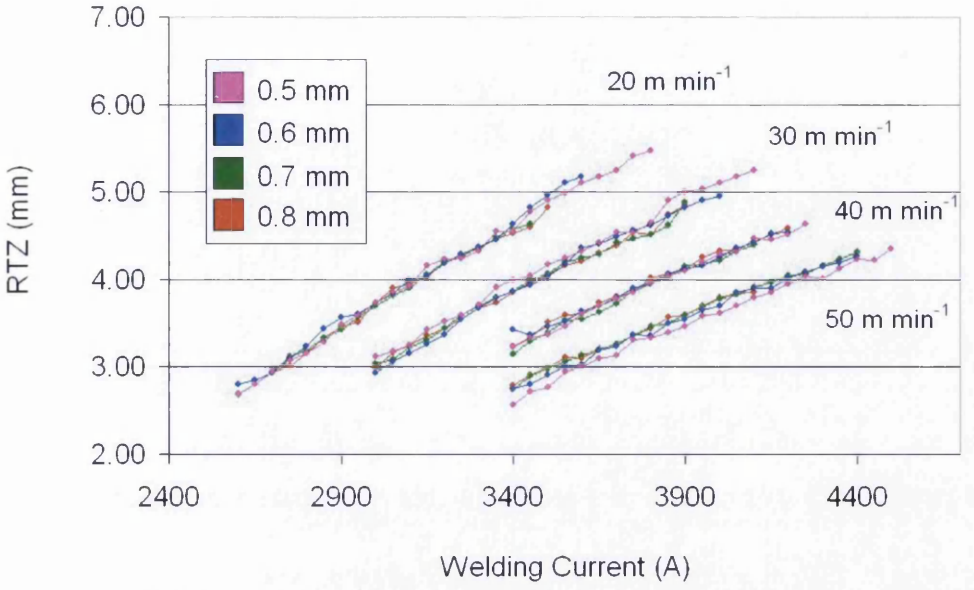

Figure 4.8: experimental data matched for validation of the model.

The welding current and weld speeds have been varied to produce a matrix of tests; welding current is varied so as to encompass cold welds, welds that pass a rip test, and welds that show signs of splash for each of the four linear welding speeds tested, Table 4.2. An average RTZ of 5 cans was taken for each data point. Notice how the machine behaves broadly in a linear fashion as one would expect, as the current is being increased linearly, but there is still some experimental variation. At this point it is worth noting that the weldability of tinplate does not vary linearly between the upper and lower weld limit, experience shows [Elzinga, 2005] that there are particular current values that do not create sound welds, yet welding currents just above and just below do. There is effectively a hole in the welding range. The colours represent different *nugget pitches* of between 0.5 and 0.8 mm but for each of the welding speeds tested nugget pitch has little effect on the RTZ. A nugget pitch of 0.65 mm has been used for all subsequent simulations.

4.1.5 SIMULATION RESULTS

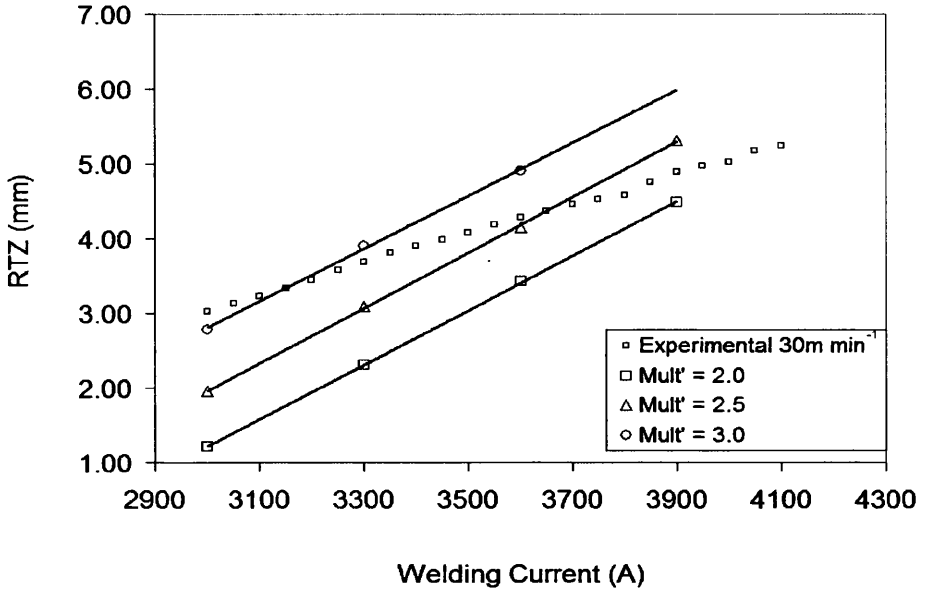

Figure 4.9: RTZ data from the model after variation of the constant bulk resistivity multiplier. Simulated results are the solid lines and the points are the experimental data.

The experimental data values for each welding current have been averaged for the 4 nugget pitches to create a straighter generic line. Repeating such a test numerically with the model should produce a similarly straight line of RTZ values as the current increases. Figure 4.9 does show this fact. There is a slight degree of scatter to the model results probably because the problem has been discretised. More notably the gradient of the line is much too high with a constant value of the contact resistance bulk multiplier. Further investigation of the model demonstrated that the contact resistance is a very sensitive parameter and has a great effect on the RTZ line. The results presented above show how changing the value of the contact resistivity bulk multiplier can vary the value of the RTZ line, but not the gradient with increasing welding current.

This sensitivity is unsurprising based on the literature survey where contact resistance is always mentioned as being very important. However, the difficult

task of ascertaining the contact resistance and how it varies with temperature is not the whole picture. The tin that is electroplated onto the surface of the steel also needs to be removed to allow bonding between the steel to take place [Blom, 2006], if this did not happen then a weak bond would obviously be formed. Also "contact resistance" as it is referred to in the literature is not contact resistance because there are no surfaces in partial contact when molten tin is between them. This has been discussed in the model development section of this body of work. What does seem appropriate is to reduce the bulk resistivity multiplier over a distance approximately where current starts to flow across the two sheets to the point where the bonded material exits the weld gap. This reflects what is physically happening when the liquid tin flows out of the overlap, but this is hard to model on the same mesh due to the differing length scales. A distance-resistivity multiplier relationship is suggested below. The distance is from the centre of the weld nugget forward and is assumed to be at the same distance as the centre of the weld rolls.

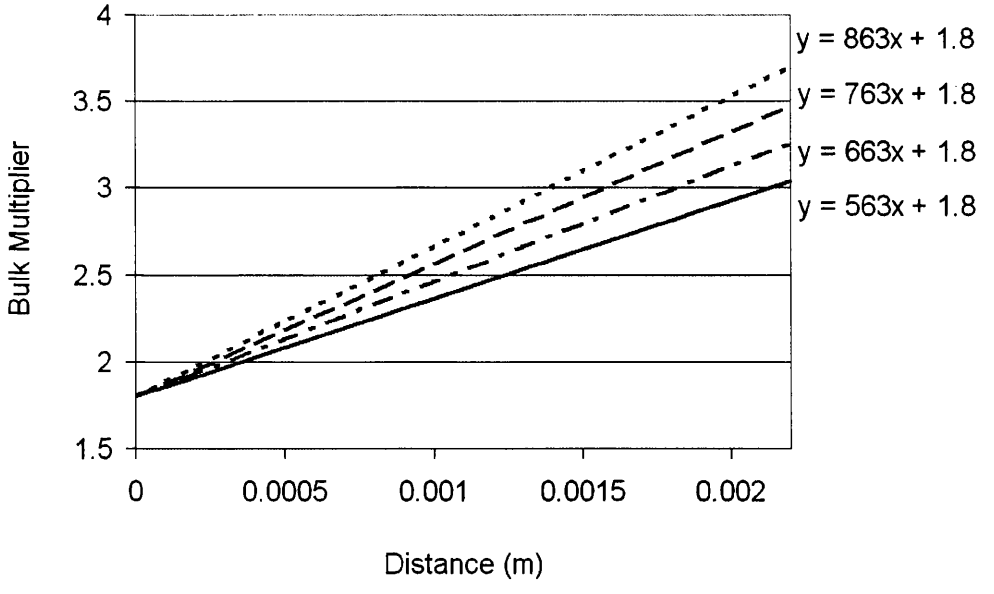

Figure 4.10: bulk multiplier as a function of distance, equations on the right.

When such a situation is allowed in the simulation the predicted results become a lot closer to experimentation, as exemplified in the results below in Figure 4.11. The model appears to be in good agreement to the experimental data now in both gradient and value. Only the line of best fit of the data is shown for clarity. The effect of both increasing and decreasing the gradient of the bulk resistivity multiplier line is shown, decreasing and increasing the gradient of the RTZ line, respectively. The results do not go above 3700 A because for the simulations where the bulk resistivity multiplier has a high gradient, and therefore a high resistivity in the early stages of the weld gap, the temperature becomes numerically unstable.

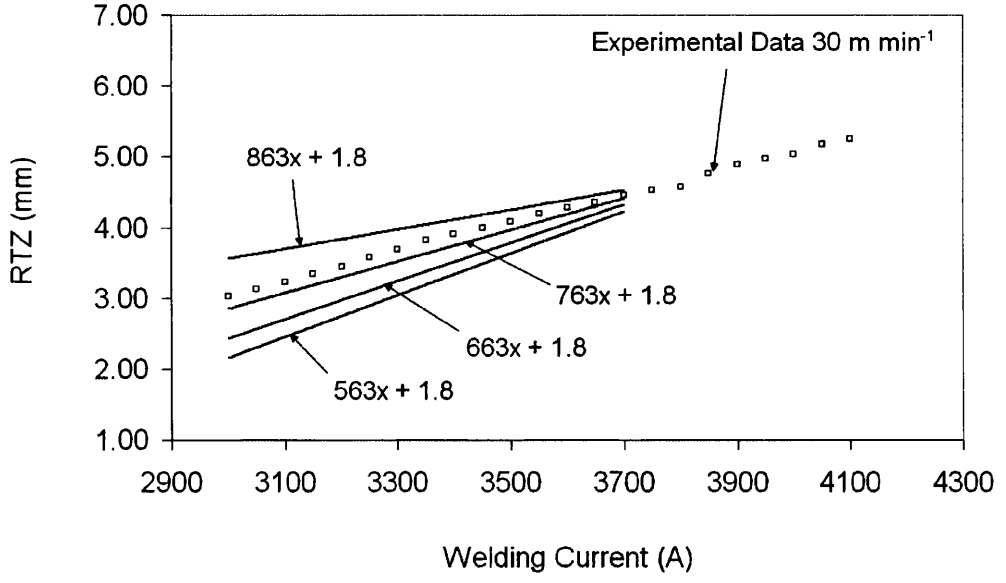

Figure 4.11: RTZ data, the effect of changing the gradient of the bulk multiplier in Figure 4.10 on the thermal behaviour of the model. Simulated results are the solid lines and the points are the experimental data.

The experimental data given in Figure 4.12 is for four welding speeds so using the same relationship for contact resistance the tests were replicated using the model. This time the results are less convincing however and are quite some way off the experimental data and it is not immediately obvious why. There is too

much difference in the values when the speed is reduced and the weld current is held the same as well as the gradient of the RTZ lines being wrong.

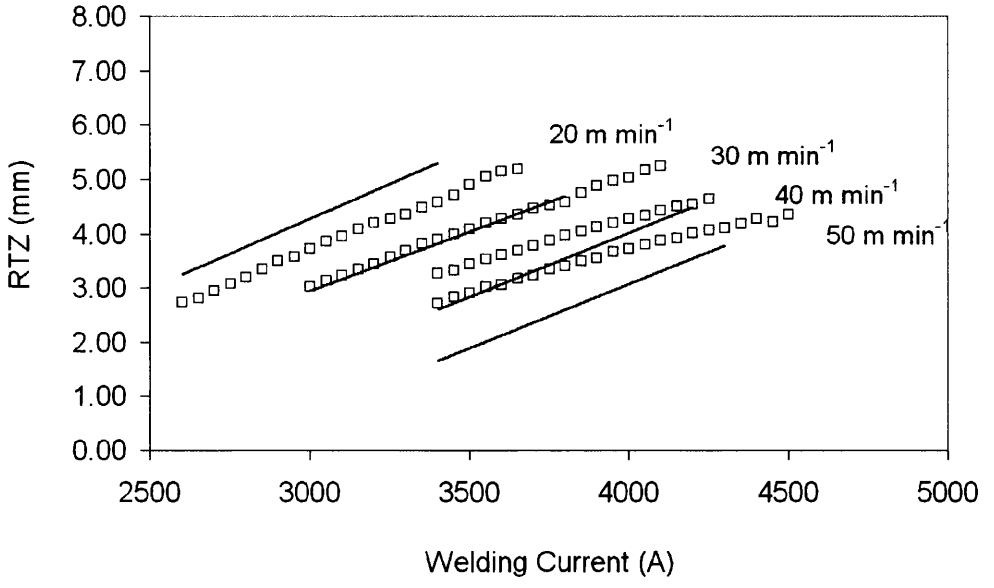

Figure 4.12: RTZ data using a consistent bulk multiplier for the 4 weld speeds. Simulated results are the solid lines and the points are the experimental data.

The contact resistance in the model was thus valid for only one welding speed. When one contemplates how the contact resistance of the process is due to the film of liquid tin, and this tin is also being removed from the interface as it passes through the weld gap, the reason for this is forthcoming. Assuming all else remains equal an increase of weld speed will offer less time for the tin to flow away from the overlap to allow the bond to form, conversely, less time will be offered at higher speeds. So at slower speeds there will less tin and therefore less resistance. When this correction is performed numerically by modifying the contact resistance the results correlate to the experimental results but there is still a rather large gap between the RTZ lines of 20 m min^{-1} and 30 m min^{-1}, see Figure 4.13.

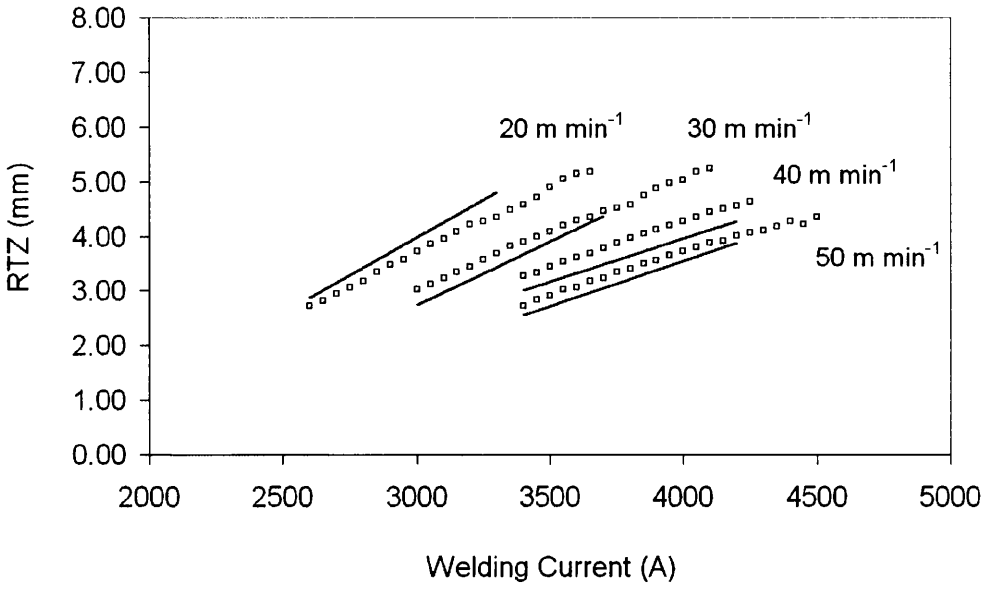

Figure 4.13: RTZ data using a non consistent bulk multiplier function. Simulated results are the solid lines and the points are the experimental data.

The contact resistance used is plotted in the graph, Figure 4.14.

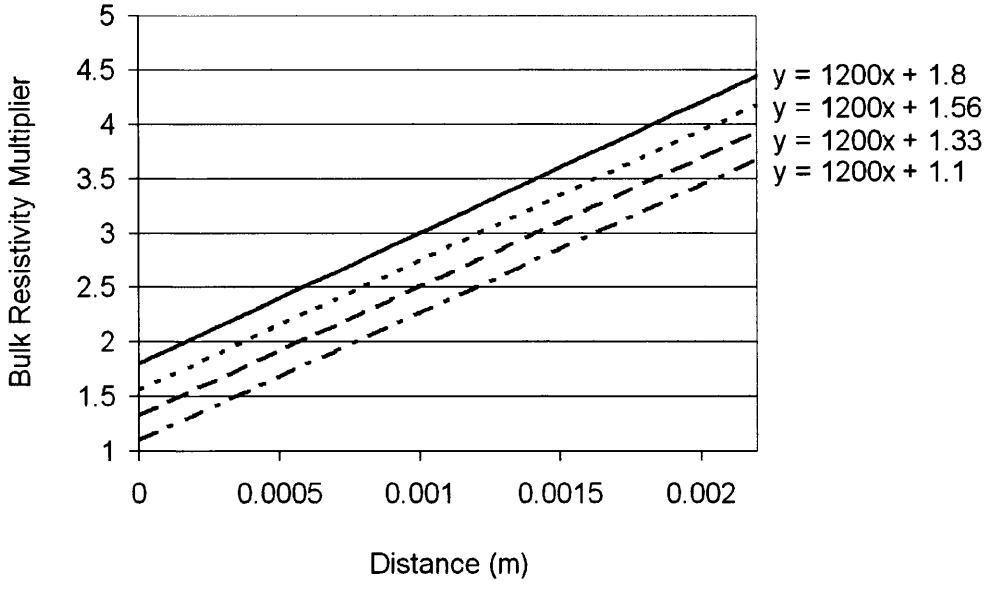

Figure 4.14: bulk multiplier used in simulations to generate data for Figure 4.13. Simulated results are the solid lines and the points are the experimental data. 1200x + 1.8 is for 50 m min^{-1} and 1200x + 1.1 is for 20 m min^{-1}etc.

Although the numerical results correlate with a reasonable degree of accuracy; the assumption that the contact resistance is less for each subsequent reduction in speed at zero distance in front of the weld gap, i.e. where the material is about to leave the weld gap, seems counterintuitive. This is because the weld has formed or is nearing completion and thus the contact resistance should surely be nearly identical, especially for welding conditions that yield a successful weld. [Blom, 2006] speculates about the effect of weld speed when concerned with the bond formation during HSRW, particularly the tin layer behaviour, agreeing that at lower weld speeds there would be less tin present. It would be possible to model such a situation to gain a numerical solution to the problem by constructing a model of the liquid tin flow behaviour by using Computational fluid Dynamics. Such a model would have to be in 3D and coupled to the present stress analysis and involve possibly the melting and solidification of the tin and iron-tin intermetallics, surface tension around the interface as well as dealing with arbitrary free liquid/solid surfaces. This would involve a significant quantity of work as well as further adding to run time and memory requirements of the model. This has been judged to be beyond the scope of this body of work.

In order to achieve a realistic and practical solution to this problem consider the very simple schematic in Figure 4.15. The two plates are separate before they are forced together by the electrode force because the 'z-bar' on the Soudronic welding machine keeps them apart as the blank is fed into the weld gap.

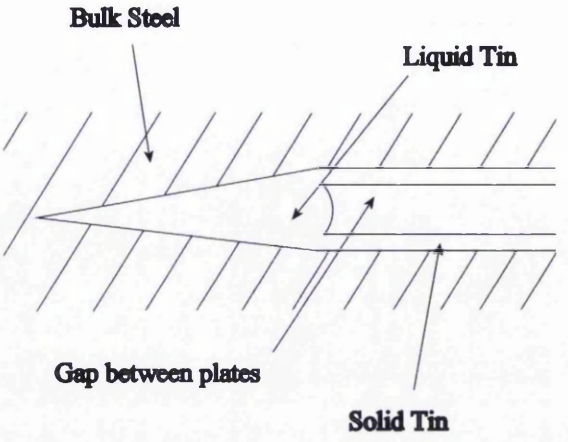

Figure 4.15: schematic of the interface between the two sheets of steel as they are passed through the weld gap and are bonded. The tin escapes laterally from the weld gap into and out of the paper.

Tin is known to end up at the edges of the weld mainly, but some remains at the interface in solid solution according to the in depth study by [Blom, 2006]. Figure 4.16 a) below shows the remaining tin in a Wavelength Dispersive Spectroscopy map and b) shows the tin build up in a partially formed weld. Very little tin is left after a weld has fully formed.

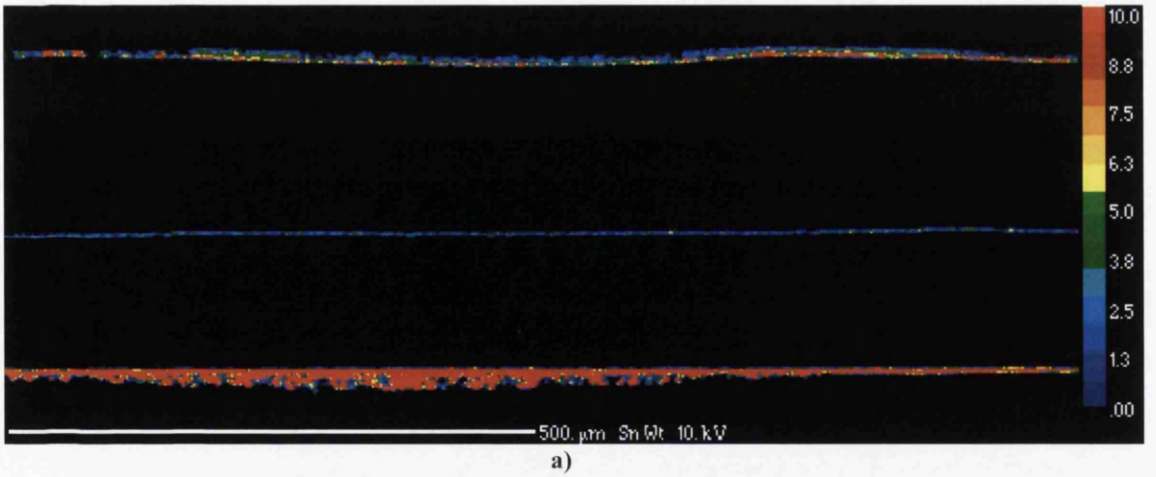

a)

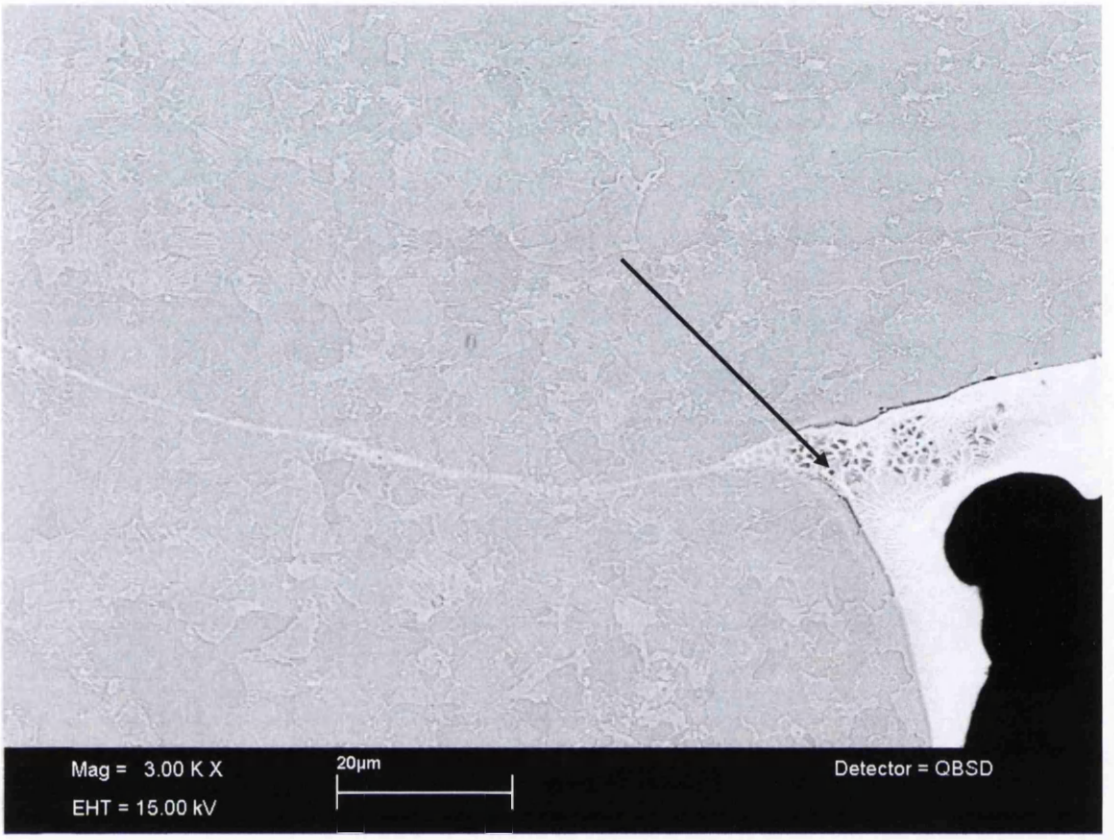

b)

Figure 4.16: tin residuals after welding analysed with Wavelength Dispersive X-ray spectroscopy [Blom, 2006], a), and b), Scanning Electron Microscope image of tin collected in corners after welding [Blom, 2006].

It is very challenging to examine practically what is actually taking place in this situation and thus approximations are necessary in the model of HSRW. Analytical solutions do exist for fluid flow between two parallel plates where both plates are stationary, e.g. plane Poiseuille flow [Brodkey, 2004] where velocity (ms^{-1}) is given as a function of position between the two plates.

$$\frac{dx}{dt} = -\frac{y_0^2}{2\mu}.\frac{dP}{dx}\left(1-\frac{y^2}{y_o^2}\right) \tag{4.1}$$

Where μ is the dynamic viscosity (Nsm^{-1}) (not kinematic), y is the distance (m) at which the velocity is required, P is the pressure (Pa), y_o (m) is half the distance across the gap between the two plates and x (m) is the distance along which the fluid flows. This is a 2D solution so has limited applicability to the problem in hand because flow is in 3D, in both the welding direction and perpendicular to the welding direction, but it gives an important guide to the relationship between viscosity and the flow rate, viz all else remaining equal the flow rate is inversely proportional to the viscosity. It would be easy to suggest that a doubling in welding speed would lead to a halving of the time available for tin to evacuate the interface but this would obviously be an oversimplification. Intuitively though one would expect that the presence of more tin at the higher weld speeds would mean that the gap filled with liquid tin, between the bulk steel of the plates, would be increased. This is because there would not be additional pressure to prevent such a build up as the welding load is held constant due to the spring loading of the upper electrode. Also the presence of iron and tin oxides that contribute to the contact resistance is not taken into account here and kinetics of their breakdown should also be taken into account for a complete analysis. Further complication is added if the surface tension would be analysed.

In light of this one can make a justifiable assumption that because a high proportion of the contact resistance is down to the film of liquid tin between the interfaces, and this film must be thicker at the front because less time is provided for the tin to flow outwards to prevent a build up, then a relationship can be proposed as is depicted in the following Figure 4.17 as a replacement to Figure 4.14 used previously.

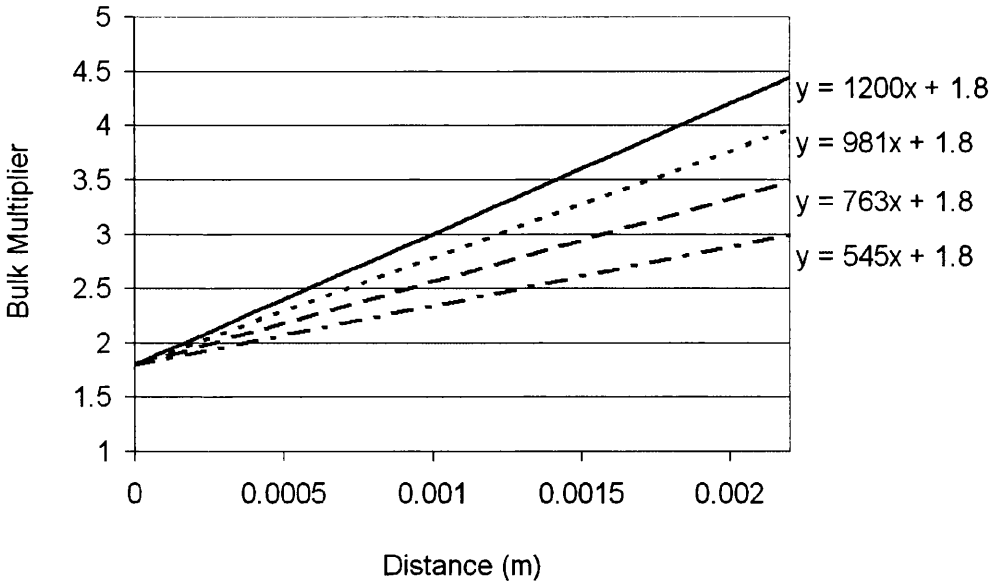

Figure 4.17: bulk multiplier with respect to distance relationship used in final model.

Simulation results using this relationship for contact resistance yields an even better relationship illustrated in the following Figure 4.18.

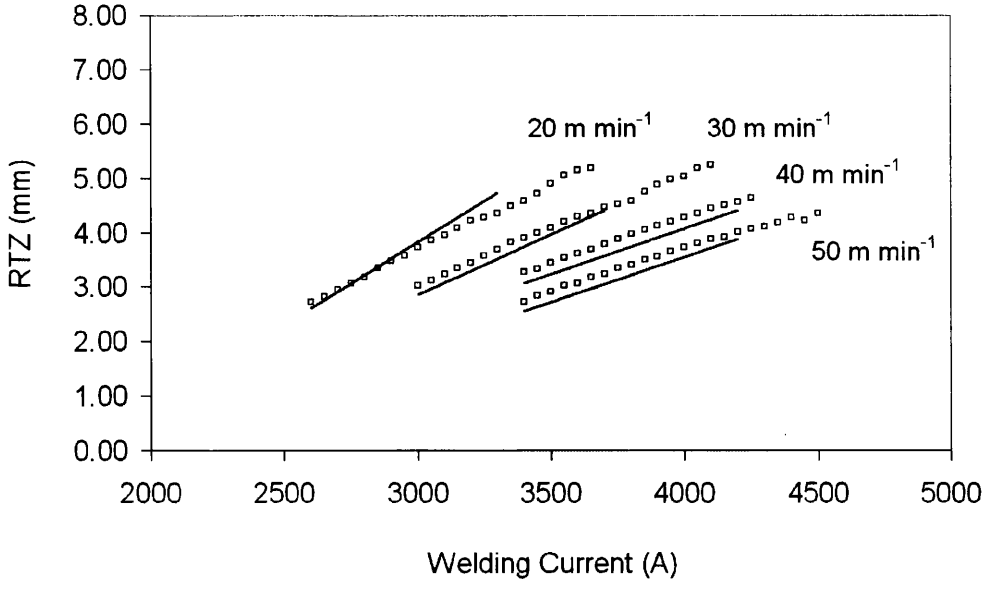

Figure 4.18: validation data of High Speed Resistance Welding model. Simulated results are the solid lines and the points are the experimental data.

A sensitivity analysis was performed for the major material parameters to see the affect on the RTZ line. The parameters that were looked at were density, thermal conductivity, specific heat capacity, electrical resistivity and strength. A change in each parameter of ±10% was simulated and the results displayed in the graphs of Figure 4.19. Each time a parameter is changed there is either an increase or a decrease in the height of the RTZ line but nothing significant changes with the gradient. The contact resistance is clearly the most important parameter of the model.

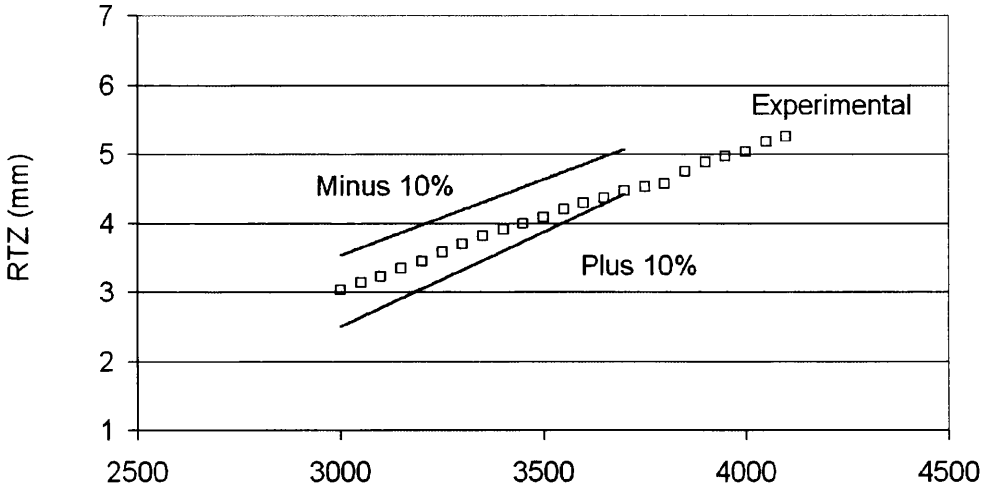

Density

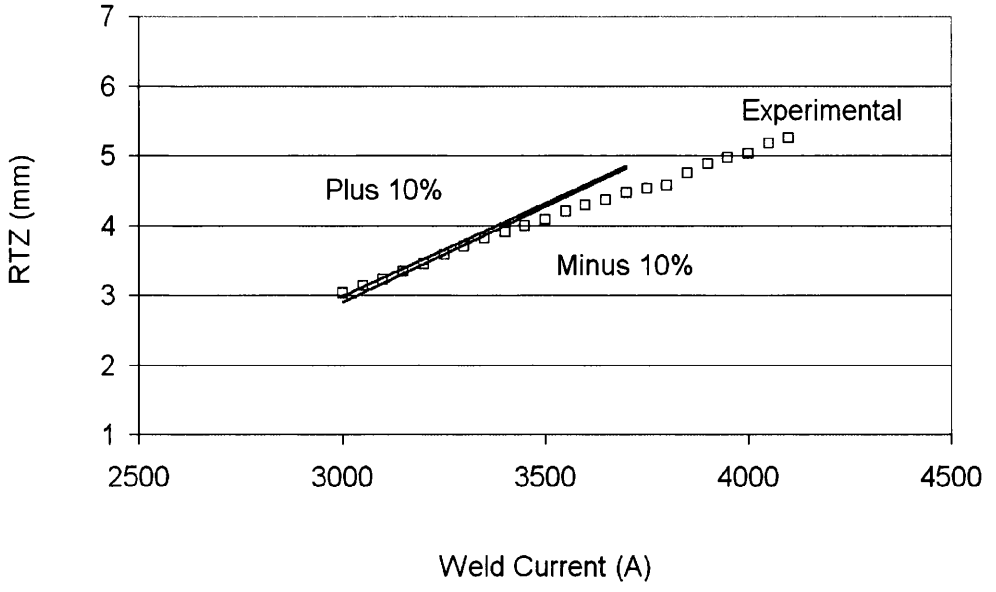

Thermal Conductivity

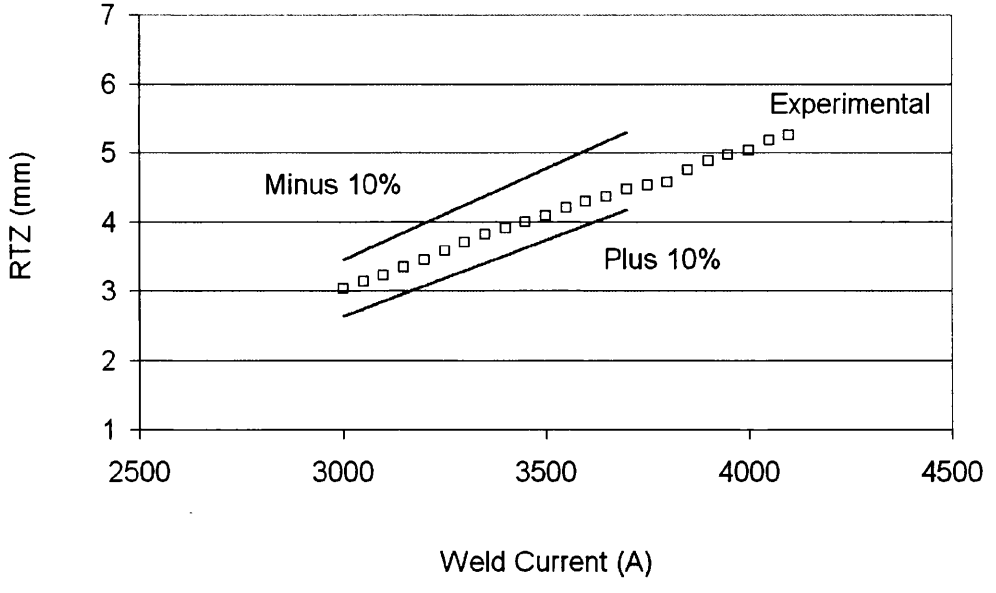

Specific Heat Capacity

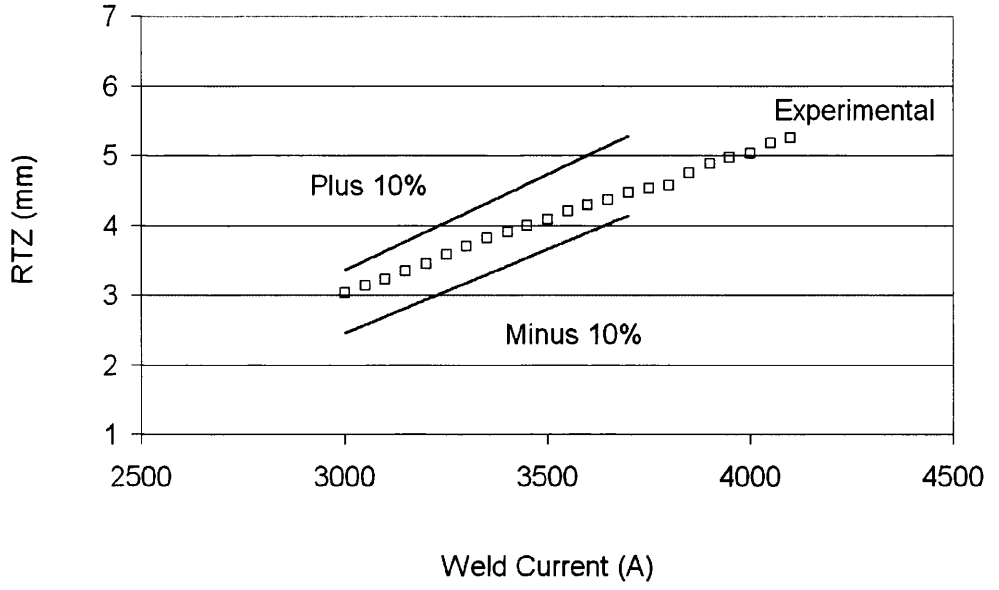

Electrical Resistivity

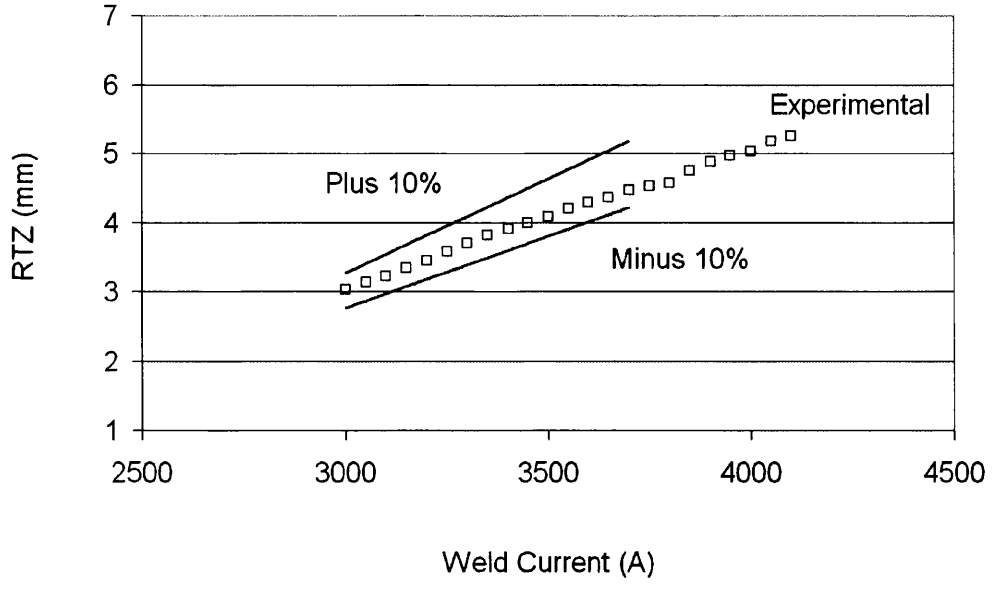

Yield Strength

Figure 4.19: sensitivity analysis. Simulated results are the solid lines and the points are the experimental data.

4.2 Results Section II – Temperature Considerations

At this point the model has been established as showing excellent comparison to measured data and now in this section of the results the focus is shifted to exploitation of the model - at first to look more deeply into cross sections to discuss the heat generation patterns.

4.2.1 Temperature Plots – Parallel Sections

Figure 4.20 shows cross sections parallel to the welding direction, the welding direction is from left to right and the welding speed is 30 m min^{-1}. The results are taken from an entire run of tests previously depicted as a line of RTZs on Figure 4.18 and show the maximum temperature reached. The welding current ranges from 3000 A to 3700 A.

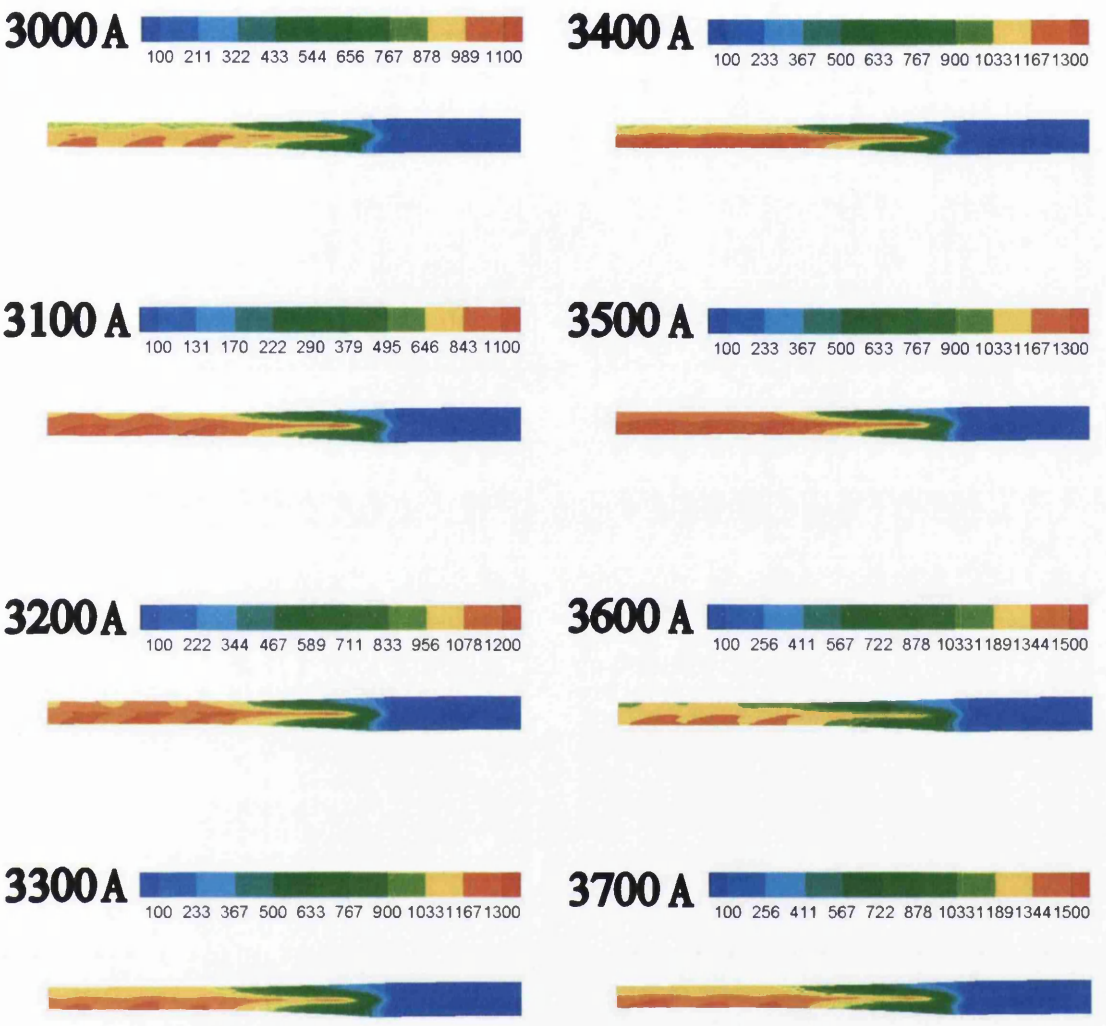

Figure 4.20: longitudinal fringe plots of maximum temperature through the centre of the overlap for eight welding currents and 30 m min^{-1}. Scale is in degree Celsius and is not the same for each current.

Immediately apparent is how the heat generation starts early on in the weld gap mainly concentrated across the interface. This is good from a theoretical point of view because this is where heat is needed for bond formation. The bond formation is thermally assisted as previously discussed and occurs under pressure from the rolling electrodes so the longer the pressure is applied to two sheets which are locally at an elevated temperature the better chance there is for a sound weld to result. One other thing worth noting is how heat generation is

predominantly towards the lower electrode from start to finish because of the higher current densities. The heat pattern for each result is similar for each process condition shown above but the absolute values reached are not; keeping the same legend levels loses the pattern.

4.2.2 Temperature Plots – Tangental Sections / Temperatures Reached During Welding

Another way to look at the maximum temperatures reached during weld formation is to section the mesh transversely to the welding direction. In Figure 4.20 the legend was changed but when the legend is kept the same and the number of levels reduced the heat patterns can be quite interesting as shown in Figure 4.21.

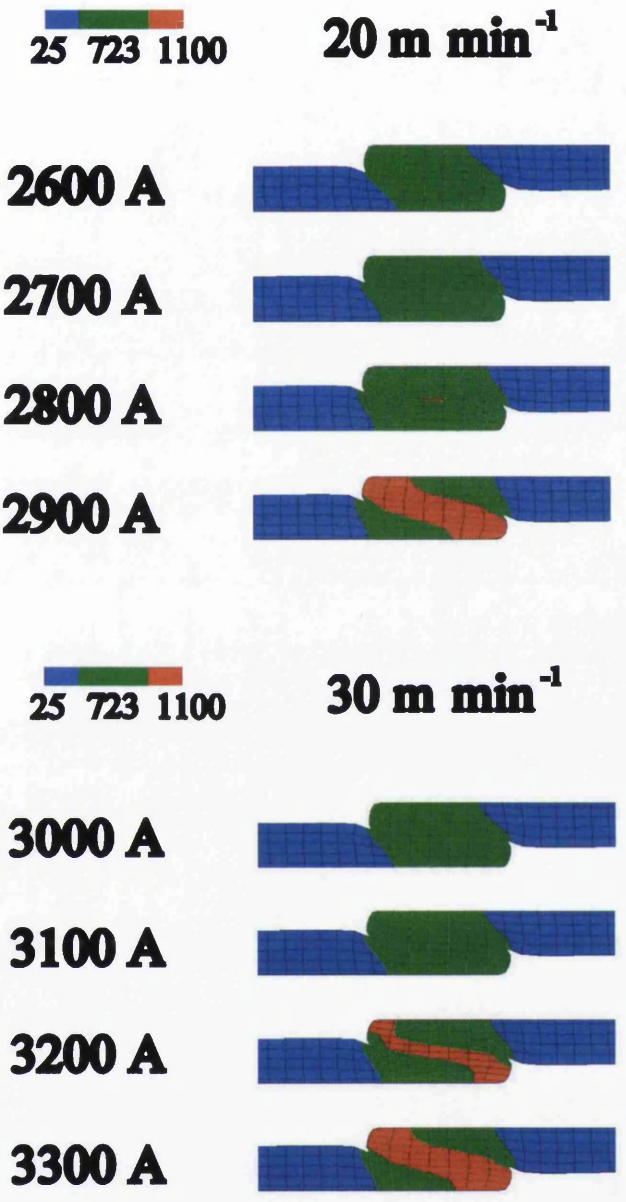
25 723 1100
20 m min-1
2600 A
2700 A
2800 A
2900 A
25 723 1100
30 m min-1
3000 A
3100 A
3200 A
3300 A

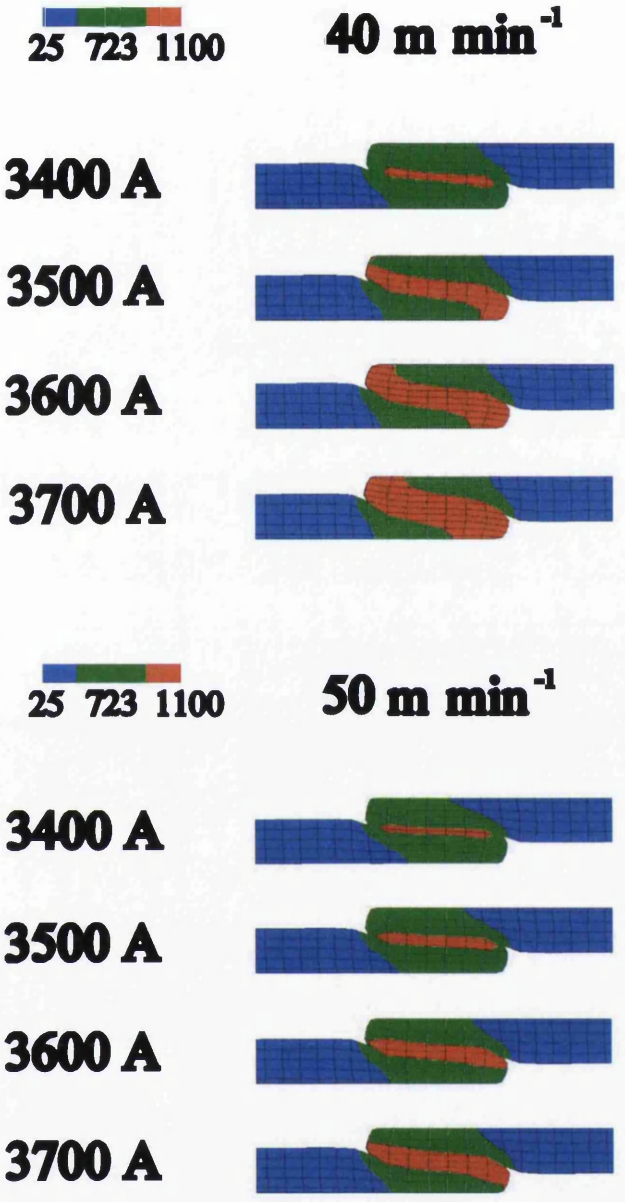

Figure 4.21: examination of the lower welding limit and temperatures reached using fringe plots of transverse cross sections. Scale is in degree Celsius.

The Ac_1 temperature from a binary iron carbon phase diagram was chosen as one level because it is necessary for harder phases such as martensite to form, and also because perhaps it is a necessary temperature to reach for sound welds. Overall the heating is most intense at the interface as can be seen in all of

the contour plots as well as extending towards the corners where the current density is numerically very high. The heating rates seen in HSRW are high as has been mentioned before and are typically of the order of 10^6 °C s^{-1}, so quite far from equilibrium. It is technically possible to calculate the phases present at such conditions but due to the high degree of complexity this analysis was deemed beyond the scope of this work. 1100°C is also plotted because the temperature is not reached in the simulations at the lower weld speeds and weld currents so this temperature appears to be critical for sound weld formation. This temperature of about 1100°C is consistent with [Davies, 1993] who mentions that the solid state welding temperature of steel is around 1200°C and also [Linnert, 1994] who states that most metals see appreciable assistance to solid state bonding when the temperature is raised above half their absolute melting temperature.

Above 723°C under equilibrium conditions plain carbon steel is austenitic and therefore in the softer FCC crystallographic configuration, but more temperature is needed to get the bond formed in the short timescales for it is not until much higher temperatures that bonding takes place. Looking at the simulation results in Figure 4.18 in conjunction with the above Figure 4.21, and remembering that the RTZ lines when performed experimentally go from the condition where no bond is formed right through to the splash condition it is possible to speculate upon the required temperatures for sound bond formation. As the welding speed is increased the 1100°C isotherm appears earlier and earlier until at 40 m min^{-1} it is present at the lowest welding current.

The appearance of the 1100°C isotherm is not consistent with the formation of sound welds, a single temperature criterion by itself is not sufficient to predict sound/unsound welds. But for many temperature driven processes, time is almost always an equally critical factor. So it can be said that higher temperatures are required for the lower limit of the welding lobe as the linear weld speed increases. This is necessary to offset the decrease in the time spent

in the weld gap and therefore the time for the bond to take place. Because the temperatures reached are higher there is a greater proportion of the material that upon cooling transforms to martensite, resulting in harder welds. Post weld formability is needed for the subsequent forming operations such as beading and seaming.

Another way to look explicitly at the temperature reached in welding is to look at the maximum temperature reached during welding graphically. Maximum temperatures seen in the whole mesh each timestep were recorded for all simulations and are depicted in Figure 4.22.

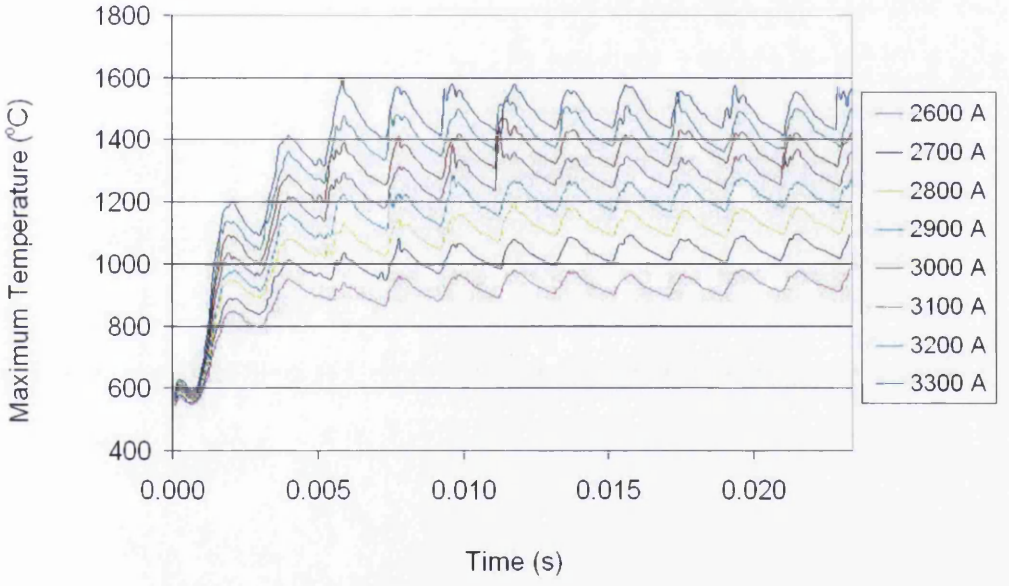

20 m per min

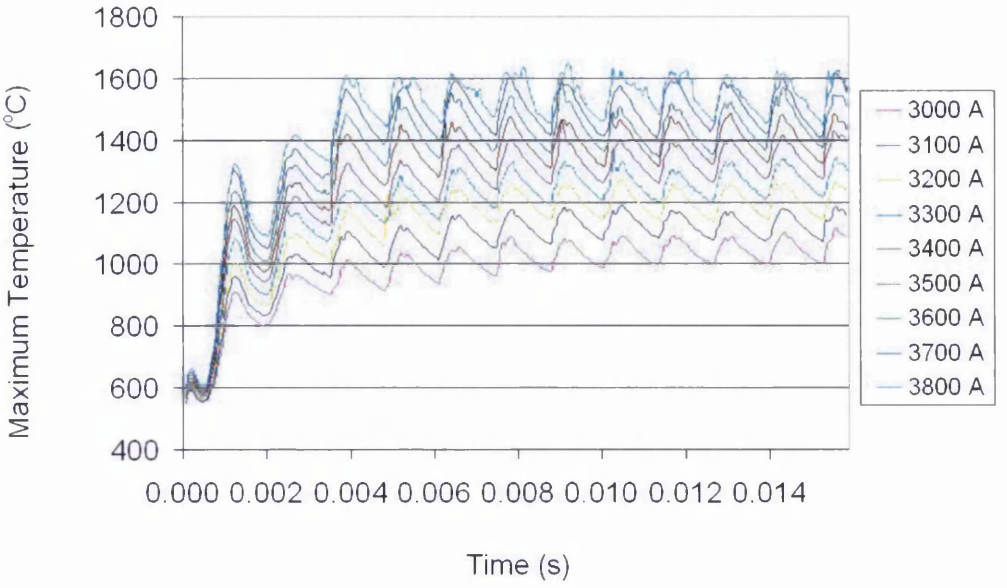

30 m per min

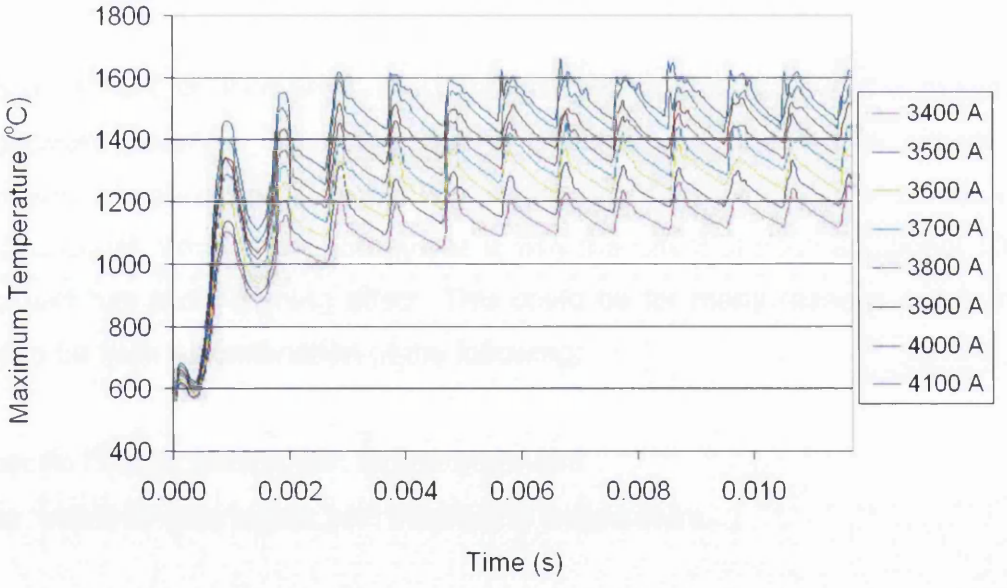

40 m per min

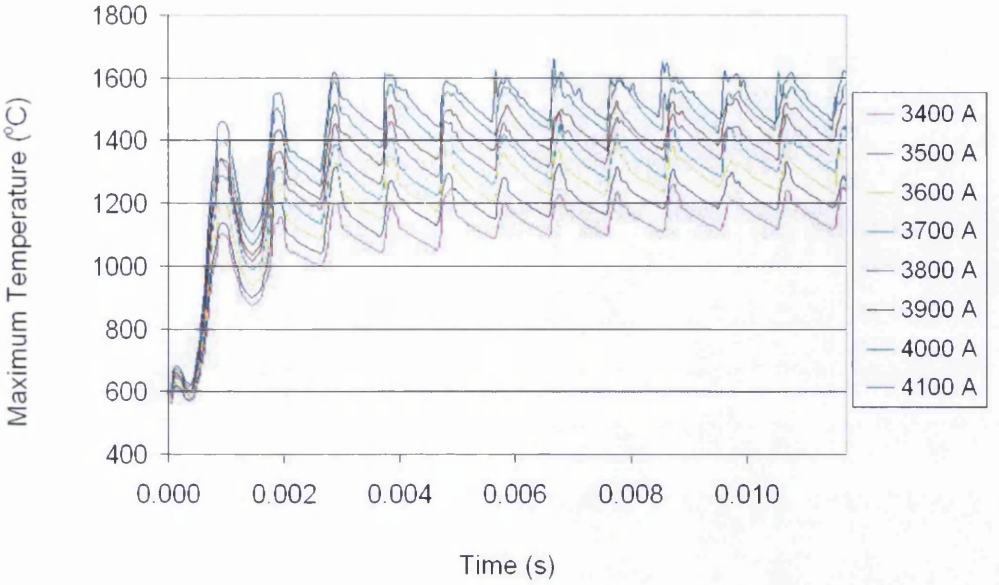

50 m per min

Figure 4.22: maximum temperature reached in the mesh against time.

As the current is increased it is immediately apparent how the maximum temperature reached each timestep is affected. As one would expect the maximum temperature is higher for higher welding currents when all else remains equal. What is not so obvious is why the effect of each additional 100 A of current has a diminishing effect. This could be for many reasons but is most likely to be from a combination of the following:

– Specific heat increases with temperature and
– The resistivity gets higher with increasing temperature.

The increase in specific heat requires that for further temperature increases to be obtained, increasing quantities of energy in the form of current must be supplied. The local increase in resistivity impedes current flow and thus the current is diverted through a wider 'path' to the surrounding volume with lower resistivity, an effect known as shunting.

The simulations at higher welding currents do not converge on a solution and are subject to very high temperature instabilities so the results are not included in this thesis. A possible explanation is because at the higher welding currents the occurrence of splash takes place and thus the material at the highest temperatures which is liquid is ejected from the weld seam, thus removing it from what is modelled as an FE mesh. This cannot be captured in the simulation because the mesh has to remain as such because of the elemental connectivity and material that may be liquid cannot be modelled to leave the mesh. Also at the higher welding currents sparks are frequently witnessed and again this phenomenon cannot be simulated by the model in its present state.

There does seem to be some variation in the maximum temperature reached with each cycle and one possible explanation for this is because of the change in contact length. What is referred to here as contact length is the length where for example the upper electrode roll is contacting the work piece. This contact length is transient as the individual nuggets show a slight indentation variance along the length so together with this there must be a change in contact length. This could be thought to be significant because with a larger contact length the heat input to the weld is caused to occur over a longer distance. Also the distance over which the weld is formed is significantly longer than the weld nugget, about 2 mm and 0.65 mm respectively. So each weld nugget, although appearances would suggest otherwise, is subjected to more than one current cycle and rarely an integer number of current cycles. This is one suggestion for the imperfect maximum temperature cycles of Figure 4.22. This is investigated later on in this section.

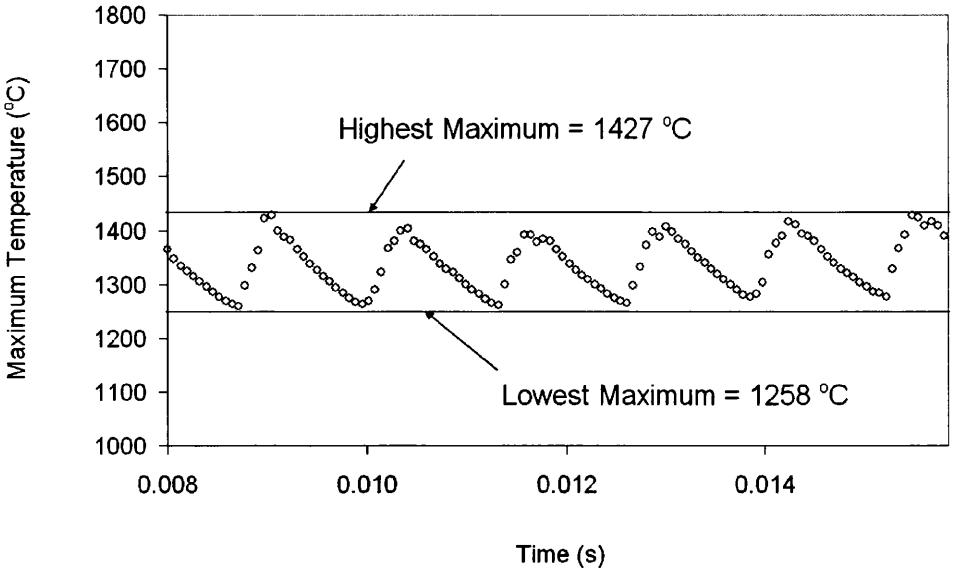

Figure 4.23: description of how the data was gathered for Figure 4.24.

To discuss more in depth the upper limit to the welding lobe the highest and lowest maximum values are scrutinised in more detail. To explain what is plotted subsequently please refer to the diagram above which shows the maximum temperatures reached in the simulation at 30 m min^{-1} and with a current of 3400 A. Figure 4.23 shows an example of the values for each simulation taken when the simulation was considered at equilibrium.

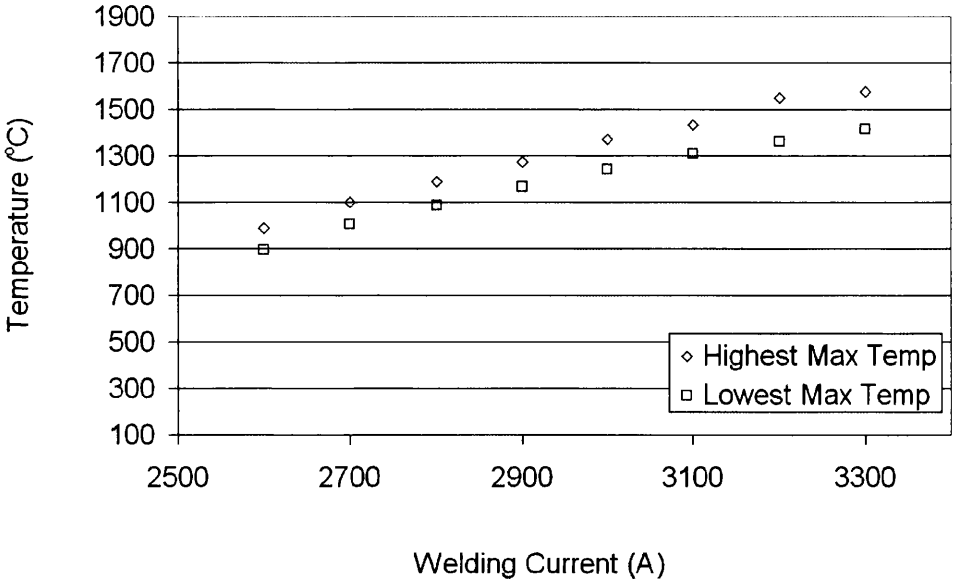

20 m per min

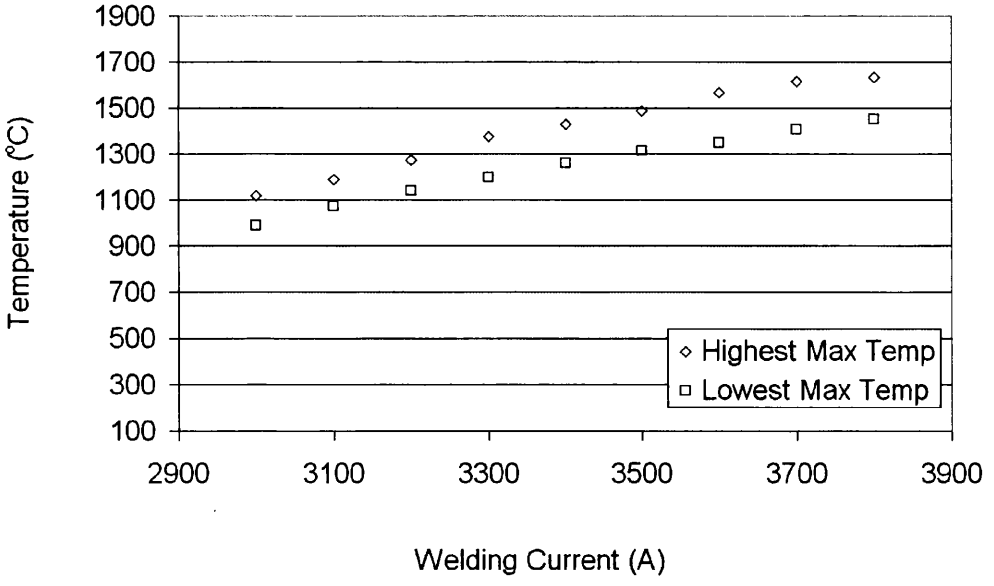

30 m per min

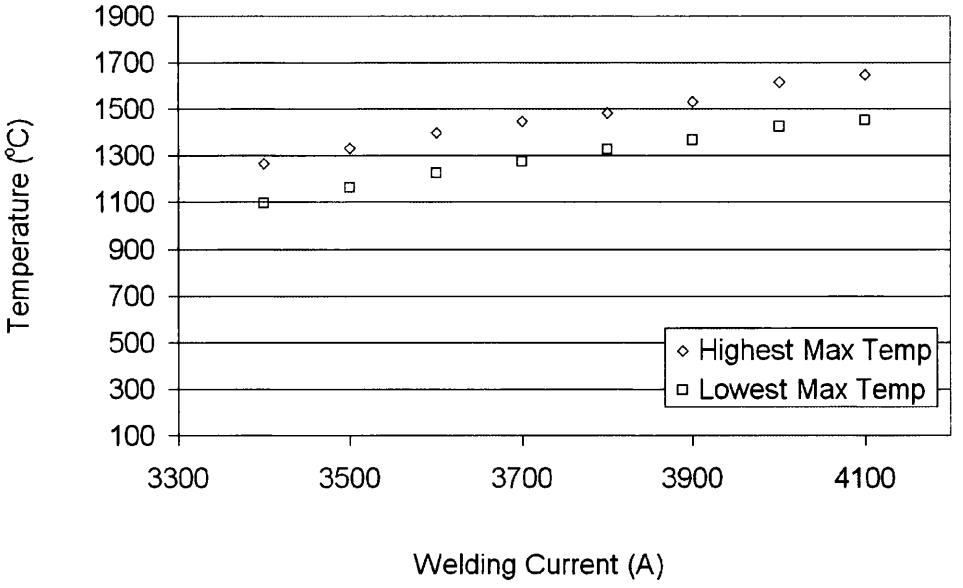

40 m per min

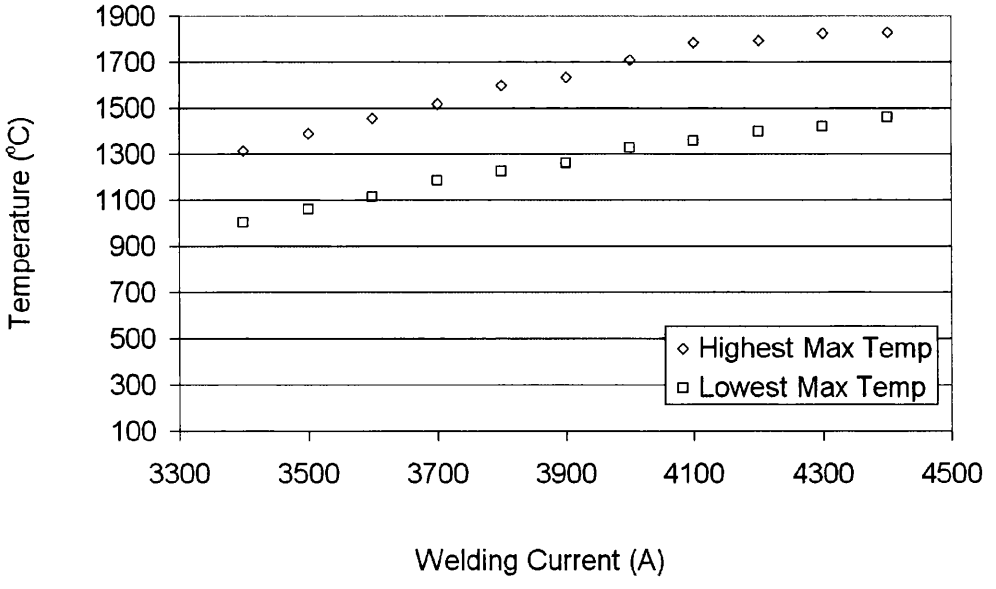

50 m per min

Figure 4.24: maximum temperatures seen in the AC cycle for four welding speeds and a range of welding currents.

The graphs show a broadly linear response to the increase in current right up to the point where the simulations become unstable. As the highest welding currents are reached for a significant time sections of the discretised continua are

above the equilibrium melting temperature of plain carbon steel. This is congruous with the appearance of splash around these temperatures. The times above the equilibrium melting temperature of plain carbon steel get longer the higher the welding current until the lowest maximum temperature is also above this temperature. At the very highest welding current for each speed this potentially could be a good method for splash prediction. However the model appears to slightly under predict the splash condition if this rationale is used and it gets increasingly more so as the welding speed gets less. The highest welding currents cannot be simulated because the model becomes unstable. An example temperature trace for an unstable weld is shown below for 20 m min^{-1} and 3400 A.

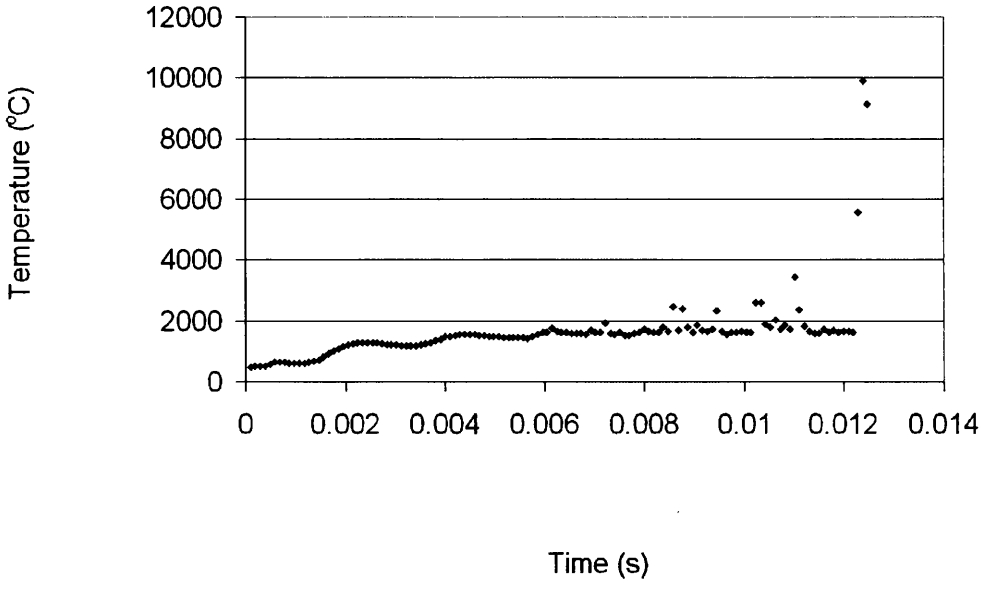

Figure 4.25: thermal instabilities of the modal at higher temperatures, maximum temperature in the mesh at each timestep for 20 m min^{-1} and 3400 A.

4.3 Results Section III – Energy and Power Considerations

One of the key advantages in FE modelling is the ability to easily plot dependent variables. One useful example is of the energy input into the weld. The energy being input into the mesh is calculated for each integration point to take account of the Joule heating effect, this energy can then be summed up for each element and then the whole mesh.

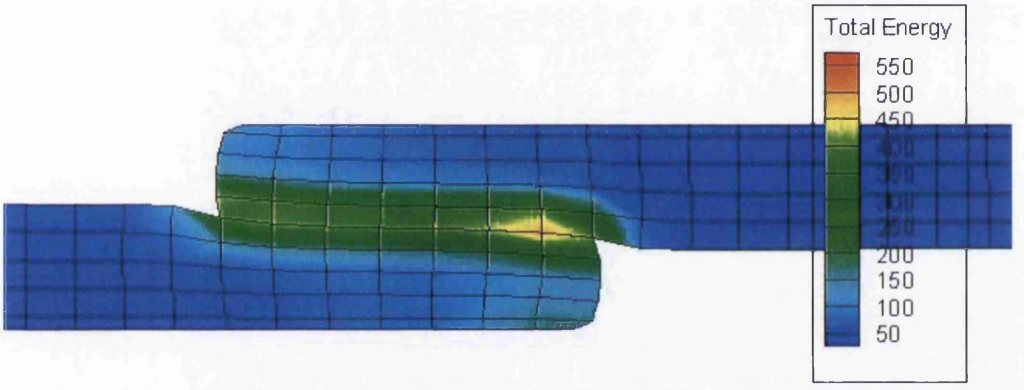

Figure 4.26: total energy input into the mesh through the Joule effect. Scale is J m^{-3}.

This transverse section along the welding direction shows a typical distribution of the total energy inputted into the mesh as it passes between the rolls, the simulation is for 20 m min^{-1} and 3100 A. It is interesting and consistent with the formation of splash. Splash is always seen on the inner side of the can where the current density is at its highest. Energy is being concentrated in a small volume of material and causes rapid melting and when this liquid is not contained it is forced out from the pressure exerted by the electrodes. More quantitative results are possible when a graph is plotted to explore the upper welding limit further. This has been performed in Figure 4.27 showing the total energy input into the mesh per metre.

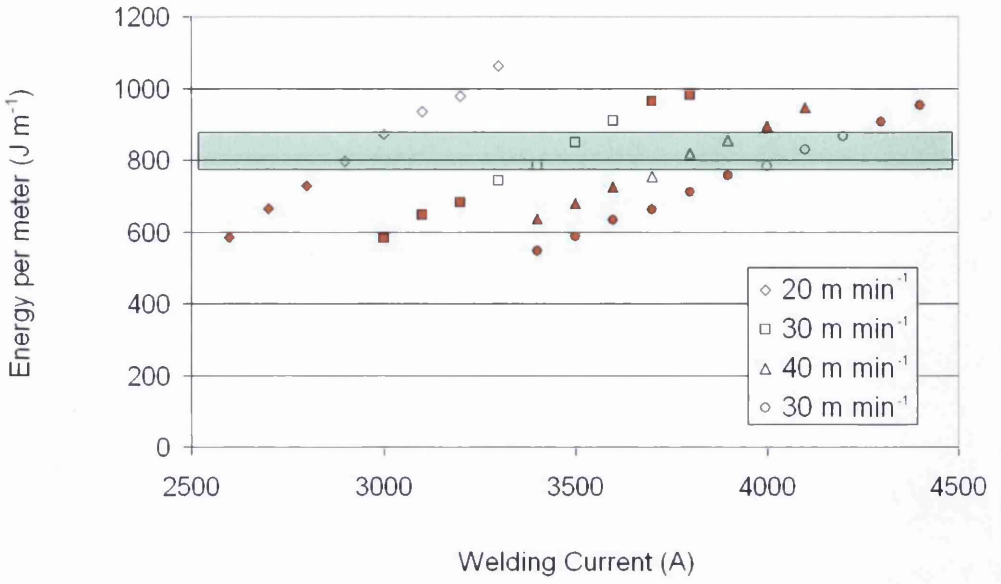

Figure 4.27: simulation results of energy per meter supplied to the mesh for the 4 welding speeds in the experimental data.

At first glimpse this graph offers little extra with respect to the condition of a weld and the pattern is identical to the RTZ lines highlighting the extent to which the two are linked. As one would expect, a critical amount of energy supplied to a weld per metre is needed to raise the temperature to the necessary level for solid state welding to take place in the available time. When the *bad* welds are highlighted it leaves a horizontal band where the *good* weld settings are. The data shown in Table 4.2 was used but because the values for the upper and lower limit of the welding range are for four nugget pitches an average was chosen. This leads to difficulties for the data at 20 m min^{-1} in so far that the large spread in these values for the upper limit means that it breaks the trend and this is why the 20 m min^{-1} data has no upper weld limit marked. Another way of producing more valuable data is to look at the power input.

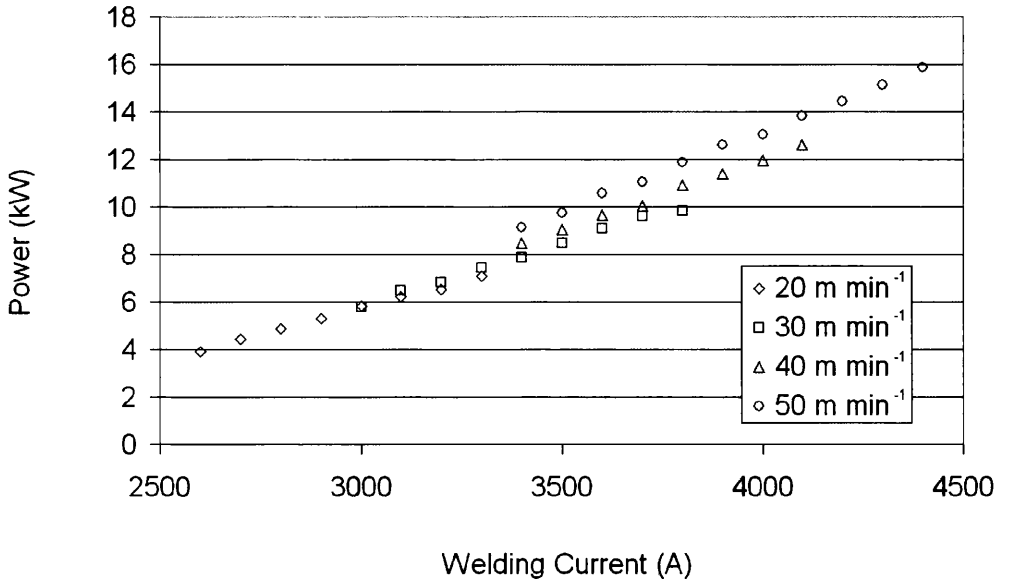

Figure 4.28: simulation results of power supplied to the mesh for the 4 welding speeds in the experimental data.

Figure 4.28 shows the power input against welding current, the power is the total power being supplied to the mesh. Overall the trend is that the individual welding speed/current combination lies close together in a single band of results. All four welding speeds do lie on a similar line however there are small increases in the power input with increase in speed. The reason for this could be the higher contact resistance applied for each subsequent speed increase but the lines are now significantly closer to one another than the energy applied per metre plot.

As a final output regarding energy an attempt is made to investigate the occurrence of slight variations in the highest maximum temperature as this goes through a cycle corresponding to the AC cycle. It is the change in contact length that has been put forward as a cause of variation in these temperatures and possibly this could be because of the total energy supplied in each slice of the mesh.

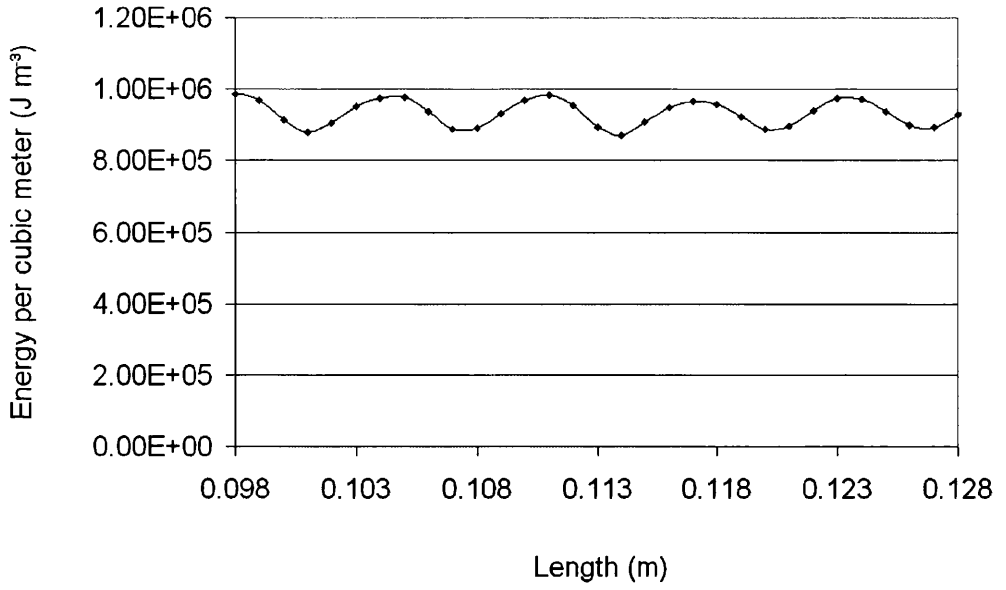

Figure 4.29: energy per cubic meter input into each plain of nodes after they have been all the way through the weld gap.

The results are from the simulation of 20 m min^{-1} and 3100 A. The above Figure 4.29 shows that this is not a possible cause of the temperature instabilities because of the consistency of the cycle.

4.4 Results Section IV – Welding Conditions

Another way to extract information not garnered experimentally is to look at the conditions present for a typical node, as opposed to the methods presented above that look at the mesh as a whole. The following plots are produced by looking at the conditions experienced by one node that lies at the centre of the interface of the two sheets being welded and is again taken from the simulation of 20 m min^{-1} and 3100 A.

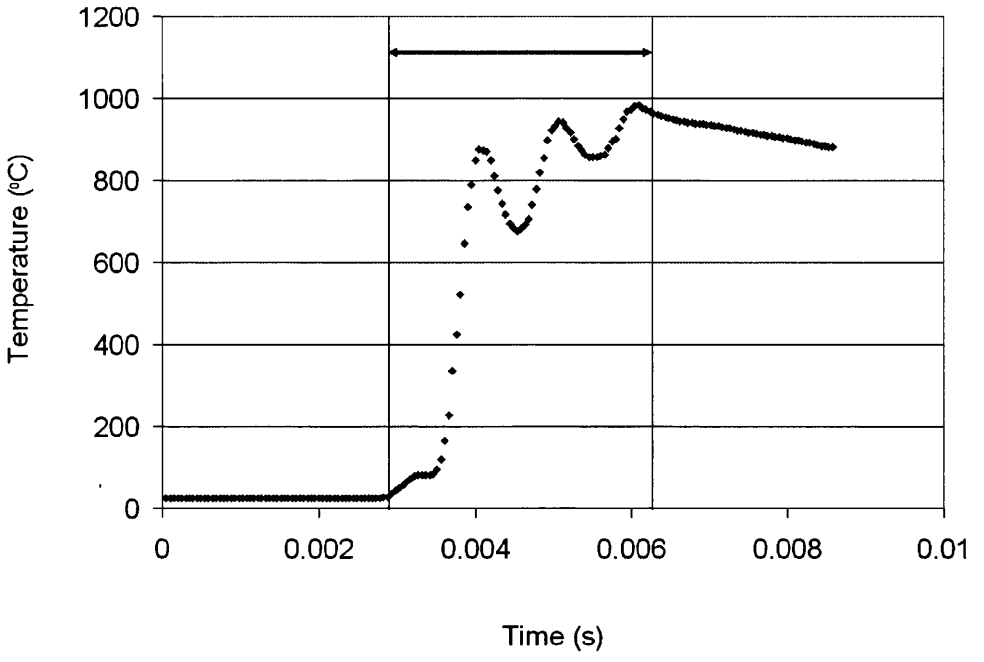

a)

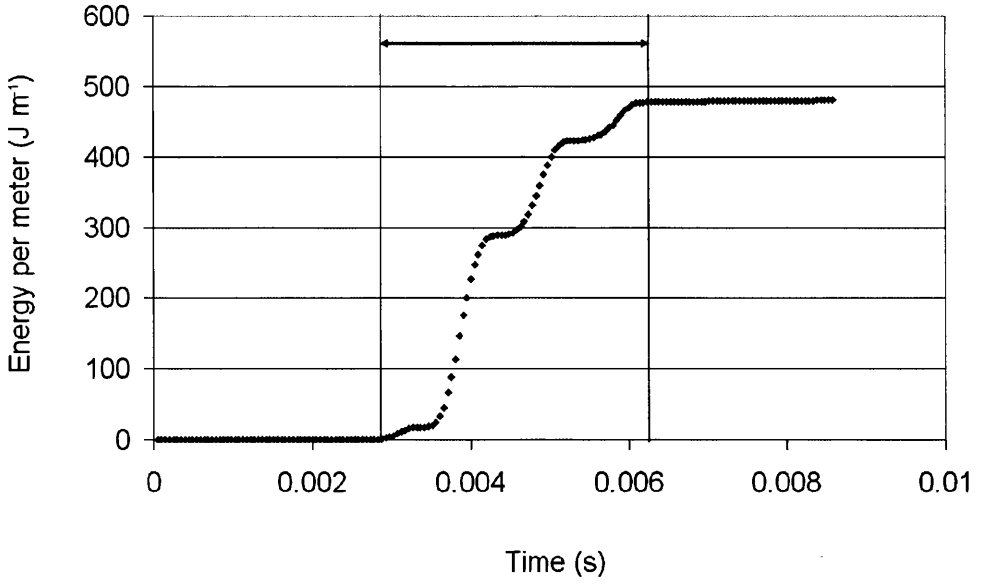

b)

Figure 4.30: temperature, a), and energy per meter, b), seen at a *tracer* nodal point that passes through the weld gap.

These two graphs in Figure 4.30 offer previously unknown information showing what the material is subjected to as it passes through the weld gap. It is clear

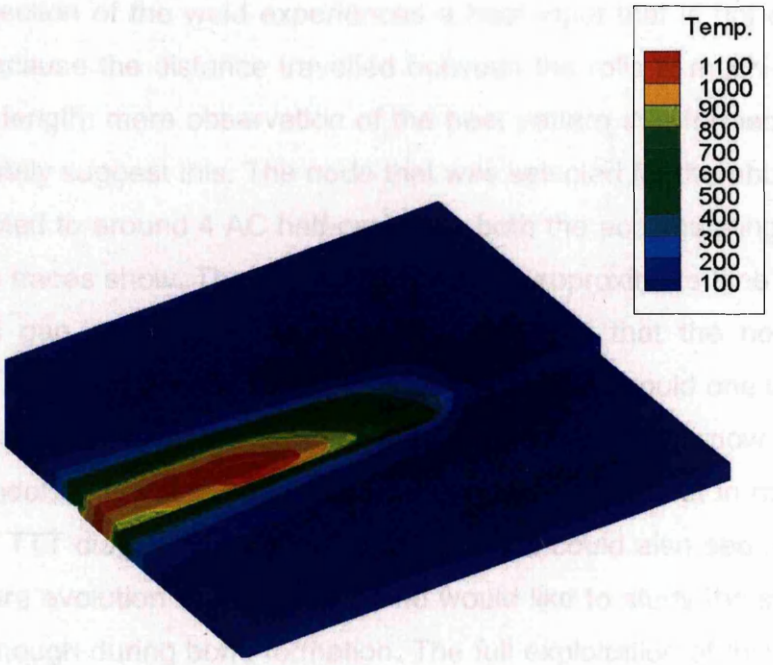

Figure 4.31: temperature of the mesh at a stable cyclical state. Scale is in degree Celsius. 30 m min^{-1} and 3400 A.

Before the weld has cooled down the von Mises stress fringe plot is given in Figure 4.32 and is due to the applied loads to the mesh by the upper and lower electrodes. The stress field is noticeably greater toward the weld overlap at the front of the contact patch due to these applied loads as well as stress arising from thermal expansion effects. The stress field is also higher just outside the overlap as the material passes though the weld gap, the overlap here being at a higher temperature and thus reducing the mechanical properties.

how each section of the weld experiences a heat input that is not equal to one AC cycle because the distance travelled between the rolls is much greater than one nugget length: mere observation of the heat pattern in a formed weld would not immediately suggest this. The node that was selected for the above plots has been subjected to around 4 AC half-cycles as both the accumulating energy and temperature traces show. The arrow highlights the approximate time that is spent in the weld gap and this is approximately the time that the node is under influence of the welding load. This data is of great value should one want to know the formation sequence of a typical weld as the conditions can now be extracted from the model. This information could be used to great effect in microstructure prediction if TTT diagrams were called upon and it could also see application in microstructure evolution studies where one would like to study the steps that the weld goes though during bond formation. The full exploitation of this data though is beyond the scope of this thesis.

4.5 Results Section V – Residual Stress

The model has the ability to simulate the weld cooling down to room temperature and to calculate the stress field enabling the calculation of residual stress fields. Residual stress fields could cause problems with post weld formability or even aid stress corrosion cracking. Figure 4.31 shows the transient temperature field once the simulation has reached a stable oscillatory state; this fringe plot displays the high temperature gradients. This simulation was run for a weld speed of 30m min^{-1} and 3400 A.

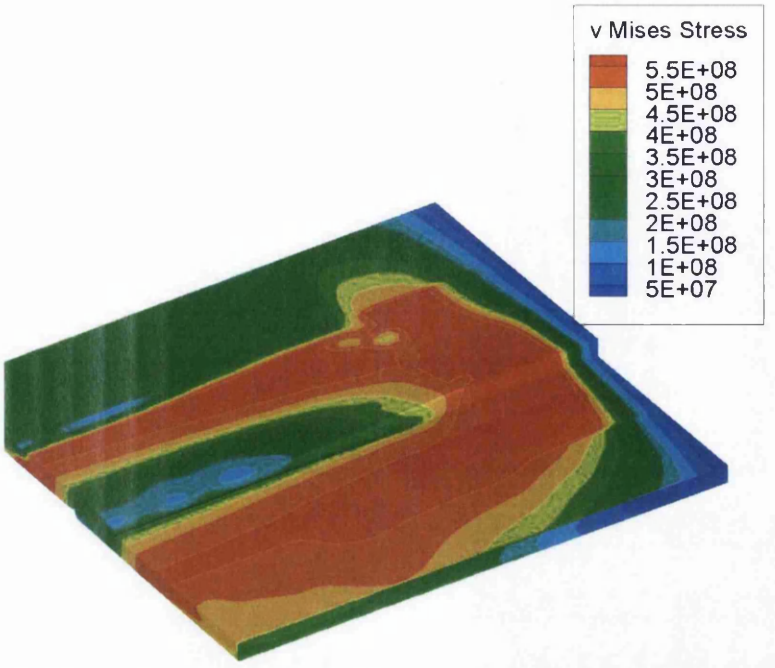

Figure 4.32: von Mises stress at stable cyclical state before cool down is simulated. Scale is Pascals.

In an attempt to investigate likely residual stress patterns after cooling the situation in Figure 4.32 was allowed to cool with no further applied load or electrical current. The result is Figure 4.33 showing much smaller maximum stress levels. In this cooling simulation the stress fields in the vicinity of the weld decay to very small levels, from the previous state of stresses approaching the yield stress at the relevant elevated temperature. The higher stresses are located at regions away from the weld. The work piece is very thin and can rapidly cool via heat transfer to the atmosphere. Not only this but the region of highest temperature can swiftly lose heat via conduction to neighbouring cooler areas and the stresses arising from the thermal contraction of the weld region are easily accommodated by these larger regions that are still at an elevated temperature. These larger regions of elevated temperatures still therefore have significantly lower yield stresses and can take up the deformations resultant of the very high temperature gradients cooling down and causing thermal contraction. From this result, in stark contrast to spot welding processes, it appears that residual stresses near the weld are not a cause for concern in

HSRW welds. Validation by [Price, 2008] was performed with neutron diffraction, but this experimental method was unavailable for this project.

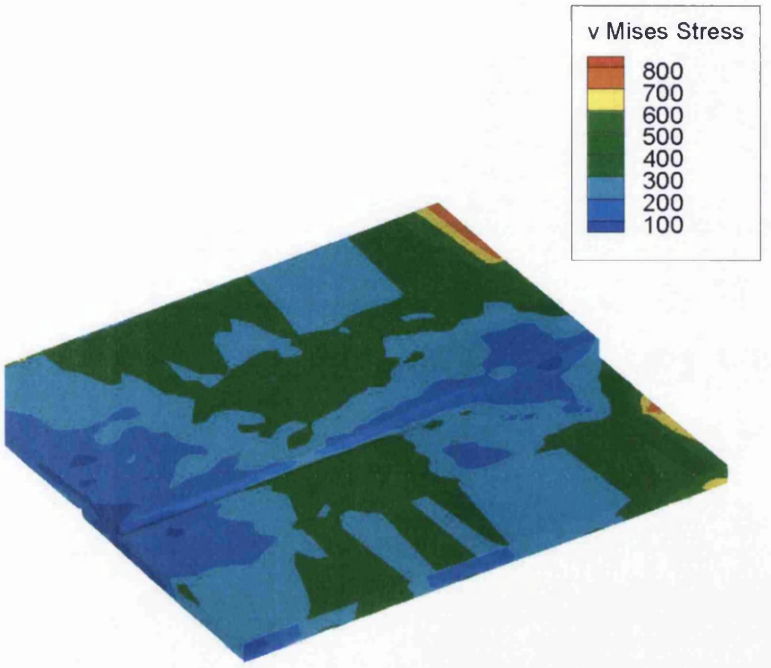

Figure 4.33: von Mises stress after cool down is simulated. Scale is Pascals.

5.0 Discussion and Evaluation

Before any numerical experiments were performed with this model of High Speed Resistance Welding the necessary steps to verify and validate the model were taken. Qualitatively the results agree to what one would intuitively expect to be happening when one considers the post weld microstructures. The longitudinal and transverse sections of the mesh look very close because of the high heat generation at the interface of the two tinplate sheets to be welded. The final step in the calculation is the transient temperature field and the model is further verified by looking at the contacting areas, voltage field and current density which then results in the said temperature field evolving. The outputs from the model such as maximum temperature, indentation and so on all follow a trend governed by the AC cycle and reach an oscillating equilibrium.

Comparison of longitudinal sections of the mesh rendered with maximum temperature and longitudinal weld micrographs shows good agreement where the heat pattern curves down to the lower electrode. The lower electrode causes this effect because higher current densities and shorter contact lengths with the electrode simultaneously provide more heat and less heat removal in this region of the weld. This heating pattern appears to have a close resemblance to the cavities witnessed with the comma type defect. This begs one to ask the question why a smaller lower electrode is chosen when it results in an uneven weld. There is a sensible answer to this question and it is because using equally sized electrodes is not the only quality issue to address when producing three piece can bodies. The overlap is also critical and much effort is gone to by the manufacturer of these machines to control this resulting in relatively large Diablo Rolls to hold the tinplate precisely in place until it is welded and, the upper electrode has to have a radius large enough to be clear of this mechanism. The lower electrode is smaller because it has to fit inside the can body.

After verification validation needs to be performed. This is good practice when one wishes to quantitatively analyse the numerical output from the model. Choosing a measurement that can be easily be taken with a high degree of accuracy both experimentally and numerically was seen as key to validating the model. Validation was chosen to be by matching the experimental and numerical Re-melted Tin Zones because it meets well the criteria set above. Validation was complete after a stage of fine tuning the model by slight changes in the contact/interface resistance assumptions, a process that took more than one year. The problem initially was that nothing appeared to change the gradient of the RTZ lines as consistently as the contact/interface resistance. The bulk multiplier used to model the effect of the liquid tin between the two sheets can be increased and decreased as an assumption but this only moved the RTZ line in a vertical direction. Making the bulk multiplier vary with distance produced results that where in very close agreement with the experimental data and so offered an opportunity to go on to evaluate data that is not available experimentally. The contact resistance is shown here to be a very sensitive parameter. It is also very difficult to model because it is such a small amount of tin that is electrodeposited onto the steel substrate and capturing this fine coating of tin numerically is very difficult.

The use of the RTZ as a successful and robust method for model validation is clear. The subtle differences in each weld are easily measured in both the model and the experimental tests. The writing of an additional piece of code using the Finite Difference method allowed very fast cool down simulations to be made with a high degree of accuracy.

Also worth mentioning is how the model becomes unstable when a significant proportion of the mesh is at a temperature above the equilibrium melting point of steel. [Murakawa, 2001] and [Ferrasse, 1998] both talked about instabilities as soon as melting took place and it is interesting to consider why. With reference to the plot of maximum temperatures against time in Figure 4.22, one can observe

the slight increase in the amplitude of the equilibrium cycle of the maximum temperature as the welding current is increased, but the model goes through a transition from stable to completely unstable within an increase of only 100 A. One could speculate that this could coincide with the occurrence of splash and the reason for the instability is because the model simply cannot simulate this happening. The model can of course produce limitless temperatures but splash is when molten metal is ejected from the weld seam; the Finite Element method offers no way to take count of this when consistency of volume and mesh connectivity needs to remain satisfied, and because the method models solid material not liquid. Along the same lines as this is the appearance of sparks at about the same welding conditions as splash and again the reason for instability could be because this cannot happen in the model so energy that would be removed from the mesh is retained resulting in ever higher temperatures. The combination of these two phenomena taking place could be providing the instability also.

An attempt to find a criterion for the lower weld limit is sought in the model results and at first attention is given to the temperatures in the weld for the first few simulations at the lower welding current range and 20/30/40/50 m min^{-1}. This method does not provide a conclusive way to predict when the lower limit of the welding lobe is reached because there is an increase in the temperatures with the welding speed. This does however make sense and when the reduced time for welding is taken into account an increase in temperature would be expected for such a thermally activated/assisted process.

The upper limit was studied with a comparable method using maximum temperature plots and due to the instabilities encountered at the highest currents it could not be completely evaluated. This instability did however take place at comparable temperatures for each weld speed. This was most notable for the lower maximum temperature of the equilibrium cycle at each welding speed because the highest stable welding current corresponds to a temperature just

above the equilibrium liquidus temperature. So although the model is reasonably consistent there is a definite under prediction of the upper welding limit. The difficulty in predicting the upper and lower weld limits led to the further investigation using energy and power input that was calculated and output from the model.

Looking at the energy and associated power input into the mesh is a case of simply outputting the energy as it is calculated each timestep and is especially useful when the contour maps of its distribution can be rendered in a post processor. When this is done the highest energy input per cubic meter is observed at the interface towards the lower electrode, just where one would expect splash to be emanating from. The energy per meter plot is very closely correlated with the RTZ data used in the validation step showing how the RTZ, though only a simply measured surface property, is actually linked to something more sophisticated.

When the results outside of the welding range are highlighted there is a distinctive band across the energy per meter plot, indicating that there is a critical level of energy input to create a sound weld. Only the 20 m min^{-1} weld speed misses this band, but only at the upper limit, so aiming for the middle of this safe band should still yield good results. One reason to mitigate this shortcoming is the large variation seen in the upper welding limit: it is between 3150 A and 3600 A. 3150 A would fit the rule very well. Maybe the data was produced under slightly different circumstances unbeknown to the author and so this is then down to experimental error. Re-examination might be revealing if this were the case. It does appear that a criterion for a good weld has been discovered, but it was not tested outside of the test matrix. Further work seems necessary to add extra foundation to this criterion.

The power input plot also looks interesting because all the points lie along a distinct band with only small increments at each of the weld speeds. Because of

this linear feature maybe with further analysis this could lead to a criterion for a better sound weld formation, but ultimately this is beyond the scope of this work.

Welding conditions were looked at for what would be a typical infinitesimal point at the interface of the two sheets being passed through the weld gap. These conditions, which are impossible to measure experimentally, give greater aid to the scientific understanding of HSRW bond formation. Looking at a weld seam and the heat pattern on the surface or even at a polished and etched microstructure one observes the heat pattern corresponding to the nugget length even though the typical interface section is clearly subjected to much more than one AC cycle. When the maximum temperature is rendered in a post processor for a longitudinal weld section the effect is the same: heat patterns that fluctuate with the nugget pitch. This goes to show how the bonding together of the two sheets and therefore the disappearance of the interface takes place at different conditions to what the bulk material experiences. This is illustrated further when one looks at the longitudinal maximum temperature contour plots and pays particular attention to the way that heating at the interface is at first concentrated on the interface. Because the welding process is so obviously thermally activated and linked to tin removal and grain growth these conditions graphs highlight much more than was previously known about the process.

The final exploitation of the model was residual stress prediction. It was thought that this should be investigated due to possible concerns with weld formability when seaming. This analysis provided an insight into a phenomenon that is hard to measure experimentally. Incidentally the residual stress field was shown as being insignificant because it drops away to very small levels. The thermal stresses encountered when cooling down are alleviated by the high temperature and therefore low yield strength material. Possibly a more significant effect would be martensite formation as the thin sheet cools down from high temperatures in a short time period, but the model does not take this into account.

5.1 Limitations of The Model

The model developed in this thesis is more extensive than those reported in the literature and presents a novel way to analyse the problem, but the model is not without its weaknesses for three reasons. The first reason is that present limitations in affordable computing power always require that simplifications have to be made when constructing numerical models. Secondly this is compounded by the fact that experimental results rarely exist for material parameters that would be needed even if these simplifications would not have been made. Finally there is a time constraint to contend with.

The first omission of the model is that it is only two sheets that are simulated rather than one sheet rolled over so the two opposite edges are then welded to form a cylinder. This does not seem such an important omission but there must be a significant loss of current through the body as well as the machine so applied welding currents are not what passes through the overlap, reducing accuracy of results.

At present there is no way to look explicitly at the bond formation because the model has had to approximate only the steady state situation of the model. Ideally a complete model would allow one to predict the occurrence of a sound weld far from the range of the process conditions verified against but following from the constraints mentioned above this was not possible. In reality an increase in bond strength would be expected when one of the following was increased:

– Weld time
– Thickness reduction
– Temperature
– Pressure

A much more elaborate model would be required to quantify bond formation and be dependent on all of the above. In reality this is the melting of the layer of metallic and intermetallic tin, removal of liquid tin, oxide dissolution, grain nucleation and grown as well as metallic bond formation so to do this in FE would be some challenge. Another method that could be coupled to this analysis may be an answer. Also the model does not look at any microstructural evolution and tying this in with the bond formation would lead to a very interesting model. Indeed the knowledge of phases would also be useful for the stress analysis when deciding on material parameters.

5.2 Suggestions For Further Work

The obvious direction for further research would be to increase the detail of the model to look at bond formation. The first on the list to be elaborated on is the treatment of the liquid tin layer to quantify its behaviour, possibly by using Computational Fluid Dynamics and, remembering that the tin layer is multi phase. If this was to be better quantified then maybe an almost empirical equation could be used to relate process conditions to the likely success of a weld. Also, possibly there could be a way to prevent the model from becoming unstable at the highest currents to allow this area of the welding lobe to be researched. With reference to the graphs on welding conditions in Figure 4.30 it would be useful to part form some welds to look at the evolution of the weld as it passes through the weld gap. This was to some extent performed by [Blom, 2006] but it relied on just lowering the weld current so the weld didn't form, looking at part formed Gleeble specimens could be one way of looking at this with a little more detail.

6.0 CONCLUSION

1. The model was taken through a process of verification to check that it was producing results that effectively simulated reality such as producing temperature fringe plots that showed similar patterns to micrographs of polished and etched post weld cross sections. The model reached a stable oscillatory state where outputs of deformation and temperature varied between consistent maximums and minimums every half cycle of the AC.

2. Before any in depth exploitation of the model was carried out a validation stage was necessary. A robust measurement was chosen to be measured experimentally and numerically – the Re-melted Tin Zone. The difference in the solidification conditions for the tin after welding in comparison to the flow melting stage in tinplate production gives rise to a surface with different reflectivity which can be measured on an optical microscope Vernier scale.

3. The experimental data was provided by Corus RD&T in IJmuiden; a test matrix of four speeds and welding currents that ranged from creating welds that were unwelded (because of a lack of heat input) right up to producing welds that showed signs of splash (because of too much heat input).

4. Numerically this was achieved by using a Finite Difference algorithm to cool down the previously simulated High Speed Resistance Weld from its equilibrium condition. The 3D Finite Element mesh is transferred onto a much finer Finite Difference mesh in 2D to allow for a higher degree of accuracy.

5. Many simulations were carried out over more than a year of model development to match these numerical results with the experimental results. Following this it was concluded that the highest sensitivity in the model by far was to the contact resistance.

6. Contact resistance is frequently described in the literature as being important with regard to the weldability of tinplated steel, but contact resistance itself is used to describe two solid objects in contact. Because tinplated steel has a fine layer of low melting point tin on the surface there is no contact resistance, only a higher resistivity because of the high resistivity of liquid tin and iron-tin intermetallics as well as surface oxides.

7. The difficulty with modelling this tin layer is because it is on a significantly smaller length scale than the whole problem so it cannot be meshed and taken into account in the same way as the rest of the problem and so it was approximated as a boundary condition (higher resistivity). The flowing away of the liquid tin, since very little is left in a formed seam weld, from the weld overlap was approximated and excellent results were attained.

8. After the validation of the model was complete the author used the model to look into the output files in more detail to first look at the lower welding limit at the four weld speeds tested. There was no consistency of the temperatures reached at the lower welding limit as time is also a critical influence in the formation of High Speed Resistance Seam Welds.

9. A similar attempt was performed to look at the upper welding limit by plotting out graphs of maximum temperatures. It was noticed that as the welding current was increased the increase in the temperature became less and less. This was put down to the increase in resistivity with temperature and also specific heat capacity increase. At just above the highest welding currents simulated the model became unstable. Other authors have reported the same when the temperatures get significantly above the melting temperature. In this model it was when the lowest cyclically stable maximum temperature reached above the equilibrium melting point of steel. It was concluded that this instability was the result of the model not being able to deal with what would be happening in

reality; splash and sparking. Essentially the removal of energy from the system by splash and sparking was held in the mesh and produced the instabilities.

10. Energy per meter input into the mesh was also studied, in the hope of revealing more about the upper and lower welding limit. Interestingly a fringe plot of this energy supplied revealed how the highest energy input into the mesh was at the same position as where splash emanates from – the inside of the can body. The plot up of energy per meter and welding current revealed not much more than the Re-melted Tin Zone plot, in fact they were identical; highlighting what the Re-melted Tin Zone is linked to.

11. A criterion for the formation of a good weld was found in the energy per meter graph. When all the welds outside the welding range were highlighted they left a horizontal band where all the good welds were produced.

12. The power input was looked at against welding current but even though the results all lied on the same band, the speed factor cannot be removed so there is not a way to predict exactly a welding limit without taking into account the diminishing time for welding as speed is increased.

13. The model was used to look at the typical conditions experienced by the material as it passes through the weld gap. This data is impossible to gather experimentally and so demonstrated the power of this numerical model, and its usefulness to aid further research. Finally residual stress was calculated for a cooling down weld and the results show that the effective von Mises residual stress field drops to a very small level and is not considered a concern for post weld formability.

7.0 ACKNOWLEDGEMENTS

The author would like to thank both Corus Packaging Plus and EPSRC for their financial support. Big thanks first of all go to Steve Brown for all the help, insight and encouragement during the past 7 years, without whom this work would not have been possible. The author would also like to thank all the people in Corus who have helped out and made the last 4 years including: Erik Elzinga, Ann Brash and Kees-Jan Verstraten. Thanks to my family for their support throughout university and especially to my mum for pointing out Materials Science and Engineering to read at university, a subject that is one of few I believe I could have managed to stay interested in all these years!

8.0 REFERENCES

Adam L & Ponthot J-P, "A Coupled Thermo-viscoplastic Formulation at Finite Strains for The Numerical Simulation of Superplastic Forming", Journal of Materials Processing Technology, vol. 139, 2003, p 514-520.

Allen W.J., Begeman M.L., "Seam Welding Galvanised Steel", Welding Research Supplement, April 1958, p138s-143s.

Argyris J.H., Scharpf D.W., "Methods of Elastoplastic Analysis", Symposium on Finite Element Techniques at The Institut Fur Statik und Dynamik Der Luft – und Raumfahrtkonstruktionen, University of Stuttgart, Germany, June 10-12, 1969.

Asano H., Higashi M., Higuchi S., Ichikawa M. "Coated Sheet Steels for Welded Cans", Nippon Steel Technical Report No. 25, April 1985, p47-54.

Basarab-Horwath I., "A Resistance Seam Weld Monitor Evaluated", Metal Construction, September 1986, p544-549.

Basarab-Horwath I., "Resistance Change During Seam Weld Nugget Formation", Joining and Materials, November 1988, p235-237.

Beaverstock R., "S3119 General FE Support – Mash Seam Welding", British Steel Internal Document, January 2000.

Begeman M.L., Walker G.C., "Seam Welding Low Carbon Steel", Welding Research Supplement, March 1955, p123s-131s.

Bellotte E.J., Lheureux G.E., "The Principles of Seam Welding", Welding and Metal Fabrication, October 1964, p393-397.

Blom A.H., "Tin Layer Behaviour and Microstructural Development during High Speed Mash Seam Welding of Tinplate Packaging Steels", Masters Thesis: Technical University of Delft, 2006.

Boyd A.J., "Mathematical Model of Weld Cooling", Metal Box Technical Record, Document No. T814034, 28/01/81.

Boyd A.J., "Geometrical Aspects of Soudronic Weld Formation", Metal Box Technical Record, Document No. TR10046050, 13/04/81.

Brifcani M., "Modelling of D.C. Resistance Welding", Crown Technology Internal Document, January 1994.

Brick R.M., "Hot Roll Bonding of Steel", Welding Research Supplement, September 1970, p440s-444s.

Brodkey R.S., The Phenomena of fluid Motions, Brodkey Publishing, Ohio, 2004.

Brown S.G.R. and Suthar B.S., "Modelling the Effects of Process Variables on Thermal Behaviour During High Speed Resistance Welding of Tinplate", Materials Science and Technology, vol. 20, Dec 2004, p1585-1589.

Brown S.G.R. and Suthar B.S., "An FE Computer Model to Investigate the Effects of Varying A.C. Frequency and Strip Speed During High Speed Resistance Seam Welding of Tinplate", Computer Aided Optimum Design in Engineering IX, Eds. Hernandez S. and Brebbia C.A., WIT Press, Southampton, 2005, p431-440.

Callister W.D., "Fundamentals of Materials Science and Engineering", Wiley & Sons, New York, 2001.

Chakrabarty J, "Theory of Plasticity", McGraw-Hill, New York, 1987.

Chatterjee K.L., Lavery R.C., Williams N.T., "High Speed Seam Welding of Tinplate Using the 150 Hz Soudronic Process", British Steel Research Communication, Report 311D, March 1971.

Chen J., Young B., "Design of High Strength Steel Columns at Elevated Temperatures", Journal of Constructional Steel Research, vol. 64, 2008, p689-703.

Church F.L. (ed.), "Laser Welding Proves Its Worth in Can Manufacturing", Modern Metals, October 1986, p104-113.

Cooper M.G., Mikic B.B., Yovanovich M.M., "Thermal Contact Conductance", International Journal of Heat and Mass Transfer, vol. 12, 1969, p279-300.

Cunningham A & Begeman ML, "A Fundamental Study of Projection Welding using High Speed Photography", Welding Journal, vol. 44, iss. 8, 1965, p381-s to 384-s

Davies A.C., "The Science and Practice of Welding", Vol. II, Cambridge University press, UK, 1993.

Deng D., Murakawa H., "Finite Element Analysis of Temperature Field, Microstructure and Residual Stress in Multi Pass Butt-Welded 2.25Cr-1Mo Steel Pipe", Computational Materials Science, 2008, Article In Press: doi:10.1016/j.commatsci.2008.01.025

Desai C.S., "Introduction to the Finite Element Method", Van Nostrand Reinhold, New York, 1972.

Dieter GE, Mechanical Metallurgy, SI Metric Edition, McGraw-Hill, London, 1988.

Eizadjou M., Manesh H.D., Janghorban K., "Investigation of roll bonding between aluminum alloy strips", Materials & Design, vol. 29, iss. 4, 2008, p909-913.

Elzinga E., "Improvement of Welding Three-Piece Cans", Hoogovens internal R&D Report (1996-1997), p61-65.

Elzinga E., "High Speed Welding Project – An Overview of Phase 3", Corus internal R&D Report, Rererence Source No. 107997, 2002.

Elzinga E., Internal Communication, Corus IJmuiden, July 2005.

Elzinga E., Internal Communication, Corus IJmuiden, July 2007.

Ferrasse S. and Piccavet E., "Thermal Modelling of the Mash Seam Welding Process Using FEM Analysis", Mathematical Modelling of Weld Phenomena 4, ed. Cerjac H., IOM Publications, Cambridge, 1998, p494-513.

Feulvarch E., Robin V., Bergheau J.M., "Resistance Spot Welding Simulation: a General Finite Element Formulation of Electrothemal Contact Conditions", Journal of Materials Processing Technology, vols. 153-154, 2004, p436-441.

Funk E.J., Begeman M.L., "Electrical and Metallurgical Characterisics of Mash Seam Welds", Welding Research Supplement, June 1956, p265s-274s.

Ganowski F.J., Williams N.T., "Advances in Resistance Spot and Seam Welding of Zinc Coated Steel Strip", Sheet Metal Industries, November 1972, p692-705.

Goldsmith A., Waterman T.E., Hirschorn H.J., "Handbook of Thermo Physical Properties of Solid Materials", vol. I, The MacMillan Company, New York, 1961.

Gould J.E., "Theoretical Analysis of Welding Characteristics during Resistance Mash Seam Welding of Sheet Steels", Welding Journal Research Supplement, October 2003, p263s-267s.

Greenwood J.A., Williamson J.B.P., "Contact of Nominally Flat Surfaces", Proceedings of the Royal Society of London. Series A, Mathematical and Physical Sciences, vol. 295, iss. 1442, April 1966, p300-319.

Greenwood J.A., "Constriction Resistance and The Real Area of Contact", British Journal of Applied Physics, vol. 17, 1966, p1621-1632.

Gregory L., Szczur J., Squires I., "The Australian Steelmakers Experience with the Welding of Tinplate Cans", The Art and Science of Welding, Auckland, New Zealand, Paper No. 10, 1985, p75-82.

Gutierrez-Miravete E. and Giamei A.F., "Recent Developments in Welding Modeling", Modelling of Casting, Welding and Advanced Solidification Processes VII, Eds. Cross M. and Capbell J., The Materials, Metals & Materials Society, 1995, p825-831.

Haigh S.J., "Preliminary Results of Electrical Characterisation of Body Plate for Welding", Metal Box Technical Record, Document No. TR10061092, 19/02/82.

Hill R, The mathematical Theory of Plasticity, Oxford University Press, London, 1950.

Hiroki I., Hideshi M., Mitsuru O., Kazuo M., "Steel Sheets for Can-Making", JFE Technical Report No. 2, March 2004, p32-40.

Holm R, Electric Contacts, 4th edition, Springer-Verlag, Berlin/Heidelburg/New York, 1967.

Hou Z., Kim I., Wang Y., Li C., Chen C., "Finite Element Analysis for The Mechanical Features of Resistance Spot Welding Process", Journal of Materials Processing Technology, vol. 185, 2007, p160-165.

Ichikawa M., Saito T., "The Effect of Contact Resistance on the Weldability of Can Materials", Fourth International Tinplate Conference – London, Paper No. 40, 1988.

Jaques S., "Tinplate and the Welded Can", Technical Paper, Australian Iron and Steel Propriety Ltd, Port Kembla, New South Wales, 1968, p17-26.

Krallics G., "Determination of Thermo-Mechanical Properties of Aluminium Base PM Material for Computer Simulation of Manufacturing Process", Euromat 99 – Vol 3, Microstructures, Mechanical Properties and Processes, Wiley VCH, Wienheim, 2000, p178-183.

Kloosterman G., "Contact Methods in Finite Element Simulations", PhD Thesis, University of Twente, Netherlands, ISNB 90-77172-04-1, 2002.

Lavery R.C., "Welding of Tinplate by The Soudronic Seam Welding Process at a Frequency of 100 c/s", British Steel Research Communication, Report 134D, February 1970.

Li C. and Thomas B.G., "Thermomechanical Finite Element Model of Shell Behaviour in Continuous Casting of Steel", Metallurgical and Materials Transactions B, vol. 35B, 2004, p1151-1172.

Li W., Li Q., Steven G.P., Xie Y.M., "An Evolutionary Shape Optimisation for Elastic Contact Problems Subject to Multiple Load Cases", Computer Methods in Applied Mechanics and Engineering, vol. 194, iss. 30-33, 2005, p3394-3415.

Linnert G.E., "Welding Metallurgy – Carbon and Alloy Steels 4th Edition", vol. 1, AWS, Florida, 1994.

Manesh D.H., Taheri A.K., "An Investigation of Deformation Behaviour and Roll Bonding Strength of Bimetal Strip during Rolling", Mechanics of Materials, vol. 37, 2005, p531-542.

Mitchell J.W., Soltis M., "Semi-Mash Seam Welding", Welding Journal, August 1973, p509-516.

Mohamed H.A., Washburn J., "Mechanism of Solid State Pressure Welding", Welding Research Supplement, September 1975, p302s-310s.

Mughal M.P., Fawad H., Mufti R., "Finite Element Prediction of Thermal Stresses and Developments in Layered Manufacturing of Metallic Parts", Acta Mechanica, vol. 183, 2006, p61-79.

Murakawa H., Minami H., Kato T., "Finite Element Simulation of Seam Welding Process", Transactions of the Japanese Welding Research Institute, vol. 30, iss. 1, 2001, p111-117.

Nakakoji H., Akeda Y., Nakamaru H., Ichida T., "Effect of Surface Morphology and Another Metal Plating on Weldability of Electrolytic Chromium Coated Steel for Welded Can", Transactions of the Iron and Steel Institute of Japan, vol. 27, 1987, pB137-B138.

Needham J.C., "Measurement of True Resistance at High Alternating Current (For Resistance Spot and Seam Welding, and for Cables)", The Welding Institute Technology Briefing No. 210, April 1983.

Okamoto H., "Desk Handbook: Phase Diagrams for Binary Alloys", ASM International, Cleveland OH, 2000.

Oldroyd P.S., Williams N.T., "Overcoming the Inherent Problems of Coated Steels", Welding and Metal Fabrication, March 1980, p97-103.

Pavlik V., Dilthey U., "A Numerical and Experimental Investigation of Heat and Fluid Flow in Electric Arc Weld Pools", Modelling of Casting, Welding and Advanced Solidification Processes IX, Eds. Cross M. and Capbell J., The Materials, Metals & Materials Society, 1995, p825-831.

Price J.W.H., Ziara-Paradowska A., Joshi S., Finlayson T., Semetay C. and Nied H., "Comparison of Experimental and Theoretical Residual Stresses in Welds: The Issue of Gauge Volume", International Journal of Mechanical Sciences, 50, 2008, p513-521.

Renard J.F., Gellez J., "Tinplate Specification for New Applications", Fifth International Tinplate Conference – London, Paper No. 11, 1992.

Phillips A.L (ed), Welding Handbook, 4th edition, American Welding Society, New York 1960.

Raabe D., "Computational Materials Science", Wiley-VCH, Weinheim, 1998.

Richard D., Fafard M., Lacroix R., Cléry P., Maltais Y., "Carbon to Cast Iron Contact Resistance Constitutive Model for Finite Element Analysis", Journal of Materials Processing Technology, vol. 132, 2003, p119-131.

Richard D., Fafard M., Lacroix R., Cléry P., Maltais Y., "Aluminium Reduction Cell Anode Stub Design Using Weakly Coupled Thermo-Electro-Mechanical

Finite Element Models", Finite Elements in Analysis and Design, vol. 37, 2001, p287-304.

Roll A., and Motz h., "Der Electrische Widerstand von Metallischen Schmelzen", Zeitschrift fur Metallkunde, vol. 48, 1957, p272-280.

Rusinek A., Zaera R., Klepaczko J.R., "Constitutive Relations in 3-D for a Wide Range of Strain Rates and Temperatures – Application to Mild Steels", International Journal of Solids and Structures, vol. 44, 2007, p5611-5634.

Savage W.F., Nippes E.F., Wassel F.A., "Static Contact Resistance of Series Spot Welds", Welding Research Supplement, November 1977, p365s-370s.

Savage W.F., Nippes E.F., Wassel F.A., "Dynamic Contact Resistance of Series Spot Welds", Welding Research Supplement, February 1978, p43s-50s.

Scala E. and Robertson W.D., "Electrical Resistivity of Liquid Metals and of Dilute Liquid Metallic Solutions", Journal of Metals, vol. 5, 1953, p272-280.

Schaerer G., Weil W., "Soudronic Welding Technique – A Promoter of Tinplate Containers", Third International Tinplate Conference – London, Paper 21, 1984.

Schuler A.W., "Resistance Seam Welding", WRC Bulletin 225, Welding Research Council, April 1977.

Shewchuk J.T., "An Introduction to the Conjugate Gradient Method Without the Agonizing Pain", Technical Report: CS-94-125, Carnegie Mellon University Pittsburgh, PA, USA, 1994.

Shimizu N., Hayashida T., Nishimoto N., Fukai J., Miyatake O., "Relation Between Equivalent Contact Resistance and Resistance Seam Weldability for Beverage Cans", Testu-to-Hagane, 1998, vol. 84, IV, p249-254.

Simon F.E., Toner D.F., "The Influence of Tinplate Surface Characteristics on Wire Welding", Fifth International Tinplate Conference – London, Paper No. 16, 1992.

Singer M & Kshonze K, "Electrical Resistance of Random Rough Contacting Surfaces Using Fractal Surface Modeling", Proceedings of the IEEE 37th Holm Conference, p73, 1991, p73-82.

Slade P.G (ed), Electrical Contacts – Principles and Applications, Marcel Dekker Ltd, New York, 1999.

Smith I.M. & Griffiths D.V., "Programming the Finite Element Method", 4th Edition, John Wiley & Sons, England, 2004.

Smith I., Leng J., Margetts L., "Parallel Three-Dimensional Finite Element Analysis of Excavation", 13th ACME Conference: University of Sheffield, March 21-22, 2005.

Snee R.K., Taylor J.L., "Infra-Red Monitoring of Resistance Spot Welding", Metal Construction and British Welding Journal, April 1972, p142-148.

Sodeik M., Taffner K, Webber F., "Fundamentals of Modern Can Making and Materials Development for Three Piece Can Manufacturing", Transactions of The Iron and Steel Institute of Japan, vol. 28, 1988, p663-671.

Song Q., Zhang W., Bay n., "An Experimental Study Determines the Electrical Contact Resistance in Resistance Welding ", Welding Research Supplement, May 2005, p73s-76s.

Stenström B., "Electrical Resistivity of FeSn Single Crystals", Physica Scripta, vol. 6, 1972, p214-216.

Sun X, "Effect of Projection Height on Projection Collapse and Nugget Formation – A Finite Element Study", Welding Research Supplement, September 2001, p211s-216s.

Sunar M., Yilbas B.S., Boran K., "Thermal and Stress Analysis of a Sheet in Welding", Journal of Materials Processing Technology, vol. 172, 2006, p123-129.

Suthar B.S., "Numerical Modelling of the High Speed Resistance Seam Welding Process", University Thesis, University of Wales Swansea, 2005.

Tafzi K., Cabrera J.M., Prado J.M., "Hot Flow Description of ARMCO Iron", Euromat 99 – Vol 3, Microstructures, Mechanical Properties and Processes, Wiley VCH, Wienheim, 2000, p262-268.

Takeuchi S. and Endo H., "Studies on the Electrical Resistivity of Pure Metals in the Molten State", Journal of the Japan Institute of Metals, vol. 26, 1962, p498-503.

Taylor G.A., Hughes M., Pericleous K., "The Application of Three Dimensional Finite Volume Methods to the Modelling of Welding Phenomena", Modelling of Casting, Welding and Advanced Solidification Processes IX, Eds. Sahm P.R., Hansen P.N., Conley J.G., The Materials, Metals & Materials Society, 2000, p852-859.

Thieblemont E, Gobez P, Bollinger E & Chevrrier J Ch, "Resistance Spot Welding: Measurement of Dynamic Electrical Resistance of the Electrode Sheet Interface", Modelling of Casting Welding and Advanced Solidification Processes 5, Eds. Rappaz M *et al*, The Minerals, Metals & Materials Society, USA, 1995.

Tsirkas S.A., Papanikos P., Kermanidis Th., "Numerical Simulation of The Laser Seam Welding Process in Butt-Joint Specimens", Journal of Materials Processing Technology, vol. 134, 2003, p59-69.

Tylecote R.F., Howd D., Furmidge J.E., "The Influence of Surface Films on the Pressure Welding of Metals", British Welding Journal, January 1958, p21-38.

Waddell W., Thomas D.E., Williams N.T., "High Speed Seam Welding of Low Tin Substrates", Metal Construction, March 1986, p156-161.
Wen S., "Preliminary Investigation on Modelling of Can Body Seam Welding", Corus Internal Document, October 2001.

Wen S., "Preliminary Investigation on Modelling of Can Body Seam Welding", Corus Internal Document, Transport Applications, Corus RD&T, Rotherham, 2001.

Wen S.W., Hilton P., Farrugia D.C.J., "Finite Element Modelling of a Submerged Arc Welding Process", Journal of Materials Processing Technology, vol. 119, 2001, p203-209.

Westgate S.A., "Recent Developments in Resistance Seam Welding", The Welding Institute Research Bulletin, December 1980, p376-380.

Westgate S.A., "The High Speed Seam Welding of Nominally 1.2mm Low Carbon Steel Sheets", The Welding Institute Technology Briefing No. 240, June 1984.

Williams N.T., Thomas D.E., Wood K., "High Speed Welding of 211 Aerosol Bodies using The 150 Hz Soudronic Process", British Steel Research Communication, Report 809D, June 1975.

Williams N.T., Thomas D.E., Wood K., "High Speed Seam Welding: Part 1 – Equipment Development, Weldability Lobes and Metallurgical Characteristics", Metal Construction, April 1977, p157-160.

Williams N.T., Thomas D.E., Wood K., "High Speed Seam Welding: Part 2 – influence of Welding Parameters and Material, And Production Implications", Metal Construction, April 1977, p202-208.

Wilson C.D., "A Critical Reexamination of Classical Metal Plasticity", Journal of Applied Mechanics, vol. 69, 2002, p63-68.

Wright P.K., Snow D.A., Tay C.K., "Interfacial Conditions and Bond Strength in Cold Pressure Welding by Rolling", Metals Technology, January 1978, p24-31.

Yovanovitch M.M. & Sridhar M.R., "Elasto-plastic Contact Conductance Model for Isotropic Conforming Rough Surfaces and Comparison with Experiments", Journal of Heat Transfer, vol. 118, Feb 1996, p3-9.

Zienkiewicz O.C., Valliappan S., King I.P., "Elasto-Plastic Solutions of Engineering Problems, 'Initial Stress', Finite Element Approach", International Journal for Numerical Methods in Engineering, vol. 1, 1969, p75-100.

Zienkiewicz O.C., Irons B.M., Ergatoudis J., Ahmad S., Scott F.C., "Iso-Parametric and Associated Element Families for Two- and Three-Dimensional Analysis", In Proceedings of a Course on Finite Element Stress Analysis, eds. Holland I. and Bell K., Norwegian University of Science and Technology, Trondheim, Norway, 1969.

Zienkiewicz O.C., Cormeau I.C., "Visco-Plasticity – Plasticity and Creep in Elastic Solids – A Unified Numerical Solution Approach", International Journal for Numerical Methods in Engineering, vol. 8, 1974, p821-845.

9.0 BIBLIOGRAPHY

Callister W.D., "Fundamentals of Materials Science and Engineering", Wiley & Sons, New York, 2001.

Desai C.S., "Introduction to the Finite Element Method", Van Nostrand Reinhold, New York, 1972.

Linnert G.E, "Welding Metallurgy – Carbon and Alloy Steels 4th Edition", vol. 1, AWS, Florida, 1994.

Porter & Easterling, "Phase Transformations in Metals and Alloys", Chapman & Hall, London, 1992.

Raabe D., "Computational Materials Science", Wiley-VCH, Weinheim, 1998.

Smith I.M. & Griffiths D.V., "Programming the Finite Element Method", 4th Edition, John Wiley & Sons, England, 2004.